2014

Theoretical and Numerican Studies of Phase Transitions and Error Thresholds in Topological Quantum Memories

Pejman Jouzdani
University of Central Florida

THEORETICAL AND NUMERICAL STUDIES OF PHASE TRANSITIONS AND ERROR THRESHOLDS IN TOPOLOGICAL QUANTUM MEMORIES

by

PEJMAN JOUZDANI
B.Sc. in Physics, Isfahan University of Technology, 2006
M.Sc. in Photonics, Shahid Beheshti University, 2009
M.Sc. in Physics, University of Central Florida, 2014

A dissertation submitted in partial fulfilment of the requirements
for the degree of Doctor of Philosophy
in the Department of Physics
in the College of Science
at the University of Central Florida
Orlando, Florida

Fall Term
2014

Major Professor: Eduardo Mucciolo

ABSTRACT

This dissertation is the collection of a progressive research on the topic of topological quantum computation and information with the focus on the error threshold of the well-known models such as the unpaired Majorana, the toric code, and the planar code.

We study the basics of quantum computation and quantum information, and in particular quantum error correction. Quantum error correction provides a tool for enhancing the quantum computation fidelity in the noisy environment of a real world. We begin with a brief introduction to stabilizer codes. The stabilizer formalism of the theory of quantum error correction gives a well-defined description of quantum codes that is used throughout this dissertation. Then, we turn our attention to a quite new subject, namely, topological quantum codes. Topological quantum codes take advantage of the topological characteristics of a physical many-body system. The physical many-body systems studied in the context of topological quantum codes are of two essential natures: they either have intrinsic interaction that self-corrects errors, or are actively corrected to be maintained in a desired quantum state. Examples of the former are the toric code and the unpaired Majorana, while an example for the latter is the surface code.

A brief introduction and history of topological phenomena in condensed matter is provided. The unpaired Majorana and the Kitaev toy model are briefly explained. Later we introduce a spin model that maps onto the Kitaev toy model through a sequence of transformations. We show how this model is robust and tolerates local perturbations. The research on this topic, at the time of writing this dissertation, is still incomplete and only preliminary results are represented.

As another example of passive error correcting codes with intrinsic Hamiltonian, the toric code is introduced. We also analyze the dynamics of the errors in the toric code known as anyons. We show numerically how the addition of disorder to the physical system underlying the toric code

slows down the dynamics of the anyons. We go further and numerically analyze the presence of time-dependent noise and the consequent delocalization of localized errors.

The main portion of this dissertation is dedicated to the surface code. We study the surface code coupled to a non-interacting bosonic bath. We show how the interaction between the code and the bosonic bath can effectively induce correlated errors. These correlated errors may be corrected up to some extend. The extension beyond which quantum error correction seems impossible is the error threshold of the code. This threshold is analyzed by mapping the effective correlated error model onto a statistical model. We then study the phase transition in the statistical model. The analysis is in two parts. First, we carry out derivation of the effective correlated model, its mapping onto a statistical model, and perform an exact numerical analysis. Second, we employ a Monte Carlo method to extend the numerical analysis to large system size.

We also tackle the problem of surface code with correlated and single-qubit errors by an exact mapping onto a two-dimensional Ising model with boundary fields. We show how the phase transition point in one model, the Ising model, coincides with the intrinsic error threshold of the other model, the surface code.

This dissertation is dedicated to my parents Parvin and Reza.

ACKNOWLEDGMENTS

"That which does not kill us makes us stronger."

— Friedrich Nietzsche

Our lives are a collection of short memories of a grand picture, of an existence, painted in the color of symmetries and by laws of physics. In the challenge to discover it and in the hope of remembering its truth we thought, we pondered, and found ourselves existing in the memory of future existents.

I must declare sincere appreciation, first and before anyone else, for the one person that I will remember and will be remembered for the most part of my memories in the rest of my life: my kind intelligent adviser, Eduardo Mucciolo, who turned the black and white world of doubts and mystery into a fruitful journey of understandings and showed the right path of success. This short acknowledgment never is enough to fully state his contributions to who I am and to what I achieved during the PhD program under his supervision.

I would like to thank him for all his advices on academic and non-academic matters. I would like to thank him for his leadership, for his support, for his work ethics, for showing the right discipline of independence in work while staying fully collaborative, for showing how to be a rigorous researcher and yet reveal a calm kind self, for his unique intuitive approach to physics that he taught us, and all his teachings that will be my guide for the rest of my life.

Next, I would like to thank my parents, without whom I could never find myself where I am. Especially, I would like to thank my mom for all her devotions and her sacrifices, and her smile that never faded even at the hardest moments in life and only for one reason: carry on son.

I would like to thank my sister Parvaneh Javadi for her help and support during these years, my brothers Payman and Parviz, my brother-in-law Peiman Javadi, and my lovely nephews and niece: Anahita, Ario, Beijan, and Khashayar.

I would like to specially thank Michael Leueneberger for his amazing lectures. Indeed most of what I've learned was in his classes and in his in-depth and elaborate lectures. Especially, I thank Eduardo Novais and our productive collaborations. I thank Igor Tupitsyn and Robert Raussendorf for valuable discussion during my stay at UBC, summer 2013.

I would like to thank my amazing friends who inspired me and were supportive in the past years. I specially thank my best friends Navid Kargahi, Christopher Lörcher, Sebastian Zuluaga, George Luchita, Ahmad Khastedel, and Shiva Davari. I would like to thank my colleagues Amin Ahmadi, Javier Romero, Leandro Lima, Guilherme Martins, and Sabine Pelton, and the faculty and classmates that together created a friendly environment all these years.

This work was supported in part by the Office of Naval Research (ONR) and the National Science Foundation (USA).

Finally, I would like to thank and acknowledge my former lecturers and advisers: Mansour Haghighat, Behrouz Mirza, and Mehdi Safa Esfahani.

TABLE OF CONTENTS

LIST OF FIGURES

CHAPTER 1: INTRODUCTION

"He who thinks great thoughts often makes great errors."

— Martin Heidegger

1.1 Quantum error correction

In the first section we formally introduce the evolution of an open quantum system by describing the quantum states in terms of the density matrix formalism.

1.1.1 Quantum Operations

Consider a closed system consisting of the environment and a *central quantum system*, with an associated Hilbert space of $\mathcal{H}_S \otimes \mathcal{H}_{Env}$. Assume that the initial state of the system is $|\psi\rangle$. At time t the state of the closed system has evolved to the new state $|\psi(t)\rangle = U(t)|\psi\rangle$, where $U(t)$ is a unitary time-evolution operator. An equivalent way to express this time evolution is using the density matrix representation. Then, the system is initial density matrix is $\rho = |\psi\rangle\langle\psi|$ and at time t it is given by $\rho(t) = U(t)|\psi\rangle\langle\psi|U^\dagger(t)$. A particular case is when the initial state of the closed system is a *product state*,

$$\rho(t) = U(t)(|\mathrm{Env}\rangle\langle\mathrm{Env}| \otimes \rho_s)U^\dagger(t), \tag{1.1}$$

where we used $|\mathrm{Env}\rangle\langle\mathrm{Env}|$ to represent the initial density matrix of the environment, while ρ_s represents the initial density matrix of the system.

The Hilbert space of the environment can be spanned by a complete set of orthogonal states $\{|e_k\rangle\}$. This set may be discrete, continuous, or both. In general, we can trace the degrees of freedom of the environment in the following way:

$$\begin{aligned}\rho^s_{\rm red}(t) &= \sum_k \langle e_k|\, U(t)(|{\rm Env}\rangle\langle{\rm Env}|\otimes\rho_s)U^\dagger(t)\,|e_k\rangle \\ &= \sum_k \langle e_k|U(t)|{\rm Env}\rangle\ \rho_s\ \langle{\rm Env}|U^\dagger(t)|e_k\rangle \\ &= \sum_k E_k\,\rho_s\,E_k^\dagger = \mathcal{E}(\rho_s). \end{aligned} \tag{1.2}$$

We then obtain the **reduced density matrix** representation of the system as a function of time. On the last line we defined operators $E_k = \langle e_k|U(t)|{\rm Env}\rangle$. It is straightforward, by dimensionality analysis, to see that E_k has a matrix representation with the same dimension as ρ_s. For example, a single qubit system for which ρ_s is a 2×2 matrix, E_k is also a 2×2 matrix for all k. Since any 2×2 matrix can be expanded by Pauli matrices, we have

$$E_k = \alpha_0\sigma^0 + \alpha_1\sigma^1 + \alpha_2\sigma^2 + \alpha_3\sigma^3, \tag{1.3}$$

with $\sigma^0 = I$ and σ^i being one of the three Pauli matrices $\{\sigma^x,\sigma^y,\sigma^z\}$. The coefficients α_ν are obtained as $\alpha_\nu = \frac{1}{2}{\rm Tr}(\sigma^\nu E_k)$. This follows from the property of the Pauli matrices that they have zero trace, ${\rm Tr}(\sigma^\nu) = 0$, and $\frac{1}{2}{\rm Tr}(\sigma^0) = 1$. In general, for a system that comprises of N qubits, E_k acts on a Hilbert space $\mathcal{H}_s = \mathcal{H}_1^2\otimes\cdots\otimes\mathcal{H}_N^2$. Then, the extension of the above expansion is

$$E_k = \sum_{\mu_1,\ldots,\mu_N} \alpha_{\mu_1,\ldots,\mu_N}\sigma_1^{\mu_1}\ldots\sigma_N^{\mu_N}, \tag{1.4}$$

with coefficients $\alpha_{\mu_1,\ldots,\mu_N} = \frac{1}{2^N}{\rm Tr}(\sigma_1^{\mu_1}\ldots\sigma_N^{\mu_N}E_k)$.

Equation (1.2) represents the time evolution of the reduced density matrix and is called *operator-*

sum representation, it is widely used in literature of quantum error correction [50, 1]. This representation will be used in the formal theory of quantum error correction presented in the following sections.

1.1.2 Theory

After giving a short review on some of the necessary tools, we can now introduce quantum error correction. The purpose of quantum error correction is to immunize the state of the central system as much as possible against errors that may damage the system during the time period in which quantum computational processes are being performed.

The general outline of the theory of quantum error correction, inherited from *classical error correction theory*, is the art of: First, initializing the system in the appropriate subspace of the accessible Hilbert space of the quantum system $\mathcal{H}_s$, known as the **quantum error-correcting code** (also code-space or code-word). Next, to detect the new state of the system once the encoded system is subjected to an error E_k relative to the code subspace by a series of **syndrome measurements**. Finally, to perform a **recovery** operation based on the detected error syndrome on the system that most likely returns the quantum system to the initial code state. A "success measure" of a given quantum code is assessed by studying the **error threshold** of the quantum code.

Theorem 1.1.1 (Quantum error correcting conditions) *Let C be a quantum code, and let P be the projector onto C. Suppose $\mathcal{E}$ is a quantum operation with operation elements $\{E_i\}$. A necessary and sufficient condition for the existence of an error-correction operation $\mathcal{R}$ correcting $\mathcal{E}$ on C is that*

$$PE_i^\dagger E_j P = \alpha_{ij} P, \tag{1.5}$$

for some Hermitian matrix α of complex numbers.

A formal proof can be found in Ref. [50]. A more intuitive justification of the proof is the following.

Let us first show the sufficiency. Since α_{ij} is a Hermitian matrix, it can be diagonalized as $\alpha = udu^\dagger$. Let us construct a new set of errors $\{F_k\}$ using matrices u and $u^\dagger$ such that $F_k = \sum_i u_{ik} E_i$ is a linear superposition of the set $\{E_k\}$. Then the condition Eq. (1.5) is changed to $PF_k^\dagger F_l P = d_{lk}\delta_{lk} P$. By using polar decomposition we can show that $F_k P = \sqrt{d_{kk}} U_k P$ for some unitary U_k. Also let us define $P_k = U_k^\dagger P U_k^\dagger = \frac{F_k P U_k^\dagger}{\sqrt{d_{kk}}}$.

The system is initially encoded in the subspace P as $\rho_{cs} \equiv P\rho_{cs}P$. Then, by looking at Eq. (1.2) with the set of errors $\{F_k\}$, the faulty density matrix of the system after an evolution time t is $\mathcal{E}(\rho_s) = \sum_l F_l P \rho_s P F_l^\dagger$. Now, by applying the combination $U_k P_k$ that acts as a detection (P_k) followed by a recovery process U_k, we have

$$\rho_s \to \sum_l F_l P \rho_s P F_l^\dagger \to \sum_{kl} U_k^\dagger P_k F_l P \rho_s P F_l^\dagger P_k U_k,$$

but the latter is

$$\begin{aligned} \mathcal{R}(\mathcal{E}(\rho_s)) &= \sum_{kl} U_k^\dagger P_k F_l P \rho_s P F_l^\dagger P_k U_k. \\ &= \sum_{kl} \frac{U_k^\dagger U_k P F_k^\dagger F_l P \rho_s P F_l^\dagger F_k P U_k^\dagger U_k}{d_{kk}}. \\ &= \sum_{kl} d_{kk} \rho_s \propto \rho_s. \end{aligned} \tag{1.6}$$

In the last line we used the condition (1.5). Therefore, it is sufficient to have the condition of Eq. (1.5) to build a set of orthogonal projective subspaces $\{P_k\}$ and their corresponding recovery

operations $\{U_k\}$.

The necessity is straightforward. If for each error in the set a recovery operation R_j exists, then

$$\sum_{ij} R_j E_i P \rho_s P F_i^\dagger R_j^\dagger = c P \rho_s P. \tag{1.7}$$

One can define $R_k E_i P = c_{ki} P$ and its adjoint to derive $\alpha \equiv \sum_k c_{ki}^\star c_{kj}$, which is a Hermitian matrix, as expected.

The next essential theorem for quantum error correction, which we quote without proof from Ref. [50], states:

Theorem 1.1.2 *Suppose C is a quantum code and $\mathcal{R}$ is the error-correction operation constructed in the proof of Theorem 1.1.1 to recover from a noise process $\mathcal{E}$ with operation elements $\{E_i\}$. Suppose $\mathcal{F}$ is a quantum operation with operation elements $\{F_j\}$ which are linear combinations of the E_i, that is $F_j = \sum_i m_{ji} E_i$ for some matrix m_{ji} of complex numbers. Then the error-correction operation $\mathcal{R}$ also corrects the effects of the noise process $\mathcal{F}$ on the code C.*

The theorem simply states that as long as we have a code that can be corrected against a discrete set of errors, the same code can be corrected against any linear combination of that set. This is a tool to deal with the continious nature of quantum noise. As an abstract example, if a single qubit can be corrected against the set of all Pauli matrices, then it can be corrected against an entire set of errors, as in Eq. (1.3).

To summarize, the theory of quantum error correction is built upon the above two theorems. The first provides us with a checking tool. The checking tool is used to test the validity of a given quantum code as well as the domain of errors it will correct. The second theorem deals with the continious nature of the Hilbert space. In contrast to classical errors where the state of the

information is discrete, in the quantum version the state can continuously sweep a Hilbert space. The second theorem guarantees that by being able to correct a discrete set of operations we can correct a continuous spectra of errors.

1.1.3 Classical linear code

So far we addressed the formalism of quantum operations and the theorems that quantum error correcting codes are based on. Now, we show actual error-correcting codes that satisfy the theorems above. To have a good understanding of how quantum error-correcting codes can be defined, we begin by considering the basics of linear classical codes and their construction. In the next section we present quantum error-correcting codes.

Consider an array of k bits represented in the form of a vector in a k-dimensional space. Such vector is defined on a $\mathbf{Z_2}$ field since a bit takes either 0 or 1. For example two bits have altogether $\{(0,0),(0,1),(1,0),(1,1)\}$ *code-words*. Assume a system of two bits that are initialized in the code-word $(0,0)$. Furthermore, assume that bit-flip noise flips the first bit. The corrupted state would be $(1,0)$. The question to be answered by a linear correcting-code is "given a vector $(1,0)$, how can we identify the initial state? Is it $(1,0)$ with no error, $(0,0)$, or $(1,1)$ with a bit flip error, or is the initial state $(0,1)$ with two bit-flip errors?

To be able to answer these and similar questions, where one needs to resolve some given vectors of data from each other, classical linear code is used [2]. We start by building a linear operator, a matrix G known as the *generating matrix* of the code, that takes a k component vector and returns an n-component vector with $n > k$. G encodes each code-word x of the k-dimensional space as Gx, the *code*. G has independent columns and thus the mapped space Gx for all x is a subspace in the larger n-dimensional vector space.

Example:

$$G^T = \begin{bmatrix} 1 & 1 & 1 & 0 & 0 & 0 \\ 0 & 0 & 0 & 1 & 1 & 1 \end{bmatrix}$$

with Gx given by

$$G(0,0) = (0,0,0,0,0,0),\ G(1,0) = (1,1,1,0,0,0)$$
$$G(0,1) = (0,0,0,1,1,1),\ G(1,1) = (1,1,1,1,1,1). \tag{1.8}$$

We might think that there are 2^k elements or code-words of data, and that $n2^k$ operations to be performed to specify the full encoding. However, to define a "linear" code all we needed is to define an $n \times k$ generating matrix. The full encoding is encapsulated in G.

Error correction can be performed by defining the *parity check matrix* $H_{n-k,n}$. The matrix is basically the collection of $n-k$ ($n-$component) independent vectors that are orthogonal to all the columns of G. Roughly speaking, H defines a subspace orthogonal to the subspace Gx or the code. Therefore, to check if a vector x belongs to the code it has to satisfy $Hx = 0$. Therefore, mathematically, H is a linear map and the code is defined as the *kernel* of the map H.

Knowing that the code is the kernel of H, now assume that a code-word $y = Gx$ is corrupted by bit flip errors and changed to $y' = y + e'$. Notice that the vector e' is a vector with 1's at the affected bits and 0 elsewhere. Since $Hy = 0$ we have $Hy' = He$. Naturally, the set $\{He\}$ are the *syndromes* detected in this way. What we are interested is to be able to distinguish vectors like He_1 from vectors He_2 for as many errors (e_1 and e_2) as possible. If that were possible then each *error syndrome* He would tell us what the initial code-word was. The strength of this method relies on how many 1's a code-word y_1 differs from a code-word y_2. Any vector y' that lies in between them (by adding 1's to, say, y_1: $y' = y_1 + e'$) is detected by He' and corrected to the closest code-word

(say y_1). Thus, to be able to correct more errors we need to have a code that provides a large *(Hamming) distance* between the code-words. The minimum distance between code-words of a given code is called the **distance of the code** d.

The initial vectors of bits to be encoded by G, contain the actual information to be coded and are called the **logical bits**. Also we can see $G_{n\times k}$ as a vector of length k with linearly independent vectors v of length n as its elements; $G = [v_1, \ldots, v_k]$. In this light, $y = Gx$ is a sum over a subset of these independent vectors: $y = \sum_{\{j\}} v_j$. Since the logical bits x consist of all possible combinations of 0 and 1, then the set $\{\sum_{\{j\}} v_j\}$ is the set of all combinations of the independent columns of matrix G, all the possible sets $\{j\}$. Now, if we add two code-words $y + y' = \sum_{\{j\}} v_j + \sum_{\{j'\}} v_{j'} = \sum_{\{j''\}} v_{j''} = y''$, we have $y'' \in C$. Likewise, one can see there is a unit element $E = G(0, \ldots, 0) \in C$. Also, for each element $y + y = E$, thus, the inverse element is in C. Therefore, code-words in C form a group.

In summary, a code C defined by a generating matrix G (or, equivalently, H) is formally denoted by $[n, k, d]$, which means that k bits are encoded into n bits and the minimum distance between the code-words is d.

1.1.4 Calderbank-Shor-Steane codes

We know that a classical linear code corrects, say, t number of bit-flip errors (equivalent to a distance $2t + 1 = d$). In contrast to a simple bit-flip error of classical physics, however, we know that errors in quantum mechanics are continuous. Also, from the theories of quantum error correcting codes if we are able to correct bit-flip and phase-flip errors, we are able to correct the qubits from any error (that is, an error that is a linear superposition of Pauli matrices $\sigma^x, \sigma^y, \sigma^z$).

One natural way to construct a quantum code seems roughly to have two classical codes working

together. We could use one to correct bit-flip errors and other code [with a Hadamard rotation] for phase-flip errors. This is the basic idea behind Calderbank-Shor-Steane (CSS) codes. More explicitly, consider classical codes C_1 and C_2. A code-word $x \in C_1$ will be encoded as

$$|x + C_2\rangle \equiv \frac{1}{\sqrt{|C_2|}} \sum_{y \in C_2} |x + y\rangle. \tag{1.9}$$

This defines an equivalent class between the elements of C_1 with respect to C_2, which is the set of cosets of C_2 in C_1 (C_1/C_2). Thus each codeword of the CSS(C_1, C_2) is a superposition of the elements in one equivalent class, i.e., it forms one coset. If the two elements x and x' belong to two different cosets, the two code-words $|x + C_2\rangle$ and $|x' + C_2\rangle$ are orthogonal. For a C_1 $[n, k1]$ and a C_2 $[n, k_2]$ code, CSS(C_1, C_2) is a $[n, k_2 - k_1]$ code.

Consider a quantum system with a state initially prepared in a CSS(C_1, C_2) code-word. Once a phase-flip e_2 accompanied by a bit-flip e_1 corrupt the original code-word, the new state of the system will be

$$\frac{1}{\sqrt{|C_2|}} \sum_{y \in C_2} (-1)^{(x+y).e_2} |x + y + e_1\rangle. \tag{1.10}$$

Assuming an ancilla qubit was appended, we could apply the parity check matrix to have

$$\frac{1}{\sqrt{|C_2|}} \sum_{y \in C_2} (-1)^{(x+y).e_2} |x + y + e_1\rangle |H_1 e_1\rangle, \tag{1.11}$$

where H_1 is the parity check matrix of the code C_1. Notice we assume that the ancilla qubit itself is immune from errors. Under this condition, one has to measure the ancilla qubit to detect the bit-flip *syndrome*, and, as the next step, to apply an appropriate *recovery* operation.

Notice that by a Hadamard matrix one can switch the role of bit-flip σ^x with phase-flip σ^z. There

exists a simple scheme that uses the Hadamard gate that practically switches the role of e_1 and e_2 in the above procedure and uses the same syndrome detection applied for the bit-flip above to detect the phase-flip error e_2. For more details see Ref. [50].

1.1.5 Stabilizer codes

There exists an alternative approach to define quantum codes by using the language of group theory. To explain the technicalities of this approach along with advantages and disadvantages of it, we begin with some nomenclatures and definitions that will be used later.

Pauli Groups: A Pauli group G_n is constructed by the matrix multiplication of all the Pauli matrices acting on n qubits. Example: $G_1 = \{\pm I, \pm iI, \pm\sigma^x, \pm i\sigma^x, \pm\sigma^y, \pm i\sigma^y, \pm\sigma^z, \pm i\sigma^z\}$. It can be easily verified that such group is closed under the matrix multiplication. Similarly, $G_2 = \{\pm I(= \pm I_1 \otimes I_2 = \pm I_1 I_2), \pm iI, \pm\sigma_1^x I_2, \dots\}$, etc.

Generators of a group: In any subgroup S of G_n we can find a set of elements such that under multiplication this set produces the whole subgroup S. Example: $S = \{I, Z_1Z_2, Z_2Z_3, Z_1Z_3\}$ is a subgroup of G_3 (or any G_n with $n \geq 3$). The subgroup can be generated by choosing the set $\{Z_1Z_2, Z_2Z_3\}$ as the set of generators of the subgroup. Notice that the set is not unique. A subgroup is usually represented by its generators as $\langle g_1, \dots\rangle$, with g_i being the i-th generator; In the example above $S = \langle Z_1Z_2, Z_2Z_3\rangle$. We will always select a set of generators such that all its elements $g_1, \dots$ are independent.

Centralizer and Normalizer: Given a subgroup S, the set $C(S) = \{E \in G_n | Eg = gE\}$ is called the *centralizer* of the subgroup S. Given a subgroup S, the set $N(S) = \{E \in G_n | EgE^\dagger = g\}$ is called the normalizer of the subgroup S. For Pauli groups G_n, if S does not include $-I$ then we have $N(S) = C(S)$.

Stabilizer: Consider a vector space V_S and a subgroup S such that for any element $|\psi\rangle \in V_S$ and any element $M \in S$ we have $M|\psi\rangle = +|\psi\rangle$. Then, V_S is said to be **stabilized** by S, and S is called the *stabilizer* of the vector space V_S.

It is obvious that for any subgroup S that contains $-I$ the only possible vector space that can be stabilized by S is the trivial 0 state. It is straightforward to show that if we restrict ourselves to only subgroups in which $-I$ is excluded, then elements $\pm iI$ are automatically excluded as well. Also, notice that if a vector state is stabilized by the set of generators of S, it is stabilized by the whole subgroup S. Therefore, we only need to verify that $g_i|\psi\rangle = |\psi\rangle$ for all $g_i \in \langle g_1, \dots \rangle$ of subgroup S in order to claim that $|\psi\rangle$ is stabilized by S.

Working with n qubits automatically implies the use of the Pauli group G_n, since all possible quantum operations that can be applied on n qubits are contained in G_n. Consider a subgroup $S = \langle g_1, \dots, g_{n-k} \rangle$. We define the projector P_S^x as

$$P_S^x = \frac{\prod_{i=1}^{n-k}(I + (-1)^{x_i} g_i)}{2^{n-k}}, \tag{1.12}$$

where x stands for $(x_1, \dots, x_{n-k})$. It can be verified that by expanding the product in the definition we generate all the elements in S. Therefore, if for a state $|\psi\rangle$ we have $P_S^0|\psi\rangle = +|\psi\rangle$, then $|\psi\rangle \in V_S$. Also, it is easy to see that for any $|\psi\rangle \in V_S$, $P_S^0|\psi\rangle = +|\psi\rangle$. Hence, we conclude that P_S^0 is a projector onto V_S. Let us add that the projectors P_S^x are a set of orthogonal projectors; the product $P_S^x P_S^{x'}$ for different sets of $x = (x_1, \dots, x_{n-k})$ and $x' = (x'_1, \dots, x'_{n-k})$ has at least one term such as $(I - g_i)(I + g_i)$ which gives 0 on any state.

The Hilbert space of n qubits is 2^n dimensional and there are 2^{n-k} different combinations of sets x. Since $\sum_x P_S^x = I_{2^n \times 2^n}$, then the vector space V_S is a 2^k dimensional space.

With the main concepts being introduced, we can sketch an outline of the stabilizer code theory

as follows. Imagine the state of a system initially prepared such that it is stabilized by P_S^0 for a stabilizer subgroup S. Then, if an error $E_x \in G_n$ acts on the system there are two possibilities: Either E_x anti-commutes with at least one of the generators of $\langle g_1, \ldots, g_{n-k} \rangle$ or it commutes with all the elements of $\langle g_1, \ldots, g_{n-k} \rangle$. In the former case, the projector P_S^0 will be transformed according to $P_S^x = E_x P_S^0 E_x^\dagger$. In this case the code may be corrected by assigning an R_x recovery operation to the P_S^x projector for every orthogonal subspace x. Therefore, by measuring all P_S^x's and consequently applying corresponding R_x's we can recover the original state. In the latter case, the error E_x is either in S which means it makes no harm to the original state, or it is in $N(S) - S$. If $E_x \in N(S) - S$ then it is uncorrectable.

Finally, the **stabilizer code** $C(S)$ is defined as the vector space V_s which is stabilized by S. The code's distance is identified by the minimum weight of an element in $N(S) - S$. Here, the weight of an element E is defined by the number of Pauli operators in the element E that are not equal to I. For example, $E = X_1 Y_3 Z_8 \in G_8$ has weight 3. Also, as a reminder, a code $[n, k, d]$ corrects errors on t single qubit such that $d = 2t + 1$.

In summary, stabilizer codes are defined as subspaces that are stabilized by a set of generators of a subgroup of Pauli groups. An ideal stabilizer code would have a long distance while requiring minimum resources (i.e., a small Hilbert space).

1.2 Topological quantum computation

1.2.1 Introduction

The subject of topology covers a wide area of research and study in physics that goes far beyond this introduction. The following introduction is based on the physical aspects of the subject that will help us to better understand the specific models we study in the main body of this dissertation.

This introduction is mainly based on Refs. [4, 5] and, partly, [6].

To reach an intuitive but sufficiently deep understanding of the underlying concepts of topology in condensed matter problems, we begin by discussing the problem of a particle on a ring. Consider a particle on a ring (periodic boundary condition). Imagine the system to be in a magnetic field with a vector potential $A = \frac{\Phi}{\Phi_0}\hat{e}_\phi$. Then, the Hamiltonian of this system is

$$\hat{H} = \frac{1}{2}(-i\partial_\phi - A)^2, \tag{1.13}$$

where ϕ is the angle. It is straightforward to see that the function $\psi_n(\phi) = \frac{1}{\sqrt{2\pi}}e^{in\phi}$ satisfies the Schrödinger stationary equation, and the energy spectrum is $\epsilon_n = \frac{1}{2}(n - \frac{\Phi}{\Phi_0})^2$ with $n \in \mathbb{Z}$.

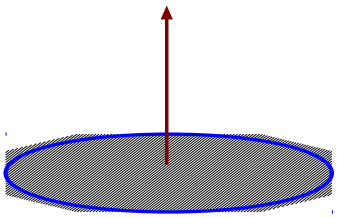

Figure 1.1: A confined particle on a ring subject to magnetic field.

This simple problem, though, in the language of functional integrals (the familiarity of the reader with the functional integral formalism of many-body physics is assumed) has interesting features to be unveiled. The partition function reads

$$Z = \int_{\phi(\beta)-\phi(0)\in 2\pi\mathbb{Z}} D\phi \; e^{\int d\tau L(\phi,\dot{\phi})}, \tag{1.14}$$

where τ is the Euclidean time and the integral is over all paths that begin at $\phi(0)$ and finishe at the same point (periodic boundary condition: $\phi(\beta) - \phi(0) \in 2\pi\mathbb{Z}$). The Lagrangian in the action $S[\phi] = \int d\tau L(\phi, \dot{\phi})$ is straightforwardly connected to the Hamiltonian of Eq. (1.13) by a Legendre transformation,

$$L(\phi, \dot{\phi}) = \frac{1}{2}\dot{\phi}^2 - iA\dot{\phi}. \tag{1.15}$$

Assume that we seek a mean-field solution to approximate the value of the partition function by taking the classical path (the saddle-point solution) as the most relevant path of the problem. In addition, we can add quantum fluctuations, i.e., deviation from the classical path, to correct our solution. The classical solution is obtained from the classical Euler-Lagrange equations, $\ddot{\phi}_{cl} = 0$, which has the solution $\phi(\tau) = \frac{W 2\pi\tau}{\beta}$, $W \in \mathbb{Z}$. For the situation where $A = 0$ this answer gives $S_W = \frac{1}{2}\frac{(W2\pi)^2}{\beta}$.

At this point, we infer that classical mean-field solutions labeled by integer values (W) are separated for different values of W by *discrete energy gaps*. To understand this, remember that in classical statistical mechanics $Z = e^F$, and F is the free energy of the system. If the system is in the saddle-point solution with free energy F_W, then another solution F_{W+1} is separated by a discrete energy of the order of $\frac{1}{2}\frac{(2\pi)^2}{\beta}$. This analysis commonly appears in the study of for example instantons and the quantum tunneling problems, which explains quantum phase transitions in glassy systems.

We should also notice that the last term in the Lagrangian of Eq. (1.15) can be integrated (since it does not depend on the path) and the total partition function can be classified as the sum over

different integer value W as

$$Z = \sum_{W} e^{2\pi i W A} \int_{\phi(\beta)-\phi(0)\in 2\pi\mathbb{Z}} D\phi \; e^{-\frac{1}{2}\int d\tau \dot{\phi}^2}. \tag{1.16}$$

Treating the problem from a perturbative perspective around the mean-field solution of the theory, we can understand that modifying the path around $\phi(\tau) = \frac{W 2\pi\tau}{\beta} \rightarrow \phi + \delta\phi$ to include quantum fluctuation corrections will not change the W value intrinsic in that mean-field solution. This indicates that there are **topological sectors** that cannot be connected via short-range perturbations. The characteristic value that identifies these sectors in this example is the **winding number** W. The **topological term** of the action in this example is in the class of θ-**terms**. Also, implicitly in the argument above, is the partitioning of all possible paths into classes; in this example, the homotopy classes of the field $[\phi]$.

Mathematically speaking, in the functional integral language and in general in field theory (classical and quantum) the field ϕ is a map that is defined over a "base manifold M" and maps to a "target manifold T",

$$\phi : \mathrm{M} \rightarrow \mathrm{T}. \tag{1.17}$$

The base manifold is usually $\mathbb{R}^d$ while the target manifold is defined by the symmetries of the underlying physical many-body system. We should digress to mention what is a natural candidate for a target manifold. The target manifold is characterized by a general symmetry group G that corresponds to the symmetries of the mean-field solution of the theory. The symmetry group G is chosen such that for all elements of $g \in G$ and $\phi \rightarrow g\phi$ the action is left invariant.

However, under changing the parameter of the theory (such as temperature, magnetic field, etc.), the system undergoes a transition that reduces the G symmetry group to G/H (a coset group of

G stabilized by H), where the $H \subset G$. This "spontaneous symmetry breaking" implies a new mean-field solution or state for the many-body system. Therefore, by knowing all the coset groups G/H of the general symmetry group G, we have identified the possible target manifolds of the problem. Thus, generally, the target manifold is represented by $T = G/H$. To be less abstract, in the XY Heisenberg spin system $G = O(3)$ while $H = O(2)$. One can show that $O(3)/O(2)$ is isomorphic to $T = S^2$.

Depending on the base and the target manifold there are different classes of maps ϕ that could be defined. In our example we saw the map $\phi : S^1 \to S^1$, (S^1 is the sphere in one dimension) and the classes of $[\phi]$ were labeled by integer numbers W. In fact, one can define a "unit map" as well as an operation between different classes, $*$, and show that these classes actually form a group. In this case a **homotopy group** $\pi_1(S^1) = \mathbb{Z}$.

Finally, we should mention that for different target manifolds resulting homotopy groups are different and even may not exist. For example, for $M = S^1$ and $T = S^2$ one can intuitively understand that by deforming a path around a sphere S^2 one can go from one winding number to another, so in this case all the maps ϕ are in the same equivalence class as $''0''$, and therefore no homotopy group exists. As a general remark,in many-body quantum field theory there are many topological terms that characterize the topological features of particular problems. In addition to the winding number, there are Weiss-Zumino terms and Chern-Simons terms (in a particular case also called the Berry phase).

1.2.2 Topology in condensed matter physics

The classification of phases of matter in condensed matter physics is understood through the Ginzburg-Landau approach, which is based on characterizing the underlying symmetries that are spontaneously broken. The phenomenology of the Landau theory is that, after calculating the free

energy $F = \ln(Z)$ of the system by handling the sum over the microscopic details of the system [see, for example, Eq. (1.16)], one is left with a system where phase is defined by macroscopic order parameters; for instance, magnetic field, temperature, etc. Within the Landau theory, different phases may be accessible via tuning these order parameters.

However, the emergence of topological features in the mathematical structure of any microscopic theory implies that there are orders that can not be simply characterized by Landau'approach. These new orders are referred to as **topological orders**. Topological orders are often used in characterizing the orders in highly correlated system such as fractional quantum Hall states [7, 8].

Moreover, there are phenomena in condensed matter physics that do not involve correlations and are explained in the framework of single-particle quantum mechanics, but, nevertheless carry topological signatures. The integer quantum Hall state (QHS) is an example that lies in this category. Topological insulators can also be studied within the framework of single-particle physics of a solid. Bellow, we elaborate this example further [10].

In an insulator a gap separates the conduction band from the valence band. However, the gap property in this system is not the only quantity that distinguishes the insulating phase from other phases. In fact, a similar gap, although narrower, exists in semiconductor phase and many semiconductors and insulators can be shown to belong to the same topological classification. There exists an isomorphism that smoothly deforms the two band structures of insulator and semiconductor into one another. This equivalence can even be extended to the equivalence between an insulator and the vacuum of the Dirac theory.

To make the connection to our previous general discussion on topology in condensed matter more clear, the Bloch theorem can be viewed as a set of maps, in analogy to $[\phi(\tau)]$: from the base manifold of the "Brillouin zone", witch is a torus T^d, in k-space, to the target manifold of $\mathcal{H}(k)$ (the target manifold has at least translational symmetry). The topological classification consists of

putting all the maps that can be continuously deformed to each other without closing the gap of the insulator into the same class. Some examples frequently found in literature are listed bellow.

- *Integer Quantum Hall and the Landau flat bands:* The authors in Ref. [9] (TKNN) proved that this classification for quantum Hall states are labeled by integer Chern numbers. A Chern number in this case is given by

$$n_m = \frac{1}{2\pi} \int d^2\mathbf{k}\ \mathcal{F}_m, \tag{1.18}$$

  where $\mathcal{F}_m = \nabla \times \mathcal{A}_m = \nabla \times i\langle u_m|\nabla_k|u_m\rangle$ is known as the Berry flux.

- *Peierls instability:* Su *et al.* [13] studied solitons in polyacetylene. In this system the Peierls instability for an odd number of sites exhibits a different Berry flux than an even number, with topological excitations dominating the transport properties of the system.

- *Graphene:* Generally, a two-band model in two dimensions can be expressed as

$$\mathcal{H}(k) = \mathbf{h}(\mathbf{k}).\vec{\sigma}. \tag{1.19}$$

  Here, $\vec{\sigma} = \{\tau_x, \tau_y, \tau_z\}$ are Nambu spinors (i.e., a set of three matrices exactly the same as Pauli matrices and should not be confused with spin). In graphene, in particular, this form reduces to $\mathcal{H}(\mathbf{q}) = \hbar v_{\mathbf{F}}\mathbf{q}.\vec{\sigma} + m\sigma_z$ around the Dirac points. The Hamiltonian has time reversal symmetry Θ, while it lacks parity symmetry Π. As a result, the two masses at the two Dirac point are the same $m = m'$. Haldane [12] showed that if by assuming a magnetic field that in average is zero ($B \propto \sin(\mathbf{k}\cdot\mathbf{r})$), one can breaks the Θ symmetry but retain the Π. He showed in this case Berry flux is different and the masses are $m = -m'$. Then, the two topological classes, $m = m'$ and $m = -m'$, pertain to $\sigma_{xy} = 0$ and $\sigma_{xy} \neq 0$, respectively

  .

The importance of these topological hallmarks is the emergence of **edge states** at the boundary between two phases with different topological classifications. In a topological insulator (TI) for example, as we approach the boundaries from the bulk of the system, there will be states that appear *in the gap*. In QHS these are the chiral edge states. Their existence indicates that the topological characteristics of the bulk is about to change as we approach the boundary (say, from TI to vacuum). By modifying the edge of the physical system, for example, by adding impurities to increase scattering on the edges in QHS, one may locally perturb these states but their topological properties are invariant. In the case of edge currents where the transport is mainly carried by these edge states, a local perturbation does not affect the current [11].

There are many interesting features related to TI. So far we encountered one that was described by Haldane [12] in which Θ is broken while Π is not. In a Θ symmetric insulator, for example, one can bring in a spin-orbit coupling that lifts the Kramers' degeneracy everywhere but at the center of the Brillouin zone (since at $\mathbf{k} = 0$ there is no spin-orbit effect). In this case there are two type of edge states that inherit their topological characteristics from the bulk (*bulk-boundary correspondence*): $\mathbb{Z}_2$ TI.

Similarly, in superconductors the theory can be expressed as in Eq. (1.19), known as the De Gennes representation. In this case there is *particle-hole* symmetry (Ξ): $\Xi\mathcal{H}_{BdG}(\mathbf{k})\Xi^{-1} = -\mathcal{H}_{BdG}(-\mathbf{k})$. As we get closer to the edge where the topology must change, this symmetry leads to the existence of a **zero-mode** edge state. This implies that there must be a state with $\Gamma_0^\dagger = \Gamma_0$ (with $\Gamma^\dagger$ and Γ creation and annihilation operators, respectively). Such excitation is known as a **Majorana particle**.

The *bulk-correspondence rule* and different symmetries in different dimensions, provide a table of classifications of involved topological characteristics. These classifications are realized in physical systems such as TI, topological superconductors, QHS, etc., and are named correspondingly such

as $\mathbb{Z}$- and $\mathbb{Z}_2$-TIs, etc. (Fig. 1.2).

The subject is vast enough to cover a complete dissertation by itself [14, 15]. For the purpose of quantum computation what is offered by topological characteristics is the possibility of employing these properties as to state information and perform computation. If the information is encoded to an edge mode, small deformation, will not change the state of the information unless a quantum phase transition happens, which can be argued to be exponentially suppressed [10]. This approach to opens the door to **topological quantum computation** (see, for example, Fig. 1.3).

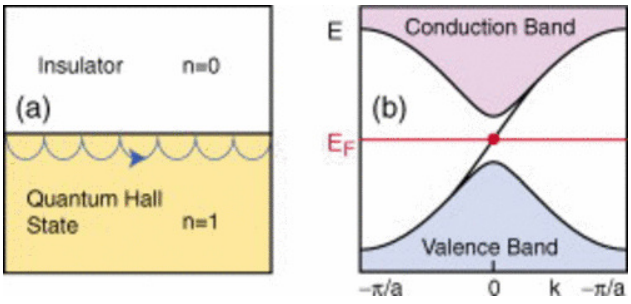

	Symmetry			*d*							
AZ	Θ	Ξ	Π	1	2	3	4	5	6	7	8
A	0	0	0	0	Z	0	Z	0	Z	0	Z
AIII	0	0	1	Z	0	Z	0	Z	0	Z	0
AI	1	0	0	0	0	0	Z	0	Z_2	Z_2	Z
BDI	1	1	1	Z	0	0	0	Z	0	Z_2	Z_2
D	0	1	0	Z_2	Z	0	0	0	Z	0	Z_2
DIII	−1	1	1	Z_2	Z_2	Z	0	0	0	Z	0
AII	−1	0	0	0	Z_2	Z_2	Z	0	0	0	Z
CII	−1	−1	1	Z	0	Z_2	Z_2	Z	0	0	0
C	0	−1	0	0	Z	0	Z_2	Z_2	Z	0	0
CI	1	−1	1	0	0	Z	0	Z_2	Z_2	Z	0

Figure 1.2: The interface between a quantum Hall state and a trivial insulator hosts a chiral edge state (top left). A boundary edge state connects the conductance band to the valence band (top right). The table of topological insulators and topological superconductors based on the bulk-boundary correspondence (bottom). From Ref. [10].

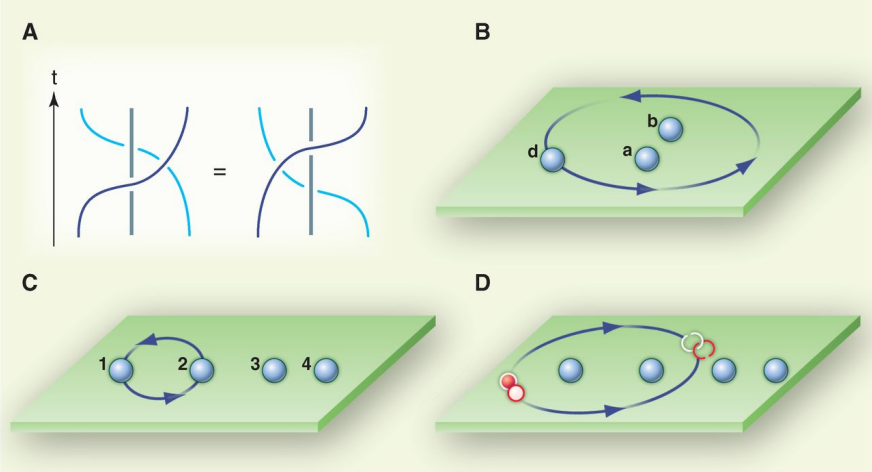

Figure 1.3: Schematic representation of braiding of non-abelian quasi-particles. From Ref. [16]. Reprinted with permission from AAAS.

CHAPTER 2: MAJORANA FERMIONS

2.1 Introduction

Here we present one of the several proposed models by Kitaev [18] with topological order with the aim of implementing topological quantum computation (TQC). The model inspired the search for *unpaired Majorana* fermions in quantum wires [17]. The idea of TQC with Majorana fermions in a wire begins with the observation that the occupation number of a fermion of a site on the wire encodes the states $|0\rangle$ and $|1\rangle$, and while a phase can also be assigned to each state, we can consider the set of sites as a collection of physical qubits $|s\rangle_j$. The scheme of unpaired Majorana describes one *logical qubit* that is encoded in this system by the the right choice of its Hamiltonian.

In this regard the single qubit flip-error σ^x is the annihilation/creation operator from $|0\rangle$ to $|1\rangle$ and vice-versa, and the phase flip σ^z is the occupation-number operator $a_j^\dagger a_j$. However, for a practical system of fermions the single flip-errors $a^\dagger$ or a become impossible to occur since we have conservation of charges. In superconducting systems this reduces to the conservation of fermionic parity $\prod_j (2a_j^\dagger a_j - 1)$ which is roughly a measure of whether the occupation number is "odd" or "even" (Reminder: in superconducting system that follows BCS theory, carriers at the Fermi sea contribute to the superconducting phase. This is the origin of the *Bogoliubv transformation* in bosonization problems like charge density waves (CDW), spin density waves (SDW), and the *Bogoliubv-de Gennes Hamiltonian*. See Ch. 2 and 6 in Ref. [4]).

In a condensed matter system where the excitations are fermions, single flip-errors appear to be suppressed due to fermionic parity conservation. But even in an non-interacting system of fermions the energy $h_j = \epsilon_j a_j^\dagger a_j$ itself would cause dephasing as the system evolves in time $|s\rangle_j \to e^{i\epsilon_j t}|s\rangle_j$ (at this point one can get the impression that if a logical qubit exists, then it must be associated to

a zero energy state $\epsilon = 0$ to stay immune from dephasing). Kitaev proposed a toy model in which the excitations of the system are the Majorana fermions, instead of fermions. As explained below, the situation in this model is different. This situation is described in Ref. [19] as: "*Electrons, from this perspective, are higher-energy composites, and looking at the system in terms of their behavior would be like doing electrical engineering with quarks.*"

Kitaev Toy Model: Consider a wire as shown in Fig. 2.1 which is governed by

$$H = \sum_j \left[-w \left(a_j^\dagger a_{j+1} + a_{j+1}^\dagger a_j \right) - \mu \left(a_j^\dagger a_j - \frac{1}{2} \right) + \Delta a_j a_{j+1} + \Delta^\star a_{j+1}^\dagger a_j^\dagger \right], \tag{2.1}$$

where w is the hopping amplitude, μ is the chemical potential, and $\Delta = |\Delta| e^{i\theta}$ is the induced superconducting gap. We also define the Majorana operators

$$c_{2j-1} = e^{i\frac{\theta}{2}} a_j + e^{-i\frac{\theta}{2}} a_j^\dagger, \tag{2.2}$$

$$c_{2j} = -ie^{i\frac{\theta}{2}} a_j + ie^{-i\frac{\theta}{2}} a_j^\dagger. \tag{2.3}$$

This convention allows us to disguise the phase of the superconducting gap Δ in the definition of Majorana fermion c. Notice that for every fermion at a site j there are two Majorana fermions.

Writing Eq. (2.1) in terms of these operators gives us

$$H = \frac{i}{2} \sum_j \left[-\mu c_{2j-1} c_{2j} + (w + |\Delta|)\, c_{2j} c_{2j+1} + (-w + |\Delta|)\, c_{2j-1} c_{2j+2} \right]. \tag{2.4}$$

Exploring different phases of the Hamiltonian in Eq. (2.4), we identify the following phases.

- **Trivial phase (Tr):** If we set $|\Delta| = w = 0$ and $\mu < 0$, then it is easy to see that $H_{\text{Tr}} = -\mu \sum_j (a_j^\dagger a_j - \frac{1}{)}2) = \frac{i}{2}(-\mu) \sum_j c_{2j-1} c_{2j}$. In this phase we have, by transforming the Hamiltonian to k-space, flat bands (Landau levels). However, we can see that Majorana

fermions on each site are coupled with the Majorana of the same site, leaving no unpaired Majorana.

- **Non-Trivial phase (NTr):** This is when $\mu = 0$ and $|\Delta| = w > 0$. In this case $H_{\rm NTr} = iw \sum_j c_{2j} c_{2j+1}$.

Comparing the two phases, in the trivial phase the fermionic parity is always $\mathcal{P} = \prod_j (-ic_{2j-1}c_{2j}) \equiv +1$ ($\mathcal{P}|\psi_{Tr}\rangle = +|\psi_{Tr}\rangle$) and the the ground state of the system is nondegenerate.

In contrast, in the non-trivial phase there are two unpaired Majorana operators c_1 and c_{2L}, where L is the linear size of the wire. Since half of an electron does not naturally exist, the combination of the two operators that can be well defined is $c_1 c_{2L}$, which commutes with the Hamiltonian of the system. Therefore, there are two degenerate ground states. In fact, $\mathcal{P}$ is exactly $\mathcal{P} = c_1 c_{2L}$ and the two ground states of the non-trivial phase correspond to the two possible parities, namely, $\mathcal{P} = \pm 1$.

How about other values of the parameter space of the Hamiltonian, μ, w, and $|\Delta|$? It is easy to see that we can write Hamiltonian of the system, Eq. (2.1), in k-space reducing it to the matrix form of Eq. (1.19). Diagonalizing the 2×2 matrix we find the bands to be $E_\pm = \pm\sqrt{(2w\cos q + \mu)^2 + 4|\Delta|^2 \sin^2 q}$.

The two extremes, trivial and non-trivial, correspond to flat bands as in the Landau levels in QHS. Kitaev argues that the phase diagram of the system is: trivial phase, $2|w| < \mu$; non-trivial phase, $2|w| > \mu$, $|\Delta| \neq 0$. Also, for general values of the parameters the unpaired Majorana fermions b' and b'' will be a superposition of the Majorana operators of all sites, in general. He concludes that any interaction between the two, $H_{int} = \frac{i}{2} t b' b''$ (that could possibly change the fermionic parity), is exponentially suppressed in the scale of the linear size of the system, $t \propto e^{-L/l_0}$.

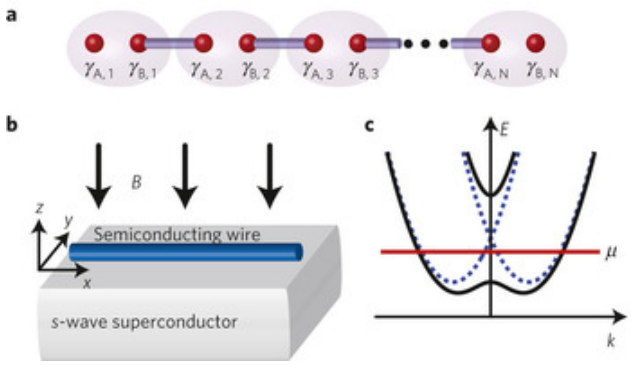

Figure 2.1: (a) A representation of the unpaired Majorana in the non-trivial phase. (b) The physical model consists of semiconductor wire on a superconductor that will induce proximity effect. (c) an attempt to tune the microscopic parameter of the model to reach the zero-mode Majorana. Source: Ref. [20]

2.2 Resilient Majorana mode in a one-dimensional spin model

- P. Jouzdani and E. R. Mucciolo, in preparation.

2.2.1 Abstract

There are mathematical equivalences between one-dimensional spin systems such as the Ising and Heisenberg XXZ models, and the Kitaev Majorana model. We study a class of one-dimensional Ising spin systems that, by a unitary transformation involving only two-qubit interactions, can be transformed into a model that has zero local order parameter, in contrast to the original Ising model, even though the $\mathbb{Z}_2$ symmetry is preserved. The degeneracy of the ground states of transformed spin model is robust against both local longitudinal and transverse fields, and the protection increases with system size. We show how the protection works using exact numerical calculation for small system sizes.

2.2.2 *Introduction*

A large effort has been made to construct more robust protocols for quantum computation by exploiting topological properties of many-body systems [21, 22]. Recently, in addition to the work done on elegant mathematical models, such as the toric and surface codes [23, 25, 24], particular attention has been given to detect and employ exotic non-Abelian excitations in order to perform quantum computation [26]. Among those, Majorana fermions are of particular interest and several systems have been proposed to host unpaired Majorana modes, such as semiconductor wires [27, 28], superconducting qubits [29], and optical lattices [30, 31].

The hunt for Majorana fermions in condensed matter physics originates from the work of Kitaev where a toy model was presented [17]. The toy model consists of a semiconductor wire interfaced with a p-wave superconductor. In that toy model two phases exists, with one hosting a non-local fermion. The non-local fermion is the sum of two Majorana operators that can appear in a two-folded degenerate mode. The model hosts one logical qubit corresponding to this two modes which is referred as the unpaired Majorana. In the same paper Kitaev argued that by a Jordan-Wigner transformation one arrives at a spin realization that hosts the two possible modes of the logical qubit of the model in its $\mathbb{Z}_2$ symmetry. Kitaev also argued that the spin realization, in contrast to the fermionic one, has an order parameter when it comes to local perturbation, and that the $\mathbb{Z}_2$ symmetry is thus broken for any value of the order parameter. Thus, the spin realization is not a promising candidate for realizing a Majorana qubit.

In the remaining sections we consider a class of one-dimensional Ising spin systems with open boundaries. While the one-dimensional Ising model has been shown to host Majorana modes after a Jordan-Wigner transformation [18, 32], we use a series of commuting two-qubit unitary transformations to reshape the Ising model onto a Hamiltonian that, in contrast to the original Ising model, does not have a local order parameter, even though the degeneracy of the ground

states is preserved. Therefore, the system is protected against both longitudinal and transverse local fields.

While the spin realization of the Kitaev toy model fails to be a good candidate to host a Majorana fermion, the transformed model provides a robust realization of a such mode. An experimental realization of the transformation required to achieve this protected state does not require more than two-spin interactions (i.e., two-qubit operations). Below, we provide a detailed description of the transformation that lends the spin model protected. We illustrate how protection takes place by evaluating numerically the energy spectrum for two short spin chains. We conclude with a brief discussion about the applicability of the model to quantum information processing.

2.2.3 The one-dimensional Ising model

The two-fold degeneracy associated with the configurations of an unpaired Majorana [22] corresponds to the topological degeneracy of the $\mathbb{Z}_2$ symmetric open-chain Ising system. The topological degeneracy of the ground state can be understood in the following way. Imagine that an applied magnetic field h_z slightly lifts the degeneracy of the two ground states $|\bar{\uparrow}\rangle = |\uparrow\uparrow \ldots \uparrow\rangle$ and $|\bar{\downarrow}\rangle = |\downarrow\downarrow \ldots \downarrow\rangle$ by an energy Δ_z. In this case, there exists a false vacuum with a slightly higher energy, say $|\bar{\uparrow}\rangle$, and a true vacuum with a slightly lower energy, $|\bar{\downarrow}\rangle$. If the spin chain is initially prepared in the false ground state $|\bar{\uparrow}\rangle$, it can nucleates into the true ground state by tunneling with a probability that falls off exponentially in the space-time distance of the nucleation and thus exponentially disappears as $\Delta_z \to 0$ [4].

A small transverse field h_y can flip a spin within the state $|\bar{\uparrow}\rangle$. Then, tunneling between the two macroscopic classical ground states occurs through a propagating domain wall, which can propagate from one end of the chain to the other. However, the tunneling amplitude associated to this transition falls off exponentially with the distance of the chain [18]. Thus, at zero temperature, a

transition between the two degenerate ground states due local external fields is strongly suppressed.

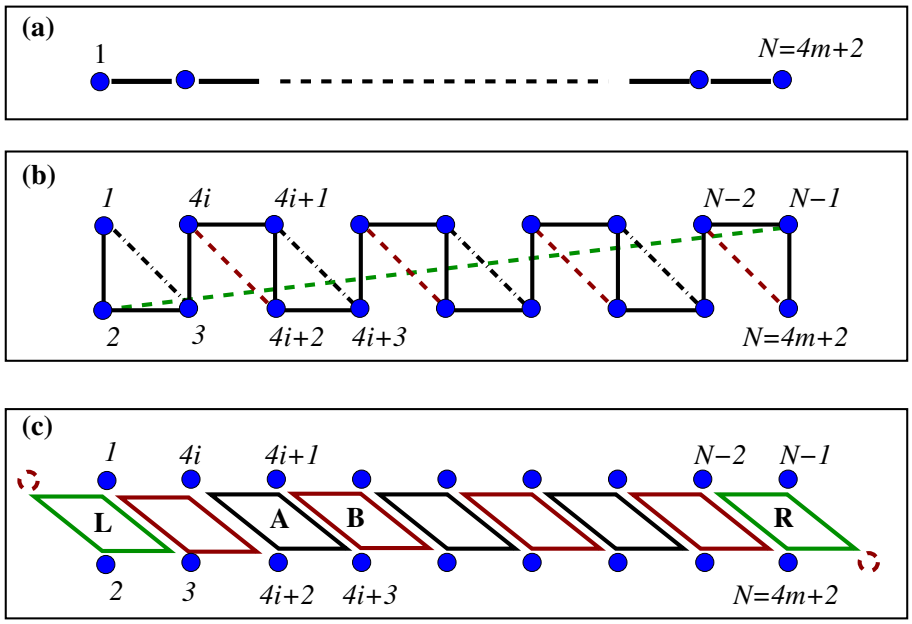

Figure 2.2: (a) The standard one-dimensional Ising model with nearest-neighbor interactions. (b) The reshaped Ising model into a ladder after the unitary transformation R in spin space. The diagonal dashed and dash-dot lines show the two-spin terms $\sigma_i^y \sigma_{i+2}^y$ used in the transformation. The term $\sigma_2^y \sigma_{L-1}^y$ is shown with a dashed line from the upper left to lower right of the ladder. (c) The Hamiltonian resulting from the transformation, H_T, has only four-spin interactions. By reshaping the chain into a ladder, we can associate the four-spin operators to plaquettes. The bulk has two different types of plaquettes, A and B. There are three operators of type A and one operator of type B. The two left and right plaquettes on the boundaries are named R and L, respectively. There are two operators acting on each of these boundary plaquettes.

The one-dimensional Ising system has an order parameter $\langle \sigma^z \rangle$ that corresponds to a net magnetization. This allows a global external field h_z to couple to the the order parameter and to destroy the coherence between the two topological degenerate states $|\bar{\uparrow}\rangle$ and $|\bar{\downarrow}\rangle$. Thus, unfortunately, this one-dimensional system is vulnerable to any finite magnetic field h_z. In addition, any of its $\mathbb{Z}_2$ broken phases is thermally unstable.

As an alternative, consider a one-dimensional spin 1/2 system of length $N = 4m+2$, with m being

a positive integer. Starting from the standard nearest-neighbor Ising Hamiltonian

$$H_I = -J \sum_{i=1}^{N-1} \sigma_i^z \, \sigma_{i+1}^z, \tag{2.5}$$

with $J > 0$, let us apply the unitary transformation

$$R(\alpha) = e^{i(\alpha/4)V}, \tag{2.6}$$

where

$$\begin{aligned} V &= \sigma_1^y \sigma_3^y + \sum_{i=1}^{N-2} \left(\sigma_{4i}^y \sigma_{4i+2}^y + \sigma_{4i+1}^y \sigma_{4i+3}^y \right) + \sigma_{N-2}^y \sigma_N^y \\ &\quad + \sigma_2^y \sigma_{N-1}^y, \end{aligned} \tag{2.7}$$

to H_I. The result is

$$\begin{aligned} H(\alpha) &= R^\dagger(\alpha) \, H_I \, R(\alpha) \\ &= \cos^2\left(\frac{\alpha}{2}\right) H_I + \cos\left(\frac{\alpha}{2}\right) \sin\left(\frac{\alpha}{2}\right) H_1 \\ &\quad + \sin^2\left(\frac{\alpha}{2}\right) H_T, \end{aligned} \tag{2.8}$$

where H_1 and H_T involve three-body and four-body interaction terms, respectively (see Appendix A). For $\alpha = \pi$, the contribution of H_1 to the total Hamiltonian drops out and we obtain

$$\begin{aligned} H(\pi) &= H_T \\ &= -J \sum_{i=1}^{m-1} \left[A_i^{(1)} + A_i^{(2)} + A_i^{(3)} \right] - J \sum_{i=0}^{m-1} B_i \\ &\quad - J \left(L_1 + R_1 + L_2 + R_2 \right), \end{aligned} \tag{2.9}$$

where we have introduced the following operators:

$$A_i^{(1)} = \sigma_{4i}^x \sigma_{4i+1}^x \sigma_{4i+2}^y \sigma_{4i+3}^y \tag{2.10}$$

$$A_i^{(2)} = \sigma_{4i}^y \sigma_{4i+1}^y \sigma_{4i+2}^x \sigma_{4i+3}^x \tag{2.11}$$

$$A_i^{(3)} = \sigma_{4i}^y \sigma_{4i+1}^x \sigma_{4i+2}^x \sigma_{4i+3}^y \tag{2.12}$$

$$B_j = \sigma_{4j+1}^y \sigma_{4j+3}^x \sigma_{4j+4}^x \sigma_{4j+6}^y \tag{2.13}$$

$$L_1 = \sigma_1^x \sigma_2^x \sigma_3^y \sigma_{N-1}^y \tag{2.14}$$

$$R_1 = \sigma_2^y \sigma_{N-2}^y \sigma_{N-1}^x \sigma_N^x \tag{2.15}$$

$$L_2 = \sigma_1^y \sigma_2^x \sigma_3^x \sigma_{N-1}^y \tag{2.16}$$

$$R_2 = \sigma_2^y \sigma_{N-2}^x \sigma_{N-1}^x \sigma_N^y \tag{2.17}$$

We denote the set formed by all these operators $\mathcal{S}$, with $i = 1, \ldots, m-2$ and $j = 0, \ldots, m-1$.

All the terms on the r.h.s. of Eq. (2.9) commute with each other. By reshaping the spin chain as shown in Fig. 2.2, one can identify $A_i^{(k)}$ and B_i as bulk plaquettes operators, while $R_{1,2}$ and $L_{1,2}$ act as boundary plaquette operators. For $N = 4m + 2$ there are $3(m-1)$ plaquettes of type A, m plaquettes of type B, and two plaquettes of types R and L each. Together, these plaquettes function as stabilizer operators and the degenerate ground states of H_T form a logical computational basis. Since there are 2^{4m+2} spin configurations and $4m + 1$ plaquette operators, the system comprised by the spin chain and the plaquette operators as observables encodes a logical Hilbert space of dimension $2^{4m+2}/2^{4m+1} = 2$.

The ground states of H_T, $|G\rangle$, have no local spin order parameter. To see that, consider that the ground states are also eigenstates of the plaquette operators of the set $\mathcal{S}$ with eigenvalue $+1$, $Q|G\rangle = |G\rangle$, where $Q \in \mathcal{S}$. Given any single-spin operator $\sigma_n^x, \sigma_n^y, \sigma_n^z$, with $n = 1, \ldots, N$, one can always find an operator Q that commutes with it. Therefore, $\langle G|\sigma_j^\alpha|G\rangle = 0$ for $\alpha = x, y, z$. As

a consequence, the system couples only weakly to external fields. Below, we illustrate this result by considering exact diagonalizations of finite spin chains.

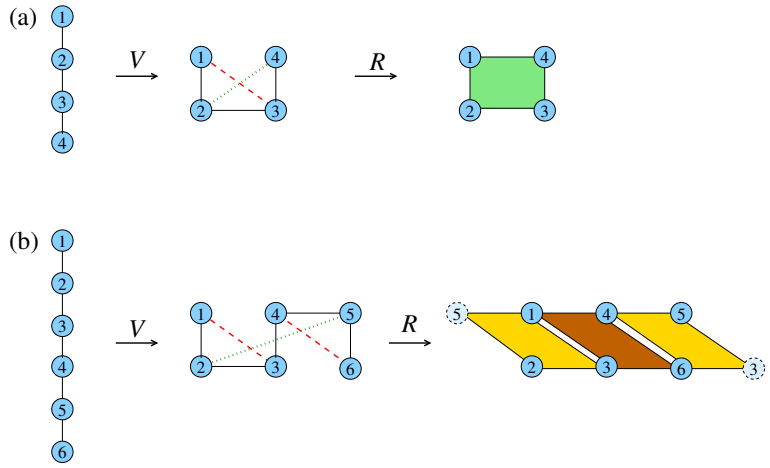

Figure 2.3: Chains of four (a) and six (b) qubits. The solid lines represent the initial Ising nearest-neighbor interaction between the spin, H_I. The dashed and dotted lines indicate the interaction terms present in V, which is used to generate the transformation R. The linear chain is reshaped to make it easier to visualize the plaquette operators, which are indicated by the filled polygons.

Examples Let us consider the Hamiltonian defined in Eq. (2.9) for two finite-size spin chains. For $N = 6$ we have

$$H_T^{(6)} = -J\,(L_1 + L_2 + B_0 + R_1 + R_2). \tag{2.18}$$

The V interaction involved in the transformation of H_I into the protected Hamiltonian $H_T^{(6)}$ is schematically shown in Fig. 2.3. This Hamiltonian has two degenerate ground states,

$$|\psi_+^{(6)}\rangle = |\uparrow\uparrow\uparrow\uparrow\uparrow\uparrow\rangle - |\downarrow\downarrow\downarrow\uparrow\downarrow\uparrow\rangle - |\downarrow\uparrow\downarrow\downarrow\uparrow\downarrow\rangle - |\uparrow\downarrow\uparrow\downarrow\downarrow\downarrow\rangle \tag{2.19}$$

and

$$|\psi_-^{(6)}\rangle = |\downarrow\downarrow\downarrow\downarrow\downarrow\downarrow\rangle - |\uparrow\uparrow\uparrow\downarrow\uparrow\downarrow\rangle - |\uparrow\downarrow\uparrow\uparrow\downarrow\uparrow\rangle - |\downarrow\uparrow\downarrow\uparrow\uparrow\uparrow\rangle. \tag{2.20}$$

Due to the small size of this example, the operators $A_i(k)$ are absent; thus, the protection in the

bulk is not complete. Nevertheless, this system has $\langle\sigma^x\rangle = \langle\sigma^y\rangle = \langle\sigma^z\rangle = 0$ for the ground states. However, expectation values involving more single-spin operators can be nonzero. For instance, $\sigma_1^x\sigma_3^y$ swaps the two ground states (up to a phase) and commutes with the operators in the set $\mathcal{S}$. Also, $\hat{Z}^{(6)}|\psi_\pm^{(6)}\rangle = \pm|\psi_\pm^{(6)}\rangle$, with $\hat{Z}^{(6)} = \sigma_2^z\sigma_3^z\sigma_4^z$. Thus, $\hat{Z}^{(6)}$ behaves as a logical σ^z operator in the two-dimensional subspace spanned by the ground states. In general, the structure of the Hamiltonian H_I is such that the logical states in this subspace are only protected up to single-spin errors. Yet, this protection increases with system size.

For the sake of comparing different system size, let us also consider $N = 4$. Even though this system does follow the $N = 4m+2$ prescription, one can identify plaquette operators that function as stabilizers (see Fig. 2.3). We have

$$H_T^{(4)} = -J\left(\sigma_1^x\sigma_2^x\sigma_3^y\sigma_4^y + \sigma_1^y\sigma_2^x\sigma_2^x\sigma_4^y + \sigma_1^y\sigma_2^y\sigma_3^x\sigma_4^x\right), \tag{2.21}$$

with the two degenerate ground states

$$|\psi_+^{(4)}\rangle = |\uparrow\uparrow\uparrow\uparrow\rangle - |\downarrow\downarrow\downarrow\downarrow\rangle \tag{2.22}$$

and

$$|\psi_-^{(4)}\rangle = |\uparrow\downarrow\uparrow\downarrow\rangle + |\downarrow\uparrow\downarrow\uparrow\rangle. \tag{2.23}$$

For this system, $\langle\sigma^x\rangle = \langle\sigma^y\rangle = \langle\sigma^z\rangle = 0$ as well.

2.2.4 Protection of H_T

The eigenenergies of the Hamiltonian $H(\alpha)$ for $N = 4$ are shown in Fig. 2.4 as a function of α. Figure 2.4a shows the energy levels in the absence of any perturbation. At $\alpha = 0$ we have the

Ising system. As α is increased, the two-fold degenerate ground states of the Ising model at $\alpha = 0$ are adiabatically connected to the two-fold degenerate ground states of H_T at $\alpha = \pi$. Figure 2.4b shows the effect of adding a uniform magnetic field, $H_Z = h_z \sum_{i=1}^{4} \sigma_i^z$. While the degeneracy in the Ising system is rapidly lifted for any value $h_z \neq 0$, the effect on H_T is significantly weaker.

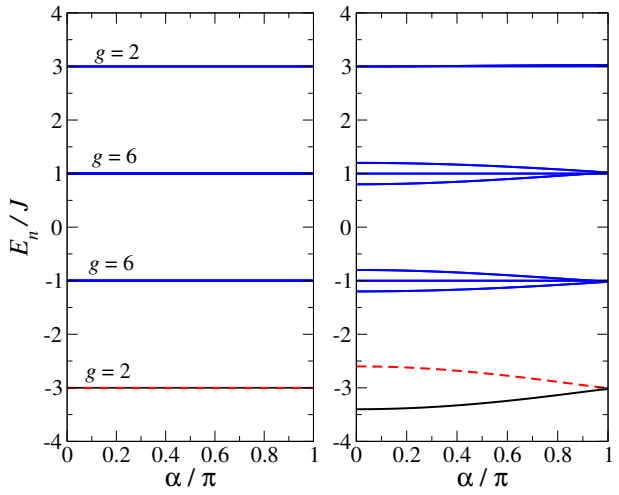

Figure 2.4: (a) The energy levels of $H(\alpha)$ in the absence of external fields for a $N = 4$ spin chain. $\alpha = 0$ corresponds to the Ising system and $\alpha = \pi$ to H_T. (b) Energy levels for the same system in the presence of a uniform longitudinal magnetic field $h_z = 0.1J$. The symbol g denotes the level degeneracy.

In fact, the dependence of the splitting of the ground states, $\Delta(\alpha) = E_+(\alpha) - E_-(\alpha)$, on global external magnetic fields allows one to verify the enhanced protection offered by H_T. The splitting for $N = 4$ at the points $\alpha = 0$ (H_I) and $\alpha = \pi$ (H_T) is shown in Figs. 2.5a and 2.5b as a function of both h_z (longitudinal) and h_y (transverse) external magnetic fields, respectively. The Z_2 symmetry (i.e., the ground state degeneracy) is lifted for any nonzero h_z for both H_I and H_T. However, there is a marked quantitative difference between them. One can see that the dependence of the splitting Δ_z goes from linear for H_I to quadratic for H_T, indicating increased protection. Figure 2.5b shows that the gap Δ_y behaves similarly for both H_I and H_T, showing a cubic dependence on the field h_y.

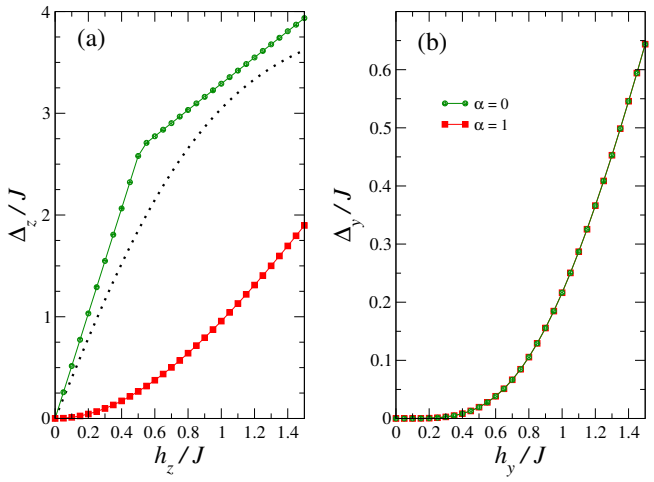

Figure 2.5: The splitting between the two low-lying states at $\alpha = 0$ (H_I, circles) and $\alpha = 1$ (H_T, squares) as a function of external field for a $N = 4$ spin chain. (a) For any non-zero longitudinal magnetic field h_z, the Z_2 symmetry is spontaneously broken. The numerical data follows closely the functional form expected for the Ising chain in the thermodynamic limit (dotted line). (b) The splitting as function of a transverse field h_y is the same for both H_I and H_T.

In Fig. 2.6 the ground state splittings for chains with $N = 4$ and $N = 6$ spins are compared. In Fig. 2.6a the comparison is with respect to longitudinal field h_z. The suppression of the splitting increases when going from $N = 4$ to $N = 6$, with the magnetic field dependence of the splitting Δ_z going from quadratic to cubic. In Fig. 2.6b, the comparison is with respect to transverse field h_y. The suppressing of the splitting is also visible in this case, with the magnetic field dependence going from fourth to sixth order in h_y.

2.2.5 Summary and discussion

We have presented a one-dimension spin model where an enhanced protection to external fields is obtained. Thus, the Majorana mode in this model is more resilient than that present in the nearest-neighbor Ising model, as well, as that in the spin version of Kitaev's model. We find that the splitting caused by external magnetic fields progressively weakens as the system size is increased.

The degenerate ground states of this model are well separated from the rest of the spectrum and can encode a logical qubit. The structure of the model Hamiltonian allows the system to self correct single-qubit errors.

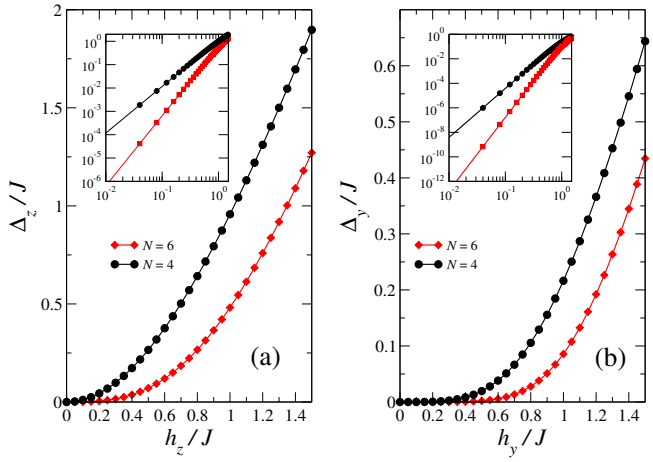

Figure 2.6: Comparison of ground state splittings for $N = 4$ and $N = 6$ spin chains as a function of external magnetic fields: (a) longitudinal, h_z; (b) transverse, h_y. The splitting is suppressed as the system size is increased.

The model studied in this chapter opens the doors to the exploration of other spin models, possibly in higher dimensions, that could also achieve enhanced protection against external perturbations by suitable unitary transformations based on two-qubit interactions. Similarly to topological schemes of passive quantum information protection, such as the toric code, the model we studied requires four-spin interactions. However, since the model is one dimensional and the only non-local interactions involve the boundaries of the spin chain, (i.e., the plaquette operators $R_{1,2}$ and $L_{1,2}$), those interactions can be made local by adopting a ring geometry.

For most low-dimensional spin models with local interactions, particularly in one dimension, thermal instability is hard to avoid. A way around this problem is to replace the always-on interactions with periodic syndrome extractions using the stabilizer operators followed by recovery operations. That would also work for our model. With the fast-paced advance seen recently for superconduct-

ing qubits [33] and other systems, this indicates that the model we introduced here could be a very good candidates for experimental studies.

CHAPTER 3: TORIC CODE

- P. Jouzdani and E. R. Mucciolo, "String localization and delocalization in the disordered toric code", American Physical Society, APS March Meeting 2012, February 27-March 2, 2012, abstract Y30.003.

3.1 Introduction

The physical system of the toric code is defined as a collection of physical qubits located on the links of a torus. The physical qubits are governed by the toric code Hamiltonian,

$$H_T = -J \sum_p \hat{B}_p - J \sum_s \hat{A}_s, \tag{3.1}$$

where

$$\hat{B}_p = \prod_{i \in p} \sigma_i^z, \quad \hat{A}_s = \prod_{i \in s} \sigma_i^x. \tag{3.2}$$

Here, $\hat{B}_p$ and $\hat{A}_s$ are called plaquettes and star operators. The geometry of the system is shown in Fig. 3.1. The torus is a square lattice of $L \times L$ dimension (L is the number of the links) with periodic boundary conditions along the width and the length. There are $N = 2L^2$ physical qubits. The operators $\hat{A}_s$ and $\hat{B}_p$ commute. In addition, there exists a set of observables of two types,

namely $\hat{X}$ and $\hat{Z}$, that are defined as

$$\hat{X}_1 = \prod_{i \in l_{x_1}} \sigma_i^x, \quad \hat{X}_2 = \prod_{i \in l_{x_2}} \sigma_i^x \tag{3.3}$$

$$\hat{Z}_1 = \prod_{i \in l_{z_1}} \sigma_i^z, \quad \hat{Z}_2 = \prod_{i \in l_{z_2}} \sigma_i^z. \tag{3.4}$$

The operators $\hat{X}_i(\hat{Z}_i)$ commute with $\hat{A}_s$ and $\hat{B}_p$ operators and, consequently, with the toric Hamiltonian. There are $L^2 - 1$ independent $\hat{B}_p$ and $L^2 - 1$ independent $\hat{A}_s$ operators.

From the perspective of the stabilizer formalism of quantum error correction (see Ch. 1), the set of operators in Eq. (3.2) (excluding two dependent operators) is a stabilizer set, S. The stabilizer subspace $C(S)$, in the 2^N-dimensional Hilbert space of the problem, is defined to be the common 2^{2L^2-2}-dimensional subspace that stabilizes the set of $2L^2 - 1$ independent plaquette and star operators (see Sec. 1.1.5).

The argument following Eq. (1.12) tells us that the $C(S)$ is $2^{2L^2}/2^{2L^2-2} = 4$-dimensional. Based on the same argument, the only operators in the set $N(S) - S$ are the logical operators $\hat{Z}$ and $\hat{X}$. This shows that for the toric code $C(S)$ the distance d is of order of $O(L)$ and the code corrects up to $L/2 - 1$ errors.

From a physical perspective, the ground state of the toric Hamiltonian in Eq. (3.1) happens naturally when all the observables corresponding to $\hat{A}_s$ and $\hat{B}_p$ are $+1$; $|\psi_o\rangle$ is the ground state of H_T if

$$\hat{B}_p|\psi_o\rangle = B_p|\psi_o\rangle = +1|\psi_o\rangle \text{ and } \hat{A}_s|\psi_o\rangle = A_s|\psi_o\rangle = +1|\psi_o\rangle, \tag{3.5}$$

for all s and all p. In other words, the ground state is obtained by a simultaneous diagonalization of all the star and plaquette operators.

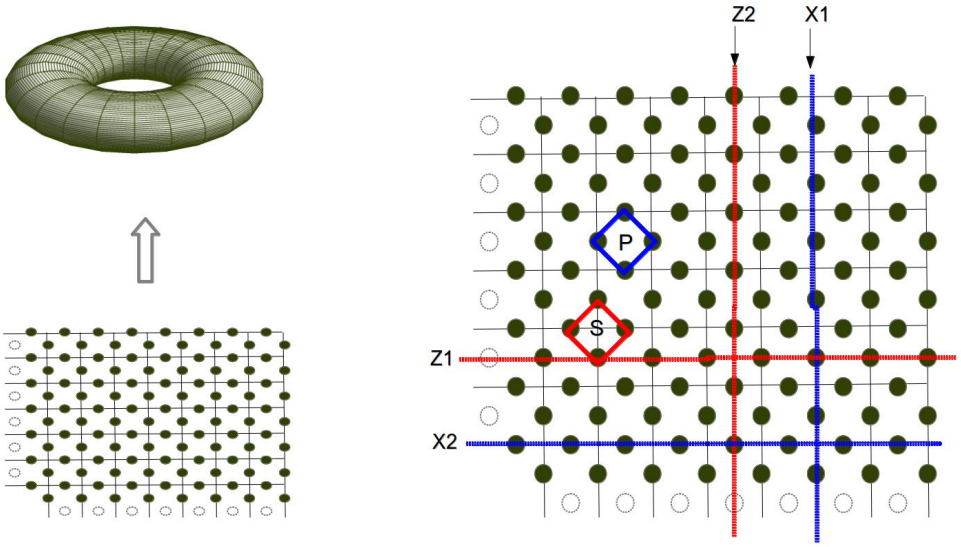

Figure 3.1: The geometry of the physical system and arrangement of qubits on the lines of a lattice (left). The stabilizers of the toric code, plaquettes and stars, are shown along with the logical operators (right) .

Since $\hat{X}_i$ ($\hat{Z}_i$) commutes with all the operators $\hat{A}_s$ and $\hat{B}_p$, a ground state must be additionally labeled by new quantum numbers indicating the eigenvalues of $\hat{Z}_1$ and $\hat{Z}_2$ (or, alternatively, $\hat{X}_1$ and $\hat{X}_2$). Therefore, each ground state has a four-fold degeneracy defined by two quantum numbers Z_1 and Z_2 such that $\hat{Z}_i|\psi_o\rangle = Z_i|\psi_o\rangle$.

The ground state of the Hamiltonian can be seen as a gas of loops containing flipped qubits. Our definition for "loops" can be explained in the following. Consider a state $|F_Z\rangle$ where all the qubits are in their $|\uparrow\rangle$ state. Then, by applying a star operator we have flipped four qubits to $|\downarrow\rangle$ states. These four qubits are on the boundary of a star and form a closed loop. This action can be repeated on the state $|F_Z\rangle$ with some arbitrary number of star operators. Each time this action creates either one or many closed loops. Finally, one can see that the ground state in Eq. (3.5) is the superposition

of all the possible distinguishable loop states created in this way.

Since applying the logical operators $\hat{Z}_i$ on $|F_Z\rangle$ gives $Z_1 = +1$ and $Z_2 = +1$, then the ground state generated in the previous paragraph has $Z_1 = +1$ and $Z_2 = +1$. Applying $\hat{X}_i$ on this ground state will give all the three other degenerate ground states, namely, $\{|\psi_o\rangle, \hat{X}_1|\psi_o\rangle, \hat{X}_2|\psi_o\rangle, \hat{X}_1\hat{X}_2|\psi_o\rangle\}$.

The energy spectrum of the toric code is gaped. It costs an energy of $2J$ to excite the system to its first excited state. A first excited state is characterized by two stabilizers with -1 eigenvalues. The physical locations of the two stabilizers are the boundaries to a string of physical qubits that actually experienced errors, which consists of *a string of Pauli matrices* $\hat{S}_{ij}^{z(x)} = \prod_{m \in S} \sigma_m^{z(x)}$. However, since only the stabilizers are observable, identification of the string of actual errors by the code formalism is not possible. See Fig. 3.2.

Recovering the corrupted code from errors could be done in the following way. If two star stabilizers $B_i = -1$ and $B_j = -1$, one needs to deliberately apply a set of σ^z errors along a string $\tilde{S}_{ij}$ that connects site i to site j. One possibility is that this string is the actual string S_{ij} that has initially caused the error. In this case applying two repeated Pauli operators, $\prod_k \sigma_k^x \sigma_k^x = 1$, and the code is recovered. If this is not the actual error then the total $\tilde{S}_{ij} \bigoplus S_{ij}$ is a closed loop; that is $\prod_{k,k'} \sigma_k^x \sigma_{k'}^x = \prod_s A_s$, product of star operators enclosed by $\tilde{S}_{ij} \bigoplus S_{ij}$ [23]. However, the loops on the torus come with two different homotopy classes; trivial, non-trivial. After a bit scrutiny we can see that the former is a product of stabilizers, while the later is a logical error. Therefore, the recovery scheme described above will work as long as the resultant is not a non-trivial loop.

In the example above the stabilizer $B_i = -1$ and $B_j = -1$ are, physically, excitations of the toric Hamiltonian. Elementary excitations of the toric Hamiltonian always come in pairs. In case of star operators these excitation are called "electric charges", while in case of plaquette operators (as in the above example) the elementary excitation are called "magnetic charges". The quasi-particles, excitations of the theory, follow a particular statistics known as non-abelian statistics.

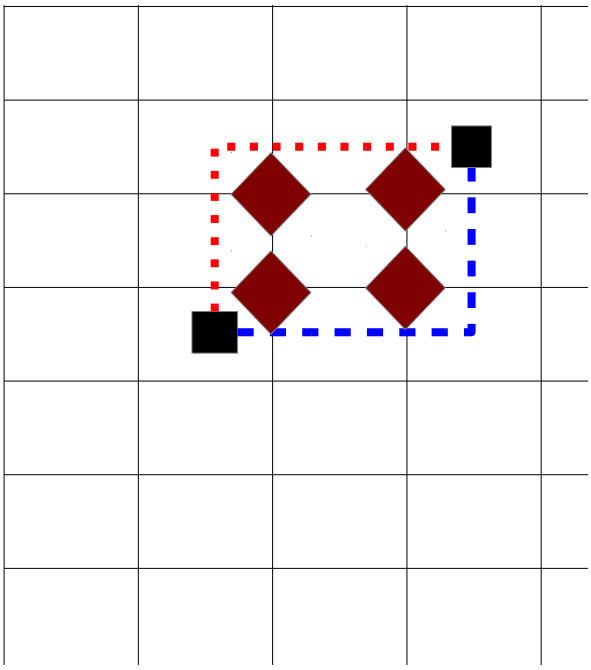

Figure 3.2: The location of two plaquettes that are detected with eigenvalues $B = -1$. Two possible actual errors ($\prod \sigma_m^x$) could have resulted in this syndrome. The two possible paths are shown in dotted and dashed lines. $\tilde{S}_{ij} \bigoplus S_{ij}$ in this example is equivalent to a product of four star operators.

3.2 Toric code in contact with a noise bath

Under a perturbation V_I one would attempt to use perturbation theory to analyze the effect. Up to the lowest order in the perturbation theory, one needs to deal with the digonalization of

$$V_I^{(1)} = \sum_{p,s} \sum_{\{S_{\{p\}},\ldots,S'_{\{s\}}\}} \langle\psi_0|\hat{S}_{\{p\}}\hat{S}_{\{s\}}\ V_I\ \hat{S}'_{\{p\}}\hat{S}'_{\{s\}}|\psi_0\rangle, \tag{3.6}$$

where the equation is read as following; $\hat{S}'_{\{s\}}|\psi_0\rangle$ is a state with an s number of e-type quasi-particles and p is the number of m-type quasi-particles. The sum $\sum_{\{S_{\{p\}},\ldots,S'_{\{s\}}\}}$ is over all the *necessary* strings (configurations of n, p errors) that generate distinct states with n, p number of errors. Finally, we have a sum over the possible errors. The situation can be complicated since many strings may result in the same configuration. Also, due to the non-abelian nature of the errors, when moving from one configuration to another, braiding of the particle must be accounted as well.

To simplify the situation we focus only on one type of errors, namely the magnetic ones. In Eq. (3.6), there are two types of elements: those connecting different sectors of n, p to n', p' with $n \neq n'$, and those connecting $\hat{S}_{\{p\}}|\psi_0\rangle$ to $\hat{S}'_{\{p\}}|\psi_0\rangle$ with the same number of charges.

The former generates more strings of error on the code if $n' > n$. Assuming an in-built quantum error correction (QEC), its task would be to correct the detected errors by "closing the loop" as mentioned previously. However, the accumulation of the strings due to the perturbation at some point will cause the QEC cycle to draw a wrong path in closing the cycles that will eventually result in a non-trivial operation on the code, namely, a logical error.

The latter accounts for the dynamics of errors within a given sector n. It is computationally difficult to monitor all the sectors for a large code system. Then, by restricting ourselves to only one sector, say $p = 2$, we can phenomenologically describe the dynamics as the physics of a hopping particle on the lattice of plaquettes. More explicitly, the perturbation in the latter case is $V_I \equiv \sum_{s,s'} t_{ss'}|\hat{S}\rangle\langle\hat{S}'|$.

Consider a complete set $\{|i_1, i_2\rangle\}$ with i_1 the lattice site (plaquettes) of the first and i_2 the lattice site of the second error. Assume a local perturbation $V_I = -h\sum_i \sigma_i^x$, and let us restrict ourselves to the sector of one string of magnetic charges. Then, from the argument above it follows that an

effective Hamiltonian is

$$V_I = -h \sum_{\langle ij \rangle} \left(c_i^\dagger c_j + c_j^\dagger c_i \right), \tag{3.7}$$

with creation, $c_i^\dagger$, and annihilation, c_i, operators of one magnetic charge at plaquette i, and $\langle ij \rangle$ are nearest-neighbor sites. We also generalize the model to situations where local impurities at each plaquette create local potentials. Finally, we assume the following Hamiltonian for the magnetic charges of the string,

$$V_I = -\sum_{\langle ij \rangle} t_{ij} \left(c_i^\dagger c_j + c_j^\dagger c_i \right) + \sum_i \left[W_i + \epsilon_i \cos(\omega t + \theta_i) \right] c_i^\dagger c_i, \tag{3.8}$$

where t_{ij} is the hopping parameter and is in general complex as $t = |t| e^{i\phi_{ij}}$. W_i are the onsite potentials. A time-dependent noise $\epsilon_i \cos(\omega t + \theta_i)$ is added. The parameter $W_i, \epsilon_i, t_{ij}, \theta_i$ are all random and their magnitudes are randomly chosen from uniform random distributions.

Our objective is to analyze the dynamics of the magnetic charges under the effective Hamiltonian Eq. (3.8). In the first step we set $t_{ij} = t$ to be constant and assume no time dependence. For this situation we calculate the distance between the two end points of the string as they evolve over time via the Hamiltonian V_I. For this we define

$$\Delta_{12}^2(t) = \langle \psi(t) | (\hat{r}_1 - \hat{r}_2) \cdot (\hat{r}_1 - \hat{r}_2) | \psi(t) \rangle. \tag{3.9}$$

The value of $|\Delta(t)|$ is numerically calculated using the Kernel Polynomial Method (KPM) expansion [36] and is shown in Fig. 3.3. The figure depicts a gradual approach to localization; from a ballistic move with no random on-site potentials (or often called random impurities) to diffusive regime and eventually localization.

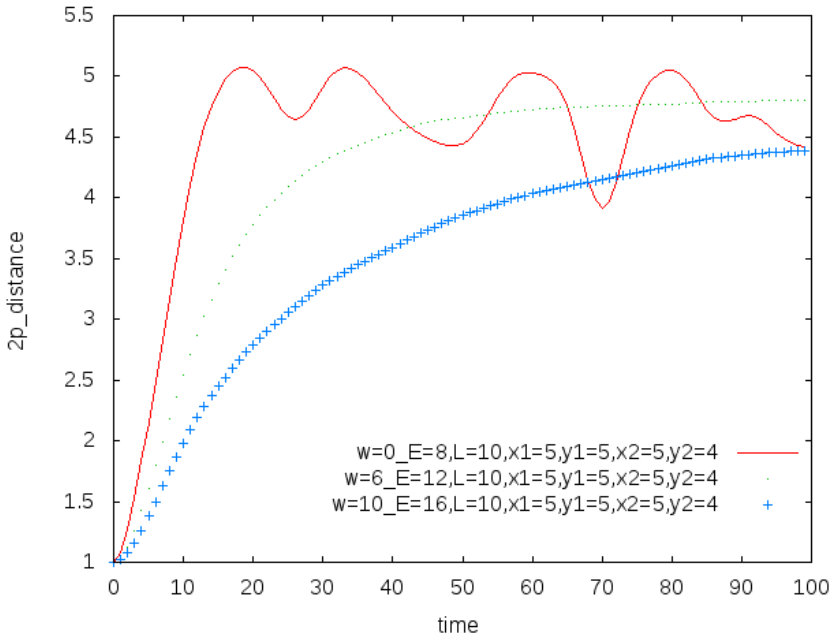

Figure 3.3: The numerical calculation of the dynamics of end-of-the string errors on toric code with $L = 10$. The errors are initially separated by one lattice site, and located in the middle of the lattice (the legend shows the initial lattice site locations) with periodic boundary conditions. The solid line (red) shows a free propagation where the two errors are not subject to random impurities. The dotted line (green) shows a modest random impurity $W/t = 1/2$, and the crossed line a higher ratio of onsite impurity $W/t = 5/8$

The distinction of the three regimes become clearer when looking at a single-particle dynamics. While errors appear as pairs, we may approximate the relative motion of the two end points as a single-particle dynamics. Then, by studying the single-particle dynamics we can achieve meaningful results on the value of the size and ratio of the strength of impurities with respect to hopping amplitude.

The behavior of error dynamics in the presence of onsite impurity can be identified by just looking at one end of the string. This can be justified by assuming that the dynamics of one of the end-of-string errors is seen from the reference frame of the other end-of-string error.

The single-particle dynamics, on the other hand, can be identified by calculating the variance

$$\Delta^2(t) \equiv \mathrm{var}(t) = \langle x^2(t)\rangle + \langle y^2(t)\rangle - \langle x(t)\rangle^2 - \langle x(t)\rangle^2, \tag{3.10}$$

which is easier to be computed numerically for larger lattice than the distance of the two anyons, as shown in Fig. 3.4. In logarithmic scale we are able to compare the slopes and identify the different propagation regimes: ballistic, diffusive, and localization of the single particle. In Fig. 3.5, it is shown how a time dependent random landscape can *delocalize* an already localized anyon.

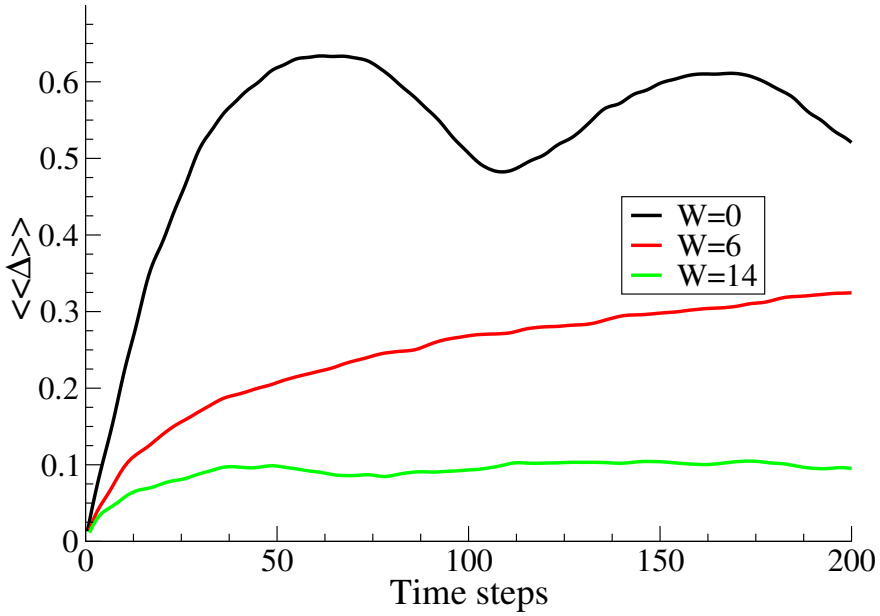

Figure 3.4: The variance Δ of a single-particle dynamics, averaged over many realizations, as a model for a single anyon on the toric code. There are three distinguished regimes; ballistic (black), diffusive (red), and localized (green).

The localization of the errors is of the Anderson type due to the destructive interference of the time-reversed paths. Moreover, by turning on the time-dependent part of V_I, the localized particle can be delocalized. This happens due to decoherence that the random time-dependence potential induces. The numerical result is shown in Figs. 3.5 and 3.6.

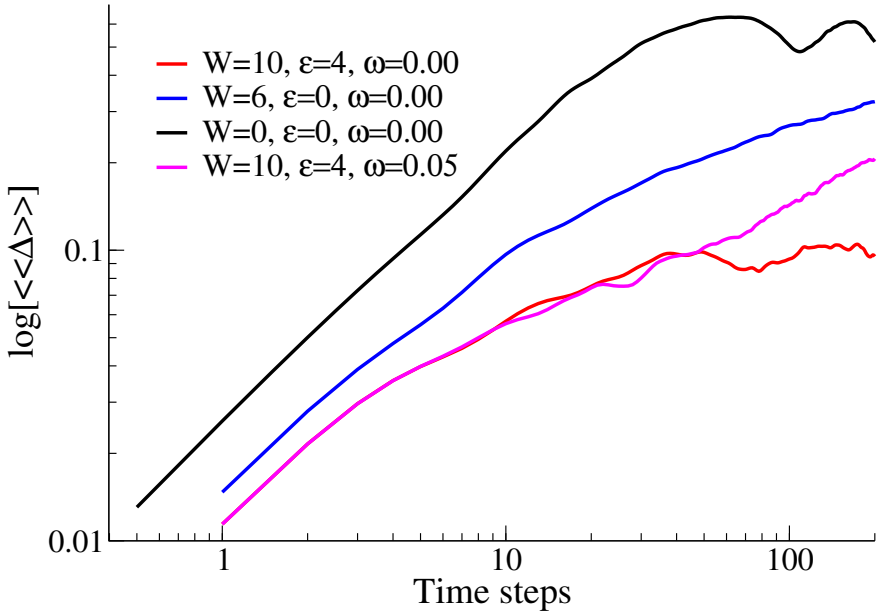

Figure 3.5: The variance with respect to time steps in a logarithmic scale ($L = 50$). The three regimes of ballistic, diffusive and localized are shown in black, blue, and red, respectively. By turning the time varying noise the localized anyon becomes delocalized (pink).

Finally, we compare the different ratios of time-independent and time-dependent random impurity strengths, and analyze the localization/delocalization transition (see Fig. 3.6).

The results obtained indicate the possibility of confining propagating anyons simply by adding randomness to the toric code system. While the overall gap is still preserved, the perturbative randomness can cause the anyons or the charge particles (errors) to be localized, making them easier to be detected and corrected.

However, we observe that a noisy environment represented by a time-dependent potential can adversely delocalize the errors, reestablishing a diffusive regime that can result in the winding of the errors around the torus and thus cause a logical error. We conclude that the random impurity approach to confine errors can be effective, but due to possibility of time-dependent noise it can not fully solve the problem of logical errors.

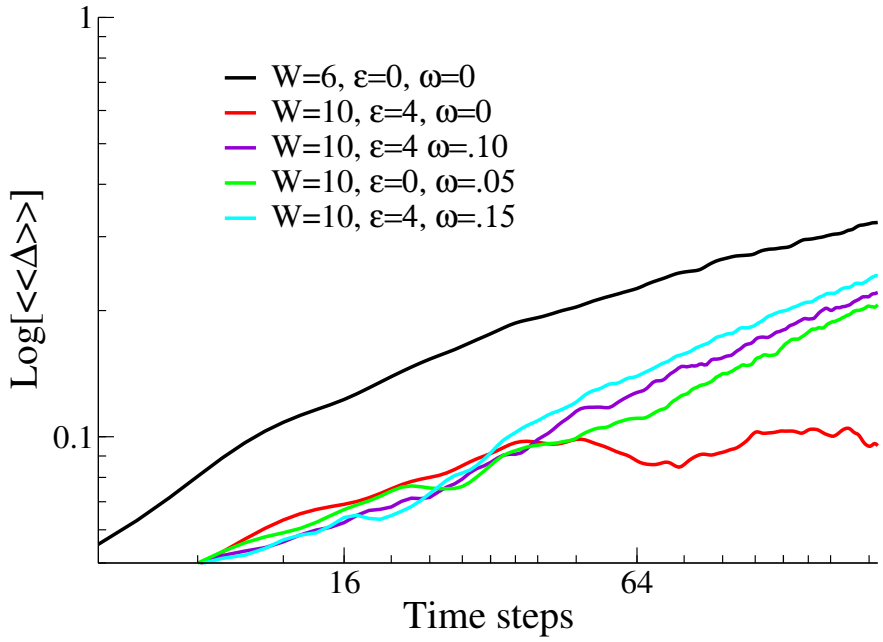

Figure 3.6: Comparison of delocalization from a localized state $W = 10$ (red line) at different frequencies ω (color lines) with the diffusive regime $W = 6$ (black line) on a lattice with $L = 50$.

CHAPTER 4: FIDELITY OF THE SURFACE CODE IN THE PRESENCE OF A BOSONIC BATH

- P. Jouzdani, E. Novais, and E. R. Mucciolo, "Fidelity of the surface code in the presence of a bosonic bath", Physical Review A **88**, 012336 (2013).

4.1 Abstract

We study the resilience of the surface code to decoherence caused by the presence of a bosonic bath. This approach allows us to go beyond the standard stochastic error model commonly used to quantify decoherence and error threshold probabilities in this system. The full quantum mechanical system-bath dynamics is computed exactly over one quantum error correction cycle. Since all physical qubits interact with the bath, space-time correlations between errors are taken into account. We compute the fidelity of the surface code as a function of the quantum error correction time. The calculation allows us to map the problem onto an Ising-like statistical spin model with two-body interactions and a fictitious temperature which is related to the inverse bath coupling constant. The model departs from the usual Ising model in the sense that interactions can be long ranged and can involve complex exchange couplings; in addition, the number of allowed configurations is restricted by the syndrome extraction. Using analytical estimates and numerical calculations, we argue that, in the limit of an infinite number of physical qubits, the spin model sustain a phase transition which can be associated to the existence of an error threshold in the surface code. An estimate of the transition point is given for the case of nearest-neighbor interactions.

4.2 Introduction

Recent progress in implementing controllable multiqubit systems in the laboratory has sparked renewed interest in topological quantum computing schemes. Particular attention has been devolted to the surface code [24, 51, 23], which is a planar version of Kitaev's toric code [25]. From a physical implementation viewpoint, the surface code has two important advantages in comparison to other schemes: (i) all gates are local, and (ii) simulations indicate that the topological protection yields very high tolerance for errors. The latter is based entirely on stochastic models for errors. These models point to error threshold probabilities per single qubit operation or cycle ranging from 1% [53, 52], when only nearest neighbor interactions and no perfect gates are assumed, up to 19% [91], when the ability to perfectly measure four-qubit operators is assumed. The large error threshold comes at the expense of hardware: a vast number of local operations and physical qubits is required to build a useful computing machine [54]. Yet, this tradeoff seems attractive nowadays for a number of physical realizations such as cold atoms [55], ion traps [56], Rydberg atoms [57], semiconductor systems [58], and superconducting integrated systems [59].

Most error threshold estimates so far have relied on the assumption of errors being uncorrelated in time and space. However, given the large-scale integration that will be required to implement a surface code, this assumption seems unwarrantable on physics grounds. The need to have tens of millions of physical qubits siting on a common substrate and interacting with each other and with the controlling electronics is very likely to introduce environmental modes, which will effectively couple the time evolution of the physical qubits. Under these circumstances, errors will become correlated and it is unclear whether the system will retain its high error threshold. In fact, previous studies of the impact of correlated errors on standard (non-topological) quantum computing codes have shown that error thresholds may be reduced or altogether disappear in some situations [60, 61, 62, 63, 64, 65]. Investigating the effect of correlations between errors in the surface code is the

main goal of this paper.

In a recent paper [66], it has been shown that the time evolution of the surface code in the presence of a common bosonic bath can be mapped onto a statistical spin model. This mapping allows for the computation of the surface code fidelity much in the same way that one computes the partition function and expectation values in a spin model. As a result, the existence of an error threshold was related to the existence of a phase transition in the statistical model. Even though the interpretation of the crossing of the error threshold as a classical phase transition is not new [67, 23], our formulation is novel since it takes into account the full quantum mechanical time evolution of the qubits in the presence of a dynamical environment. In addition, rather than evaluating error probabilities, we compute directly the fidelity of the logical qubit. Our choice of environment, a collection of freely propagating massless bosonic modes, is realistic for systems where decoherence can be related to the coupling to phonons, magnons, and electromagnetic modes.

Below, we provide a detailed derivation of the evolution operator of the combined surface code–bosonic bath system. We focus our attention on a single quantum error correction cycle and assume that, after the syndrome extraction, the bath is reset to its ground state. Within this approximation, we find that the fidelity can be written as a function of the expectation value of single-qubit logical operators. The study of these expectation values can be related to the physics of an Ising-like spin model with a complex fictitious temperature. Under the assumption of non-cyclic and perfect stabilizer measurements, we use both exact and mean-field finite numerical calculations to argue that the spin model sustains a thermodynamic phase transition in the limit of an infinite number of physical qubits. System with 25 and 41 qubits are studied numerically. The critical temperature of the spin model yields a coupling constant threshold value which is found to depend mainly on bath parameters.

The chapter is organized as follows. In Sec. 4.3 we give a brief introduction to the essential

elements of the surface code and set some of the notation used later. Section 4.4 presents a Hamiltonian formulation of the problem in terms of bosonic modes coupled to physical qubits which allows us to obtain a compact form for the evolution operator of the combined logical qubit–bath system. The evolution operator involves a bath correlation function which is explicitly evaluated for three representative situations. The effect of syndrome extraction on the evolution operator is described in Sec. 4.5 and an expression for the fidelity in terms of expectation values involving qubit operators is derived in Sec. 6.6. The mapping of the fidelity calculation onto a statistical model is given in Sec. 4.7 and the connection between the fictitious critical temperature and the error threshold probability is shown in Sec. 4.8. In Sec. 4.9 we estimate the fictitious critical temperature via a low-temperature expansion. Numerical supporting the existence of an error threshold are shown in Sec. 4.10, which is a very encouraging result. Conclusions and a critical discussion of the approximations involved and future directions of investigation are drawn in Sec. 4.11. A number of appendices with technical details of the calculations are also provided at the end of this dissertation.

4.3 Surface code

Following Ref. [24], we define the surface code as collection of N spins 1/2 (physical qubit systems) located on the edges of a two-dimensional lattice with two types of boundaries, as shown in Fig. 4.1. The lattice comprises n and m qubit rows and columns, respectively. Measurements are done on two types of stabilizer operators: stars $A_{\Diamond}$, which are associated to lattice vertices ($\Diamond$),

$$A_{\Diamond} = \prod_{i \in \Diamond} \sigma_i^x, \tag{4.1}$$

and plaquettes $B_{\square}$, which are associated to tiles ($\square$), including the ones at the open boundaries,

$$B_{\square} = \prod_{i \in \square} \sigma_i^z. \tag{4.2}$$

In Eqs. (6.18) and (6.19), the Pauli spin operators $\vec{\sigma}_i$ act on qubits. Thus, there are $N_{\square} = (n+1)m$ plaquette operators and $N_{\Diamond} = (m+1)n$ star operators. The N physical qubits store one logical qubit. There are $n_L = 2$ distinct logical operators: $\bar{X}$ and $\bar{Z}$. They are formed by a string of physical qubit operators along paths that cut through the lattice:

$$\bar{Z} = \prod_{i \in \Gamma_Z} \sigma_i^z \tag{4.3}$$

and

$$\bar{X} = \prod_{i \in \Gamma_X} \sigma_i^x \tag{4.4}$$

where Γ_Z runs between qubits at opposite open boundaries (left to right), passing through vertices along the way, while Γ_X runs between qubits at opposite closed boundary (top to bottom), crossing tiles (see Fig. 4.1). Notice that vertices and tiles form dual lattices.

The protected code space contains two states, $\left|\bar{\uparrow}\right\rangle$ and $\left|\bar{\downarrow}\right\rangle$. Both states are eigenstates of all stabilizer operators with eigenvalue $+1$. Errors can be inferred by measuring the stabilizer operators and tracking down which stars or plaquettes yielded -1 values. A decoding procedure is needed to decide which recovering operation to perform [70, 71].

The code state can be generated by the action of a product involving all star operators on the z ferromagnet state, namely,

$$\left|\bar{\uparrow}\right\rangle = G|F_z\rangle. \tag{4.5}$$

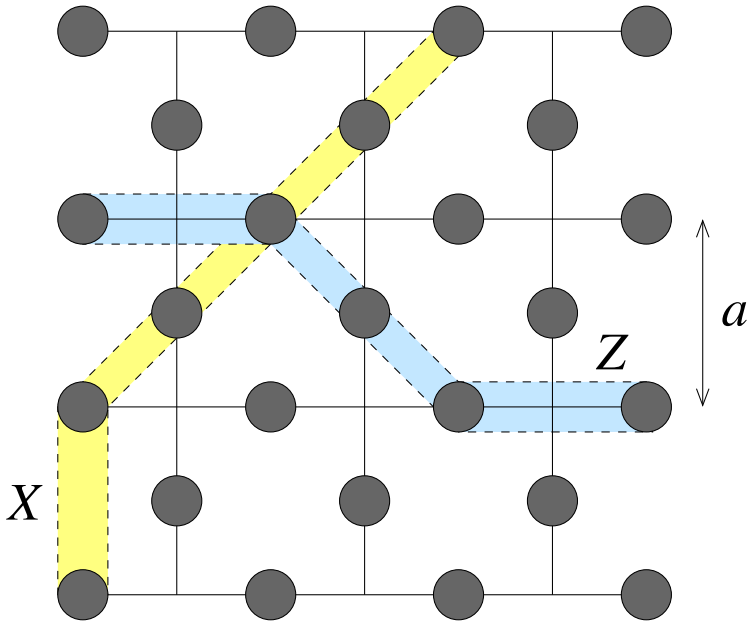

Figure 4.1: A 3×3 two-dimensional square lattice structure for a surface code. Physical qubits (circles) are located at the edges of the lattice, which has open (vertical) and closed (horizontal) boundaries. In the general case, the lattice is $n \times m$ in size, with nm vertical and $(n+1)(m+1)$ horizontal edges and $N =$ physical qubits. The light colored strips show possible paths for the logical operators $\bar{Z}$ and $\bar{X}$. a is the lattice constant.

Likewise

$$\left|\bar{\downarrow}\right\rangle = G\bar{X}|F_z\rangle, \tag{4.6}$$

where

$$G = \frac{1}{\sqrt{2^{N_\Diamond}}} \prod_{\Diamond} (1 + A_\Diamond) \tag{4.7}$$

and

$$|F_z\rangle = \prod_{i=1}^{N} |\uparrow\rangle_{i,z}. \tag{4.8}$$

Notice that the product in Eq. (4.7) can be expanded as

$$\prod_{\Diamond} (1 + A_\Diamond) = 1 + \sum_{\Diamond} A_\Diamond + \sum_{\Diamond_1 \neq \Diamond_2} A_{\Diamond_1} A_{\Diamond_2} + \ldots. \tag{4.9}$$

The number $2^{N_\Diamond}$ appearing in the prefactor of G is the number of terms appearing in the expansion: $2^{N_\Diamond} = \binom{N_\Diamond}{0} + \binom{N_\Diamond}{1} + \cdots + \binom{N_\Diamond}{N_\Diamond}$.

4.4 The bosonic environment

The most general bath model would allow for both flip and phase errors to occur. However, only perturbative calculations would be possible in this general case. Since our goal is to obtain nonperturbative results, we focus our discussion on flip errors only (it is possible to rephrase the model to induce only pure dephasing model by a simple change of basis). We do not explicitly consider correlated errors introduced by the hardware upon measurement, but rather errors induced by the interaction between a bath and the qubits during the time span of a QEC cycle. The Hamiltonian we consider is written as

$$H = H_0 + V, \tag{4.10}$$

where H_0 is a free bosonic Hamiltonian,

$$H_0 = \sum_{\mathbf{k}\neq 0} \omega_{\mathbf{k}}\, a^\dagger_{\mathbf{k}} a_{\mathbf{k}}, \tag{4.11}$$

and

$$V = \frac{\lambda}{2} \sum_i f\left(\mathbf{r}_i\right) \sigma^x_i, \tag{4.12}$$

where $\mathbf{r}_i$ denotes the spatial location of a qubit i and f is a local bosonic operator,

$$f\left(\mathbf{r}\right) = \frac{\left(v/\omega_0\right)^{D/2+s}}{L^{D/2}} \sum_{\mathbf{k}\neq 0} |\mathbf{k}|^s \left(e^{i\mathbf{k}\cdot\mathbf{r}} a^\dagger_{\mathbf{k}} + e^{-i\mathbf{k}\cdot\mathbf{r}} a_{\mathbf{k}}\right). \tag{4.13}$$

Here, D is the bath spatial dimension, v is the bosonic mode velocity, $\omega_{\mathbf{k}} = v|\mathbf{k}|$, and ω_0 is a characteristic frequency of the bath (notice that f is dimensionless since we adopt units such

that $\hbar = 1$). The creation and annihilation operators of the bosonic modes follow the standard commutation relations, namely, $[a_{\mathbf{k}}, a^{\dagger}_{\mathbf{k}'}] = \delta_{\mathbf{k},\mathbf{k}'}$ and $[a_{\mathbf{k}}, a_{\mathbf{k}'}] = [a^{\dagger}_{\mathbf{k}}, a^{\dagger}_{\mathbf{k}'}] = 0$.

The choice of s depends on the physical nature of the environment and on which bosonic degree of freedom couples to the qubits. When the qubits couple directly to the bosonic displacement field, we choose $s = -1/2$, whereas when they couple to the bosonic current operator, we choose $s = 1/2$ instead. Notice that these two choices allow us to write the coupling between the qubits and the bosonic environment as a simple function of the free bosonic field. Hence, they render an interaction Hamiltonian with commutators that are subluminal, namely, which are equal to zero outside the boson light cone (see below). But this is not the general rule. For instance, a model that couples the environment to two different qubit components would render an interaction Hamiltonian with non-subluminal commutators (regardless of our choice for s).

This apparent problem comes from the fact that we usually think of errors in a dynamical sense: they happen in a point in space-time and create bosons that propagate at the speed of light. However, this is an incorrect interpretation to the equations we are about to derive. We will not be considering pulses propagating thought a medium, but rather looking at allowed normal modes of the bath and how they relate to different qubits configurations. If there is no fundamental symmetry reason for their suppression, long-wave length modes of the bath will in general introduce superluminal effective interactions. A very simple way to highlight this fact is to rewrite the bosonic model in a coherent state basis, $a_{\mathbf{k}} = \tilde{a}_{\mathbf{k}} + \alpha$, where $\tilde{a}_{\mathbf{k}}$ and $\tilde{a}^{\dagger}_{\mathbf{k}}$ also obey standard commutation relations and α in a constant. This procedure introduces an effective instantaneous interaction between the qubits as much as the Coulomb gauge introduces the instantaneous Coulomb interaction in quantum electrodynamics.

For a time interval Δ, the error model comprised by Eqs. (4.10) to (4.12) leads to the following

evolution operator in the interaction picture [62]:

$$U(\Delta) = T_t \, \exp\left[-i\frac{\lambda}{2}\int_0^\Delta dt \sum_i f\left(\mathbf{r}_i, t\right)\sigma_i^x\right]. \tag{4.14}$$

Combining a Magnus expansion with the Zassenhaus formula (see Appendix B), we arrive at a remarkably simple expression for the evolution operator,

$$U(\Delta) = \chi \, \exp\left[-\frac{\lambda^2}{2}\sum_{i\neq j}\Phi_{\mathbf{r}_i\mathbf{r}_j}(\Delta)\,\sigma_i^x\sigma_j^x\right] : \exp\left[-\frac{i\lambda}{2}\sum_i F_{\mathbf{r}_i}(\Delta)\,\sigma_i^x\right] :, \tag{4.15}$$

where

$$\Phi_{\mathbf{rs}}(\Delta) = \frac{1}{2}\left[\mathcal{G}_{\mathbf{rs}}^{(R)}(\Delta) + \mathcal{G}_{\mathbf{rs}}^{(I)}(\Delta)\right], \tag{4.16}$$

$$\chi = \exp\left[-\frac{\lambda^2}{4}\sum_i \Phi_{\mathbf{r}_i\mathbf{r}_i}(\Delta)\right], \tag{4.17}$$

and :: stands for normal ordering. In Eqs. (4.15) and (4.16), we have introduced two bath correlation functions,

$$\begin{aligned}\mathcal{G}_{\mathbf{rs}}^{(I)}(\Delta) &= \frac{1}{2}\int_0^\Delta dt_1 \int_0^{t_1} dt_2 \left\{\left[f\left(\mathbf{r}, t_1\right), f\left(\mathbf{s}, t_2\right)\right]\right. \\ &\quad \left. + \left[f\left(\mathbf{s}, t_1\right), f\left(\mathbf{r}, t_2\right)\right]\right\}\end{aligned} \tag{4.18}$$

and

$$\mathcal{G}_{\mathbf{rs}}^{(R)}(\Delta) = \langle 0|F_{\mathbf{r}}(\Delta)\, F_{\mathbf{s}}(\Delta)|0\rangle, \tag{4.19}$$

and the auxiliary bosonic field

$$F_{\mathbf{r}}(\Delta) = \int_0^\Delta dt\, f\left(\mathbf{r}, t\right). \tag{4.20}$$

(Notice that χ is a real number since $\mathcal{G}_{\mathbf{rr}}^{(I)} = 0$.)

Below, we present the functional form of the correlations functions for two-dimensional bosonic baths ($D = 2$). Details of the calculations are provided in Appendices C and D. We consider three representative values of the power s which appears in the qubit-bath coupling constant dependence on the bath mode momentum [see Eq. (4.13)]. These values are $s = -1/2$, 0, and $s = 1/2$, corresponding to subohmic, ohmic, and superohmic baths, respectively. This classification is standard and follows from the bath's spectral function frequency dependence at low frequencies: sublinear (subohmic), linear (ohmic), and superlinear (superohmic) [68]. Also, see Appendices C and D.

4.4.1 Subohmic bath

For two-dimensional subohmic baths ($D = 2$ and $s = -1/2$), the bath correlation function takes a simple closed form. The real part reads

$$\begin{aligned}\mathcal{G}^{(R)}_{\mathbf{rs}}(\Delta) &= -\frac{|\mathbf{r}-\mathbf{s}|}{\pi v\omega_0} + \frac{\Delta}{2\omega_0}\theta(v\Delta - |\mathbf{r}-\mathbf{s}|) \\ &\quad + \frac{\Delta}{\pi\omega_0}\theta(|\mathbf{r}-\mathbf{s}| - v\Delta)\left[\arcsin\left(\frac{v\Delta}{|\mathbf{r}-\mathbf{s}|}\right) + \sqrt{\frac{|\mathbf{r}-\mathbf{s}|^2}{(v\Delta)^2} - 1}\right], \end{aligned} \tag{4.21}$$

where $\theta(x)$ denotes the Heaviside step function. The imaginary part reads

$$\begin{aligned}\mathcal{G}^{(I)}_{\mathbf{rs}}(\Delta) &= \frac{-i\Delta}{\pi\omega_0}\,\theta(v\Delta - |\mathbf{r}-\mathbf{s}|) \\ &\quad \times \left\{\ln\left[\sqrt{\frac{(v\Delta)^2}{|\mathbf{r}-\mathbf{s}|^2} - 1} + \frac{v\Delta}{|\mathbf{r}-\mathbf{s}|}\right] - \sqrt{1 - \frac{|\mathbf{r}-\mathbf{s}|^2}{(v\Delta)^2}}\right\}. \end{aligned} \tag{4.22}$$

4.4.2 Ohmic bath

Choosing $D = 2$ and $s = 0$, the real and imaginary parts of the bath correlation function take the forms [69]

$$\mathcal{G}^{(R)}_{\mathbf{rs}}(\Delta) = \frac{1}{\pi\omega_0^2} \operatorname{arcosh}\left(\frac{v\Delta}{|\mathbf{r}-\mathbf{s}|}\right) \theta(v\Delta - |\mathbf{r}-\mathbf{s}|), \tag{4.23}$$

and

$$\begin{aligned}\mathcal{G}^{(I)}_{\mathbf{rs}}(\Delta) &= \frac{i}{\pi\omega_0^2}\left[\frac{\pi}{2}\,\theta(v\Delta - |\mathbf{r}-\mathbf{s}|)\right. \\ &\quad \left. + \arcsin\left(\frac{v\Delta}{|\mathbf{r}-\mathbf{s}|}\right)\theta(|\mathbf{r}-\mathbf{s}| - v\Delta)\right].\end{aligned} \tag{4.24}$$

Notice that the real part of the correlation function vanishes for distances larger than $v\Delta$. For this bath as well as others, the number of qubits within the spatial range of the correlation function is determined by the ratio $v\Delta/a$, where a is the surface code lattice constant.

4.4.3 Superohmic bath

Choosing $D = 2$ and $s = 1/2$, we find for the real part

$$\mathcal{G}^{(R)}_{\mathbf{rs}}(\Delta) = \frac{v}{\pi\omega_0^3}\left[\frac{1}{|\mathbf{r}-\mathbf{s}|} - \frac{\theta(|\mathbf{r}-\mathbf{s}| - v\Delta)}{\sqrt{|\mathbf{r}-\mathbf{s}|^2 - (v\Delta)^2}}\right]. \tag{4.25}$$

For the imaginary part we find

$$\mathcal{G}^{(I)}_{\mathbf{rs}}(\Delta) = \frac{iv}{\pi\omega_0^3}\frac{\theta(v\Delta - |\mathbf{r}-\mathbf{s}|)}{\sqrt{(v\Delta)^2 - |\mathbf{r}-\mathbf{s}|^2}}. \tag{4.26}$$

A schematic representation of the spatial dependence of these correlations functions is shown in

Fig. 4.2

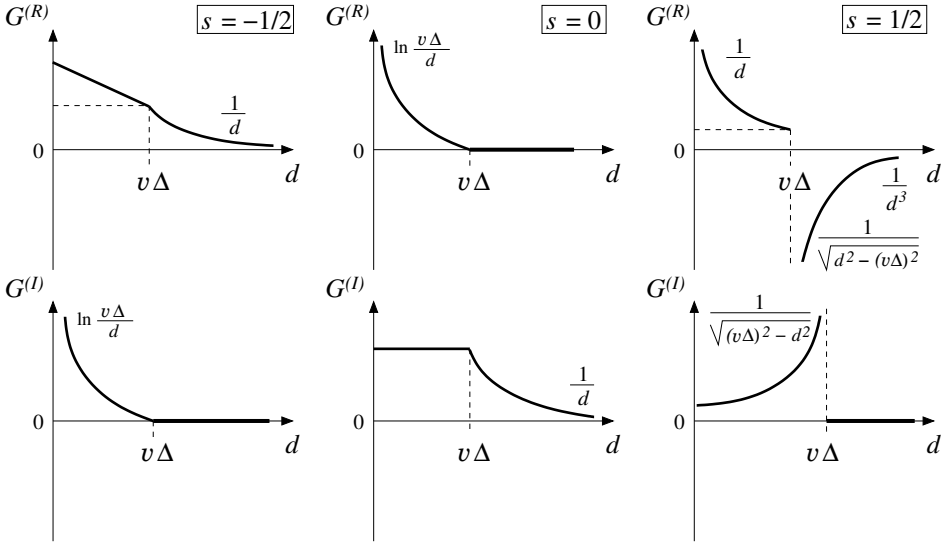

Figure 4.2: Schematic representation of the spatial dependence of the correlation functions $\mathcal{G}^{(R)}_{\mathbf{rs}}(\Delta)$ and $\mathcal{G}^{(I)}_{\mathbf{rs}}(\Delta)$ for $s = -1/2$, 0, and $1/2$. We use $d = |\mathbf{r} - \mathbf{s}|$.

4.5 Syndrome extraction

Let us assume that the system is prepared initially in the logical state $\left|\bar{\uparrow}\right\rangle$ and the boson field initial state is the vacuum,

$$|\Psi_0\rangle = (G|F_z\rangle) \otimes |0\rangle_b. \tag{4.27}$$

We then let the system evolve under the interaction Hamiltonian until a time Δ, when an error correction protocol is performed flawlessly. The syndrome extraction operator is equivalent to the application of the projector

$$P = \frac{1}{2^{N_\square} 2^{N_\Diamond}} \prod_{\square} (1 + b_\square B_\square) \prod_{\Diamond} (1 + a_\Diamond A_\Diamond)\,, \tag{4.28}$$

where $a_\square = \pm 1$ and $b_\lozenge = \pm 1$ are the syndromes for each star and plaquette operator, respectively. Since we are assuming only bit-flip errors, the projection over stars is just the identity for $a_\lozenge = 1$, namely,

$$P = \frac{1}{2^{N_\square}} \prod_\square \left(1 + b_\square B_\square\right). \tag{4.29}$$

Using that $A_\lozenge G = G$ and $\left[\bar{X}, G\right] = 0$, we can rewrite the projector in a slightly different form,

$$P = R \left|\bar{\uparrow}\right\rangle \left\langle\bar{\uparrow}\right| R + R \left|\bar{\downarrow}\right\rangle \left\langle\bar{\downarrow}\right| R, \tag{4.30}$$

where R is the recovery operation chosen to be performed.

In principle, we should consider all possible syndrome outcomes. However, it is useful to look at the most benign evolution and assume $b_\square = 1$. Such an evolution corresponds to the system remaining in the vacuum of the gauge fields after a time Δ. This nonerror syndrome provides an upper bound to the available computational time. In addition, it simplifies the calculations by removing from consideration a recovery operation that tries to steer the system back to the computational basis [70, 71, 72]. Thus, for this particular case,

$$P = \left|\bar{\uparrow}\right\rangle \left\langle\bar{\uparrow}\right| + \left|\bar{\downarrow}\right\rangle \left\langle\bar{\downarrow}\right|. \tag{4.31}$$

The environment state is unaffected by the error correction protocol. If no extra step is taken to dissipate excitations that pile up over time, the environment will keep a memory of events that happened during the QEC period. Keeping track of such excitations between QEC cycles in a fidelity calculation is a difficult task even for simple, non-topological logical qubit systems [61, 62, 64]. For topological qubits, the task is considerably harder due to the exponential number of terms that enter in the composition of the computational states.

Thus, in order to make the formulation amenable to an analytical calculation, we consider an extra step to the QEC protocol. In addition to projecting the quantum computer wave function back to the logical Hilbert space, we assume that at the end of the QEC step the environment is reset to its ground state. This is equivalent to imposing at the end of the QEC step the projector $\lim_{T_{\rm bath}\to 0} e^{-H_0/k_B T_{\rm bath}}$, for some environment temperature $T_{\rm bath}$ defined with respect to some even larger reservoir.

A consequence of this extra QEC hypothesis is that we exclude from the calculation any spatial correlation between QEC periods, as well as memory and spatial correlations between the time evolution of bras and kets. This new projector operator can be conveniently written as

$$P' = |\Psi_0\rangle\langle\Psi_0| + \bar{X}|\Psi_0\rangle\langle\Psi_0|\bar{X}. \tag{4.32}$$

After the projection, the wave function must be normalized again. For this purpose, consider the normalization factor

$$\left\langle \Psi_0 \left| U^\dagger(\Delta) P' U(\Delta) \right| \Psi_0 \right\rangle = |\mathcal{A}|^2 + |\mathcal{B}|^2 , \tag{4.33}$$

where

$$\mathcal{A} = \left\langle \Psi_0 \left| U(\Delta) \right| \Psi_0 \right\rangle \tag{4.34}$$

and

$$\mathcal{B} = \left\langle \Psi_0 \left| \bar{X} U(\Delta) \right| \Psi_0 \right\rangle . \tag{4.35}$$

Below, we use the expectation values $\mathcal{A}$ and $\mathcal{B}$ to compute the surface code fidelity after one QEC cycle.

4.6 Fidelity

The fidelity of the surface code after one QEC cycle can be defined as

$$F \equiv |\langle \Psi_{\mathrm{QEC}} | \Psi_0 \rangle|, \tag{4.36}$$

where $|\Psi_0\rangle$ is the initial state of the qubit system and the bath and

$$|\Psi_{\mathrm{QEC}}\rangle = P' U(\Delta) |\Psi_0\rangle . \tag{4.37}$$

The expectation values $\mathcal{A}$ and $\mathcal{B}$ now come in handy since they allow one to obtain a simple expression for the fidelity,

$$\begin{aligned} F &= \left[\frac{\langle \Psi_0 | P' U(\Delta) | \Psi_0 \rangle \langle \Psi_0 | U^\dagger(\Delta) P' | \Psi_0 \rangle}{\langle \Psi_0 | U^\dagger(\Delta) P' U(\Delta) | \Psi_0 \rangle} \right]^{1/2} \\ &= \left[\frac{\langle \Psi_0 | U(\Delta) | \Psi_0 \rangle \langle \Psi_0 | U^\dagger(\Delta) | \Psi_0 \rangle}{|\mathcal{A}|^2 + |\mathcal{B}|^2} \right]^{1/2} \\ &= \frac{|\mathcal{A}|}{\sqrt{|\mathcal{A}|^2 + |\mathcal{B}|^2}} \\ &= \frac{1}{\sqrt{1 + \frac{|\mathcal{B}|^2}{|\mathcal{A}|^2}}}, \end{aligned} \tag{4.38}$$

where we used that $P' |\Psi_0\rangle = |\Psi_0\rangle$. Thus, our task of determining the fidelity is reduced to evaluating the ratio $|\mathcal{B}|^2/|\mathcal{A}|^2$.

4.7 Mapping onto a statistical model

Let us first consider the cases where the bath correlation function $\Phi_{\mathbf{rs}}(\Delta)$ has both real and imaginary parts finite, namely, $0 < D + 2s < 3$. The insertion of the evolution operator given by Eq. (4.15) into Eqs. (4.34) and (4.35) results in very compact expressions for $\mathcal{A}$ and $\mathcal{B}$ since these expectation values are taken on the bosonic vacuum. After a short manipulation, we arrive at

$$\mathcal{A} = \chi \left\langle F_z \left| e^{-\beta \mathcal{H}} G^2 \right| F_z \right\rangle \tag{4.39}$$

and

$$\mathcal{B} = \chi \left\langle F_z \left| \bar{X} e^{-\beta \mathcal{H}} G^2 \right| F_z \right\rangle, \tag{4.40}$$

where we introduced

$$\mathcal{H} = \frac{\lambda^2}{2\beta} \sum_{i \neq j} \Phi_{\mathbf{r}_i \mathbf{r}_j}(\Delta)\, \sigma_i^x \sigma_j^x \tag{4.41}$$

and

$$\beta = \frac{1}{2\pi} \left(\frac{\lambda}{\omega_0} \right)^2 \frac{1}{(\omega_0 \Delta)^{D+2s-2}}. \tag{4.42}$$

Clearly, Eq. (4.41) can be interpreted as an effective interaction between qubits intermediated by the environmental bosons. The connection to a statistical model becomes more apparent when we consider that the ferromagnetic state along the z direction can be expanded in in the x basis, namely,

$$|F_z\rangle = \prod_{i=1}^{N} \left(\frac{|\uparrow\rangle_{i,x} + |\downarrow\rangle_{i,x}}{\sqrt{2}} \right). \tag{4.43}$$

Inserting this expression into Eqs. (4.39) and (4.40), we arrive at

$$\mathcal{A} = \frac{\chi}{2^N} \sum_S e^{-\beta E_S} \left\langle S \left| G^2 \right| S \right\rangle \tag{4.44}$$

and

$$\mathcal{B} = \frac{\chi}{2^N} \sum_S e^{-\beta E_S} \left\langle S \left| \bar{X}\, G^2 \right| S \right\rangle , \tag{4.45}$$

where S stands for the eigenstates of the operator $\prod_{i=1}^{N} \sigma_i^x$ and

$$\beta E_S = \langle S | \beta \mathcal{H} | S \rangle . \tag{4.46}$$

Notice that the expectation values in Eqs. (5.26) and (5.27) vanish for those states $|S\rangle$ where at least one start operator has a -1 eigenvalue. Therefore, those equations can be rewritten as

$$\mathcal{A} = \frac{\chi}{2^N} \sum_{S'} e^{-\beta E_{S'}} \tag{4.47}$$

and

$$\mathcal{B} = \frac{\chi}{2^N} \sum_{S'} e^{-\beta E_{S'}} \left\langle S' \left| \bar{X} \right| S' \right\rangle , \tag{4.48}$$

where the sums are over the subset of states S' where *all* star operators take positive values:

$$\langle S' | A_\Diamond | S' \rangle = +1. \tag{4.49}$$

It is clear now that $\mathcal{A}$ is proportional to the partition function of a classical statistical spin model with a restricted configuration space. Then, $\mathcal{C}$ is equal to the expectation value of the operator $\bar{X}$ in this model.

The statistical model defined by Eqs. (4.41), (4.46), (4.47), and (4.48) is nontrivial in a number of ways. First, the interaction term (4.41) is not purely real. Second, the interaction range is not necessarily restricted to nearest neighbors. Third, the constraint imposed by Eq. (4.49) severely reduces the size of the configuration space.

Since $\left\langle S' \left| \bar{X} \right| S' \right\rangle$ can only take the values ± 1, one can rewrite Eqs. (4.47) and (4.48) as sums over

"energy" eigenvalues, namely,

$$\mathcal{A} = \frac{\chi}{2^N} \sum_{E'} \left[g^+(E') + g^-(E') \right] \, e^{-\beta E'} \tag{4.50}$$

and

$$\mathcal{B} = \frac{\chi}{2^N} \sum_{E'} \left[g^+(E') - g^-(E') \right] \, e^{-\beta E'}, \tag{4.51}$$

where $g^{\pm}(E')$ are the number of qubit configurations with energy E' and $\langle \bar{X} \rangle = \pm 1$. The prime indicates that only configurations where all star operators have $+1$ expectation value are considered, Eq. (4.47).

When the sums in Eqs. (4.50) and (4.51) are not restricted by Eq. (4.47), the time-reversal symmetry of the Hamiltonian implies $g^+(E) = g^-(E)$ for logical operators $\bar{X}$ containing an odd number of σ_i^x qubit operators. Therefore, in this case, $\mathcal{B} = 0$. For $\bar{X}$ containing an even number of σ_i^x operators, for each "energy" eigenvalue E, $\langle \bar{X} \rangle$ is either $+1$ [and $g_-(E) = 0$] or -1 [and $g_+(E) = 0$], but the value of $\mathcal{B}$ cannot be predicted.

In the case of a restricted sum, it is straightforward to see that the separation of configurations in time-reversal symmetry classes is not useful. Consider that at the vertical boundaries one can form operators $A_\diamondsuit$ with three qubits. In this case, even if a certain configuration $|S'\rangle$ satisfies Eq. (4.47), its time-reversal partner will not and therefore will not be included in Eqs. (4.50) and (4.51). Thus, the restriction is equivalent to projecting out time-reversal partner of $|S'\rangle$.

As explained in Ref. [66], one useful way to understand this point is to break up the states $\{|S'\rangle\}$ into two groups, $\{|S'_+\rangle\}$ and $\{|S'_-\rangle\}$, where

$$|S'_+\rangle = \prod_j B_\square |F_x\rangle \tag{4.52}$$

and

$$|S'_-\rangle = \bar{Z}_\Gamma |S'_+\rangle. \tag{4.53}$$

Here, $\prod_j B_\square$ is a product of all plaquette operators that do not touch the logical error $\bar{Z}_\Gamma$ for a given path Γ. It is then possible to show that this separation leads to the appearance of an effective local magnetic field that acts only on the qubits along the path Γ. This local magnetic field leads to the time-reversal symmetry breaking in the computation of the expectation values in Eqs. (4.50) and (4.51).

4.7.1 Effective interaction and fictitious temperature

The parameter β plays the role of inverse temperature in the statistical model. From Eq. (4.42), we see that β is proportional to λ^2, thus serving as a measure of the strength of the coupling between the qubits and the environment. The effective exchange interaction amplitude, J_{ij}, depends on the bath characteristics (e.g., spatial dimension and spectral density), on the QEC cycle duration Δ, and on the ratio $a/(\Delta v)$.

For instance, consider the ohmic bath, where

$$\beta = \frac{1}{2\pi}\left(\frac{\lambda}{\omega_0}\right)^2 \tag{4.54}$$

Using Eqs. (4.23) and (4.24), the effective Hamiltonian of the statistical model can be written as

$$\mathcal{H} = \sum_{i \neq j} J_{ij}\, \sigma_i^x \sigma_j^x, \tag{4.55}$$

with

$$J_{ij} = \frac{1}{2} \times \begin{cases} \operatorname{arcosh}\left(\frac{v\Delta}{|\mathbf{r}_i - \mathbf{r}_j|}\right) + \frac{i\pi}{2}, & \frac{|\mathbf{r}_i - \mathbf{r}_j|}{v\Delta} < 1, \\ i \arcsin\left(\frac{v\Delta}{|\mathbf{r}_i - \mathbf{r}_j|}\right), & \frac{|\mathbf{r}_i - \mathbf{r}_j|}{v\Delta} > 1. \end{cases} \tag{4.56}$$

The real part of J_{ij} is nonzero only between qubits within the light cone of the bosonic modes. The imaginary part is present for any pairs of qubits, but decays rapidly (approximately with the cube of the inverse distance) when qubits are outside the light cone. For a lattice of size L, an extreme limit occurs when $v\Delta \sim L$, in which case all qubits are correlated. In the opposite limit, when the QEC cycle period Δ is sufficiently short (or, equivalently, that the lattice constant is large enough), so that $a/\sqrt{2} < v\Delta < a$, only qubits belonging to the same plaquette are within the light cone defined by the free spatial propagation of the bosonic modes and the real part of the coefficient J_{ij} vanishes beyond nearest neighbors.

4.8 Connecting β to the qubit error probability

It is useful to relate the fictitious inverse temperature β of the spin model to the probability p of a qubit flipping its spin state during the QEC cycle. The latter can be defined as

$$p = \langle 0| \otimes \langle \uparrow_j |U_j^\dagger(\Delta)| \downarrow_j \rangle \langle \downarrow_j |U_j(\Delta)| \uparrow_j \rangle \otimes |0\rangle, \tag{4.57}$$

where $\{|\uparrow_j\rangle, |\downarrow_j\rangle\}$ are states of the qubit located at $\mathbf{r}_j$, $|0\rangle$ is the bath ground state, and

$$U_j(\Delta) = T_t \exp\left[-\frac{\lambda}{2}\int_0^\Delta dt\, f(\mathbf{r}_j, t)\, \sigma_j^x\right] \tag{4.58}$$

is the evolution operator of that qubit coupled to the bath when the dynamics of all other qubits is frozen. The steps in the evolution of Eq. (4.57) are similar to those used in the derivation of the

fidelity. The details are provided in Appendix E. The result is

$$p = \frac{1}{2}\left\{1 - \exp\left[-\frac{\lambda^2}{4}\,\mathcal{G}^{(R)}_{\mathbf{r}_j\mathbf{r}_j}(\Delta)\right]\right\}. \tag{4.59}$$

Notice that for $\lambda = 0$, $p = 0$. As the coupling between qubits and bath grows in magnitude, p approaches 1/2, which signals a complete randomization of the qubit state.

The functional relation between p and the fictitious temperature β can be easily established by evoking Eq. (4.42) and employing the explicit form of $\mathcal{G}^{(R)}_{\mathbf{r}_j\mathbf{r}_j}(\Delta)$ as given in Eq. (C.1). One obtains

$$\ln(1-2p) = -\frac{\pi\beta(v\Delta)^{D+2s-2}}{L^D}\sum_{\mathbf{k}\neq 0}|\mathbf{k}|^{2s-2}[1-\cos(|\mathbf{k}|v\Delta)]. \tag{4.60}$$

The sum over momentum diverges in the ultraviolet when $D+2s \geq 2$ and the relation between the error probability and the fictitious inverse temperature becomes cutoff dependent. For instance, for $D = 2$ and $s = 0$ (ohmic bath), one finds $p = \frac{1}{2}\left[1 - (2v\Delta\Lambda)^{-\beta/2}\right]$, where Λ is the ultraviolet momentum cutoff. However, for $D = 2$ and $s = -1/2$ (subohmic case), one finds $p = \frac{1}{2}\left(1 - e^{-\pi\beta/4}\right)$, which is cutoff independent.

4.9 Estimate of β_c

We now provide an estimate of the critical inverse fictitious temperature, taking a slightly different approach from that used in Ref. [66]. Let us consider the case when the effective spin coupling in Eq. (4.41) is real and only nearest-neighbor interactions occur, $\Phi_{\mathbf{r}_i\mathbf{r}_j}(\Delta) = J$ for $|\mathbf{r}_i - \mathbf{r}_j| \leq a/\sqrt{2}$ and $\Phi_{\mathbf{r}_i\mathbf{r}_j}(\Delta) = 0$ otherwise. We will carry out a low-temperature (large β) expansion of Eqs. (4.50) and (4.51). The key element we exploit in this expansion is the following property of the surface code: At the boundaries of the surface code, the star operators are defined by three qubits instead of four. This means that if a certain state $|S\rangle$ is included in the restricted sums defining

$\mathcal{A}$ and $\mathcal{B}$, its time-reversed counterpart is included. This is because reversing all the qubit of a configuration with an eigenvalue $+1$ for all star operators yields a -1 eigenvalue for the star operators at the boundaries.

This property is particularly useful in the limit of $\beta \to \infty$ when the term with the minimum energy, $e^{-\beta E'_{\min}}$, carries the leading contribution to the sums. For $\beta \to \infty$ and for $J < 0$, the only state with minimum energy is a ferromagnetic state where all spins are pointing along the positive x direction, $|F_x\rangle$. Since the the ferromagnet state with spins pointing along the negative x is not part of the restricted sum, $g^-(E'_{\min}) = 0$. In this limit, the spin model is in the ordered phase, with $\mathcal{A} = \mathcal{B}$, resulting in $\mathcal{F} = 1/2$ (lost fidelity).

Consider now a large but finite β. Starting from the state $|F_x\rangle$, the states appearing in $\mathcal{A}$ and $\mathcal{B}$ can be separated into two groups, as shown in Eqs. (4.52) and (4.53). The first group, $\{S'_+\}$, corresponds to the states counted in $g^+(E')$, whereas the second group, $\{S'_+\}$, is accounted for by $g^-(E')$. Therefore, $g^-(E')$ is equal to the number of states of energy E' with a logical error $\bar{Z}_\Gamma$ for a given path Γ. At large β, the energy cost of these states is of the order of the length of $\bar{Z}_\Gamma$ and they are suppressed in comparison to other states. The leading terms contributing to the sums are the minimum energy state $|F_x\rangle$ and the states $|S'_+\rangle$ containing only small loops. However, as the system size increases the multiplicity factor $g^+(E')$ increases as well. Its value is proportional to the number of ways one can apply the $\bar{Z}$ operation, or equivalently, to the number of self-avoiding walks (SAW) from one open boundary to its opposite. The number of SAWs with a length l, is related to connective constant μ of the lattice and scales as μ^l.

If the multiplicity factor $g^-(E')$ is high enough, it can compensate the Boltzmann factor suppression. Then, as β decreases to a certain value β_c, for some energy $E'_\star$ a term of the type $\mu^{l_{\bar{Z}}(E'_\star)}\, e^{-\beta_c E'_\star}$ will appear in $\mathcal{B}$ with the same order as the leading term related to the $|S'_+\rangle$ states,

namely, $e^{-\beta_c E'_{\min}}$. Here, $l_{\bar{Z}}$ is the length of $\bar{Z}$. This criterion provides a crude estimate for β_c:

$$e^{-\beta_c E'_{\min}} \approx \mu^{l_{\bar{Z}}(E'_\star)}\, e^{-\beta_c E'_\star}, \tag{4.61}$$

leading to

$$\beta_c \approx \frac{l_{\bar{Z}}(E'_\star)\, \ln \mu}{E'_\star - E'_{\min}}. \tag{4.62}$$

The difference between $E'_\star$ and $E'_{\min}$ is proportional to the length of the logical error $\bar{Z}$. Then, the denominator is of the order of $2n\, l_{\bar{Z}} J$, where n is the number of qubits interacting with the qubits comprising the logical error $\bar{Z}$ through the Hamiltonian in Eq. (4.55). A range of possible values for the connective constant of a square lattice can be found in the literature. If we adopt $\mu = 2.64$ [73], set $n = 4$, and insert these values into Eq. (4.62), we obtain $\beta_c J \approx 0.12$.

4.10 Numerical evaluation of the fidelity

In light of Sec. 4.7, we can interpret the ratio $\mathcal{B}/\mathcal{A}$ as the expectation value of the $M_x = \sum_{j\in\Omega} \sigma_j^x$, namely, the x magnetization of a linear set of spin 1/2 particles embedded into a spin system governed by the Hamiltonian of Eq. (4.55) with the restriction imposed by Eq. (4.47). (Here, Ω denotes the path defining the logical error $\bar{X}$.) In the absence of such a restriction, the computation of $\mathcal{B}/\mathcal{A}$ in the thermodynamic limit would follow standard procedures used in Statistical Mechanics. The restriction, however, makes an analytical computation rather difficult, if not impossible. Therefore, we resort to numerical calculations, both exact and approximate, to find how $\mathcal{B}$ and $\mathcal{A}$ (and thus the fidelity $\mathcal{F}$) behave as a function of β and how this behavior scales with increasing system sizes.

Below, we focus on the case where the effective interaction strength J_{ij} is real and only involves nearest-neighbor qubits. As mentioned earlier, this special case is of significance to experiments

where $v\Delta$ is of the order of a. Short-range correlated errors in this case can be introduced by any measurement or operation on individual stars and plaquettes.

4.10.1 Exact calculations

For two lattice sizes, $N = 25$ and 41, we computed $\mathcal{A}$ and $\mathcal{B}$ for an $\bar{X}$ operator that ran vertically through the middle of the lattice. The computation was done by exhaustive enumeration of all orthogonal qubit configurations $|S\rangle$ that complied with the constraint $\langle S|G^2|S\rangle \neq 0$, namely, that produced only positive plaquette eigenvalues. We verified that the results were insensitive to the choice of operator $\bar{X}$. The resulting fidelity is shown in Fig. 4.3 as a function of the inverse fictitious temperature β. For small β (equivalent to small coupling constant λ), the fidelity stays close to 1 after one QEC cycle. As β increases, the fidelity decays and tends asymptotically to $1/\sqrt{2}$, which is expected when $\mathcal{B} = 0$. Another important feature is that the transition from $\mathcal{F} = 1$ to $\mathcal{F} = 1/\sqrt{2}$ becomes sharper as the system size is increased. This is the expected behavior when, in the thermodynamic, infinite-size limit, a phase transition occurs at some critical value of β.

We have tested that this behavior is not substantially altered when the coupling constant J gains a constant imaginary part. The results are shown in Fig. 4.4. The main effect of adding an imaginary part is to create oscillations in the decay of the fidelity as a function of β. The larger the magnitude of the imaginary part in J, the more oscillations are observed. However, the relative amplitude of these oscillations decrease with increasing system size. In the limit of a large number of physical qubits, we expect that the oscillations to be relatively small and concentrated near the critical value β_c.

In order to determine the critical value β_c, we resort to the coherent anomaly method, which has been extensively and successfully used to determine critical temperatures in interacting spin systems [74, 75].

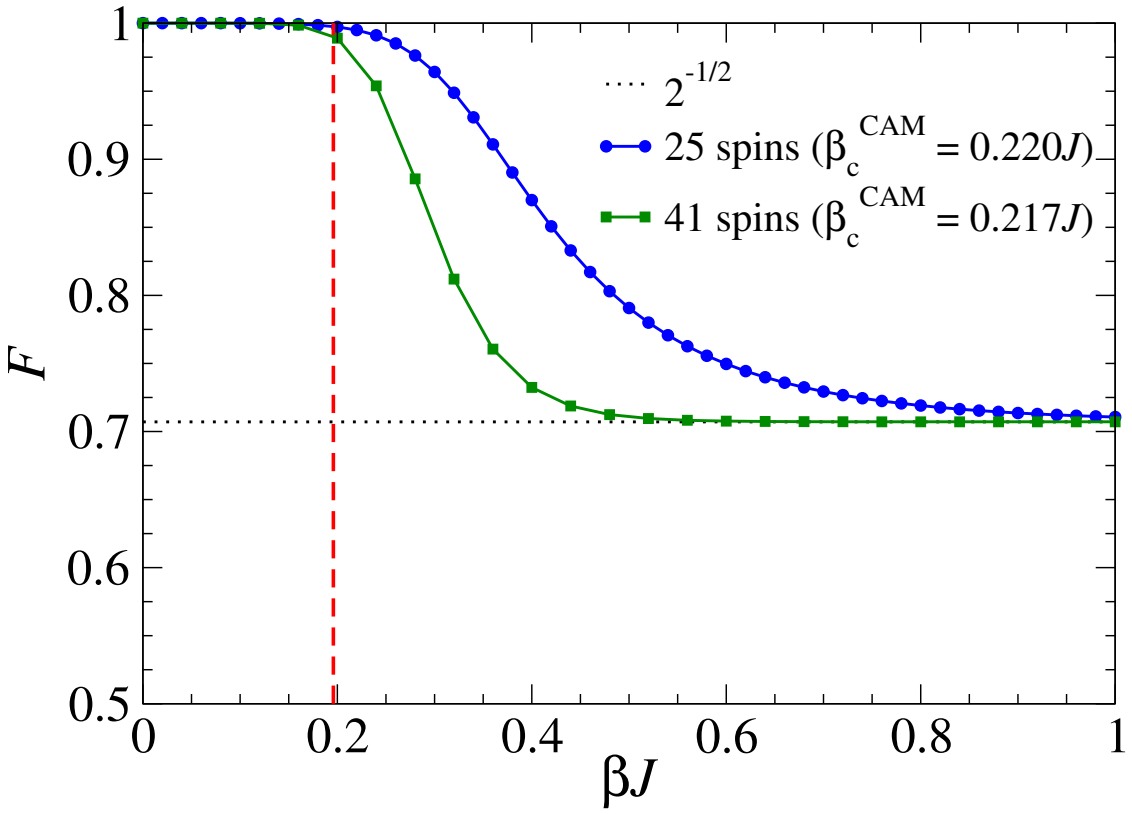

Figure 4.3: Surface code fidelity of code spaces of 25 and 41 physical qubits in contact with a bosonic bath when star operators are restricted to positive values ($A_\diamondsuit = 1$).

4.10.2 Mean-field solution: coherent anomaly method

In the coherent anomaly method (CAM), a cluster of interacting spins is embedded inside a mean-field medium. Self-consistency is obtained by allowing the spins at the boundary of the cluster to experience the mean field, which is set equal to the mean value of the central spin in the cluster. This constraint provide an equation from which the critical temperature can be determined. As the cluster size is increased, the expectation is that the critical temperature obtained in this way rapidly approaches the exact value of an infinite-size system [74, 75].

More precisely, let S_0^x denote the central spin operator and let $\mathcal{H}$ be a Hamiltonian describing

nearest-neighbor interactions inside the cluster, $\mathcal{H}_{\rm cl}$, as well as the action of an effective field $\phi_{\rm eff}$ at the boundary spins,

$$\mathcal{H} = \mathcal{H}_{\rm cal} + J\,\phi_{\rm eff} \sum_{i\in\partial\Omega} S_i^x, \tag{4.63}$$

where $\partial\Omega$ denotes the cluster boundary. The expectation value of the central spin is given by

$$\langle S_0^x \rangle = \frac{\mathrm{Tr}\left[S_0^x\, e^{-\beta\mathcal{H}}\right]}{\mathrm{Tr}\left[e^{-\beta\mathcal{H}}\right]}, \tag{4.64}$$

where the trace is carried over all allowed spin configurations. Expanding the exponentials in Eq. (4.63) to the lowest nontrivial order in the effective field, we find that

$$\langle S_0^x \rangle = \langle S_0^x \rangle_{\rm cl} - \beta\, J\, \phi_{\rm eff} \sum_{i\in\partial\Omega} \langle S_0^x\, S_i^i \rangle_{\rm cl}, \tag{4.65}$$

where $\langle \cdots \rangle_{\rm cl}$ denotes the expectation value taken with just the Hamiltonian $\mathcal{H}_{\rm cl}$ and neglecting the boundary field. Setting $\langle S_0^x \rangle$ equal to $\phi_{\rm eff}$, we arrive at the equation

$$1 - \beta_c\, J \sum_{i\in\partial\Omega} \langle S_0^x\, S_i^x \rangle_{\rm cl} = 0, \tag{4.66}$$

which can be solved numerically to yield the critical inverse temperature $\beta = \beta_c$ as a function of J. The most costly part of the procedure is the calculation of the correlation function $\langle S_0^x S_i^x \rangle_{\rm cl}$, which requires an exhaustive enumeration of all spin configurations within the cluster.

We employed this method to compute the critical value of β for surface codes with clusters of increasing sizes and performed a finite-scaling analysis to estimate the critical value in the thermodynamic limit. The result is shown in Fig. 4.5. As in the case of the exact numerical calculations, we employed the constrained nearest-neighbor Ising model of Sec. 4.7 with J real and only allowed for spin configurations with positive plaquette eigenvalues. We find that $\beta_c J = 0.193(2)$ for an infinitely large system, which is about 60% higher than the estimate presented in Sec. 4.9

(given the roughness of the approximations involved in the estimate, the discrepancy seems quite acceptable). The extrapolated value also matches quite closely the point where the downturn of the fidelity develops (see Figs. 4.3 and 4.4), providing additional support for the existence of a phase transition in the thermodynamic limit in the case of nearest-neighbor interactions.

4.11 Discussion and conclusions

We have presented a fully quantum mechanical calculation of the fidelity of the surface code in the presence of a bosonic bath. We considered the fidelity after a complete quantum error correction cycle and in the most benign case, when a nonerror syndrome occurs. An important assumption made in the calculation was the resetting of the bath to its ground state after the syndrome extraction. We then expressed the fidelity as a function of the ratio of two complex amplitudes which were formulated as expectation values of a statistical spin model with complex two-body interactions and a restricted configuration space. We presented both analytical estimates and numerical evidence that the statistical spin model sustains an ordered/disordered phase transition in the limit of an infinite number of qubits. The existence of such a phase transition can be directly related to the existence of a threshold on resilience of the surface code: provided that the bath coupling constant remains lower than a critical value, fidelity can be maintained close to unity with increasing system size. This is very good news for those interested in large-scale implementations of the surface code.

This work provides more detailed derivations and deeper analyses than Ref. [66], in additional to new numerical support to the existence of an error threshold in the surface code in the presence of correlated noise. We note that our approach differs substantially from the surface code literature since we do not rely on a stochastic error model.

In order to understand the difference between a threshold due to correlations and the usual stochastic model discussion, let us consider the case of $D = 2$ and $s = 0$ (ohmic bath). As shown in Sec. 4.8, the probability of such a bosonic bath to produce a bit flip error is $p = \frac{1}{2}\left[1 - (2v\Delta\Lambda)^{-\beta/2}\right]$. If we take the ultraviolet cutoff to infinity, then we are bound to find $p = 1/2$. However, in most physics systems, and condensed matter systems in particular, the cutoff is finite. Hence, we can expand p for small β and Δ to obtain

$$\beta \approx \frac{4p}{\ln|2v\Delta\Lambda|}. \tag{4.67}$$

For the ohmic model, we also found that the real part of the effective interaction is given by [see Eq. (5.11)]

$$J_{ij} \approx \frac{1}{2}\ln\left(\frac{v\Delta}{|\mathbf{r}_i - \mathbf{r}_j|}\right) \tag{4.68}$$

for qubits within the causality cone. In both equations, the logarithms are slow growing functions and should be regarded as producing numbers of the same order. Therefore, we can rewrite p as

$$\beta \approx \frac{2p}{J}, \tag{4.69}$$

where we took $J \sim J_{ij} \sim (1/2)\ln|2v\Delta\Lambda|$. Now, we have also found that the inverse critical temperature is [see Eq. (4.62)]

$$\beta_c \approx \frac{\ln\mu}{2nJ}, \tag{4.70}$$

To be resilient to correlated errors, we must require the system to be above the critical temperature, thus $\beta < \beta_c$. Using the equations above, we find that

$$p < \frac{\ln\mu}{4n}. \tag{4.71}$$

For the least correlated case, where only nearest neighbors effective interactions take place, we

have

$$p < \frac{\ln \mu}{16} \sim 6\%. \tag{4.72}$$

That is, the threshold for the surface code in the presence of an ohmic bath is reduced to at most $p_c \sim 6\%$ due to the introduction of nearest-neighbors correlated errors. If we allow for longer-range correlated errors, the threshold will steadily decline.

Within our formulation, exact analytical calculations of the threshold based on the fidelity are daunting. Thus, it is likely that quantitative results will always require numerical simulations. In Ch. 5 we simulated statistical spin models with more general interactions than the nearest-neighbor case investigated here. Further investigations are necessary to relax the assumption of bath resetting and to evaluate the effects of residual qubit correlations on the fidelity over multiple cycles. Such studies are also under way in Mucciolo's group.

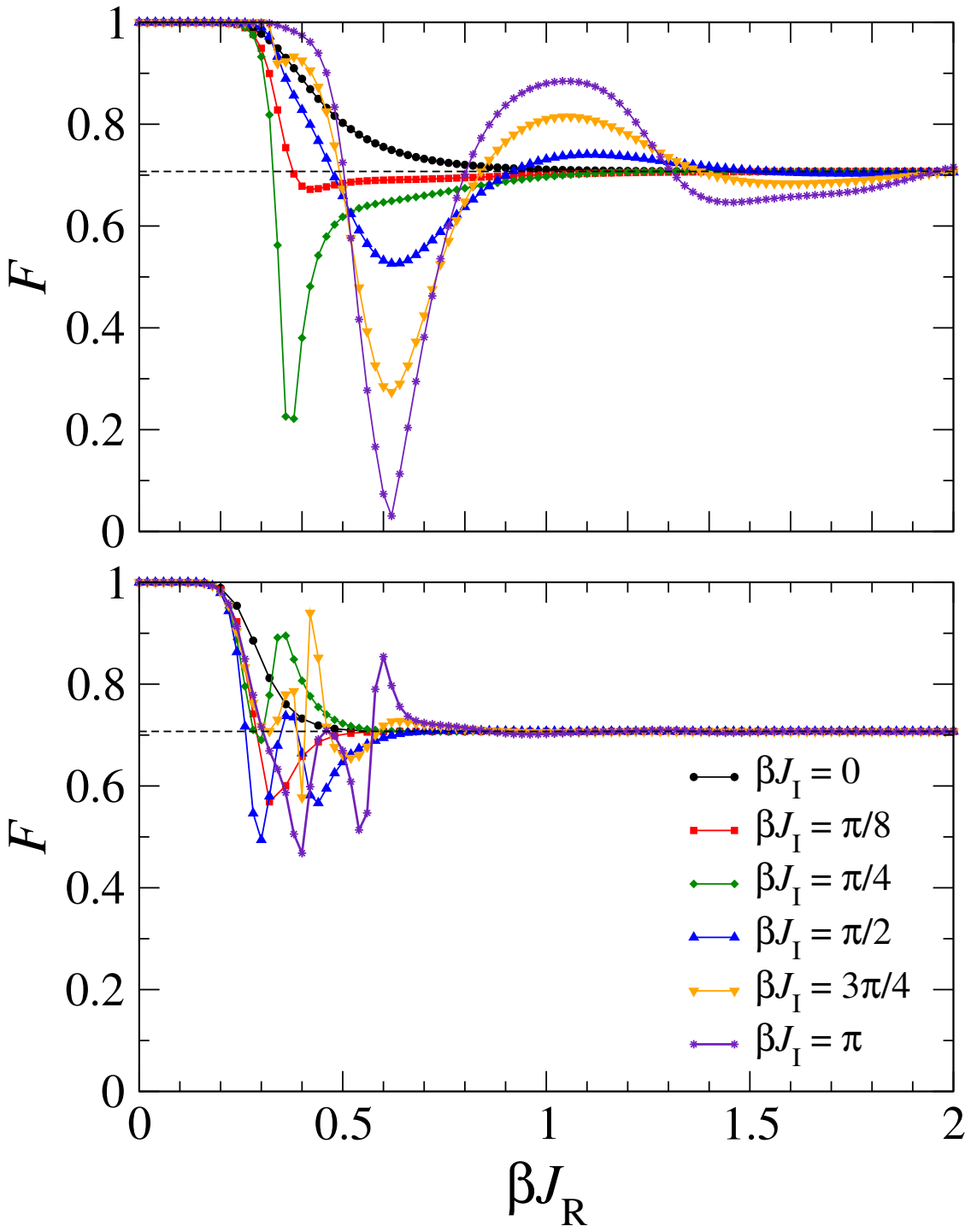

Figure 4.4: Fidelity of a code space of 25 physical qubits in contact with a bosonic bath when star operators are restricted to positive values ($A_\diamond = 1$) and an imaginary part is added to the coupling constant: $J = J_R + iJ_I$. The data sets correspond to different values of J_I.

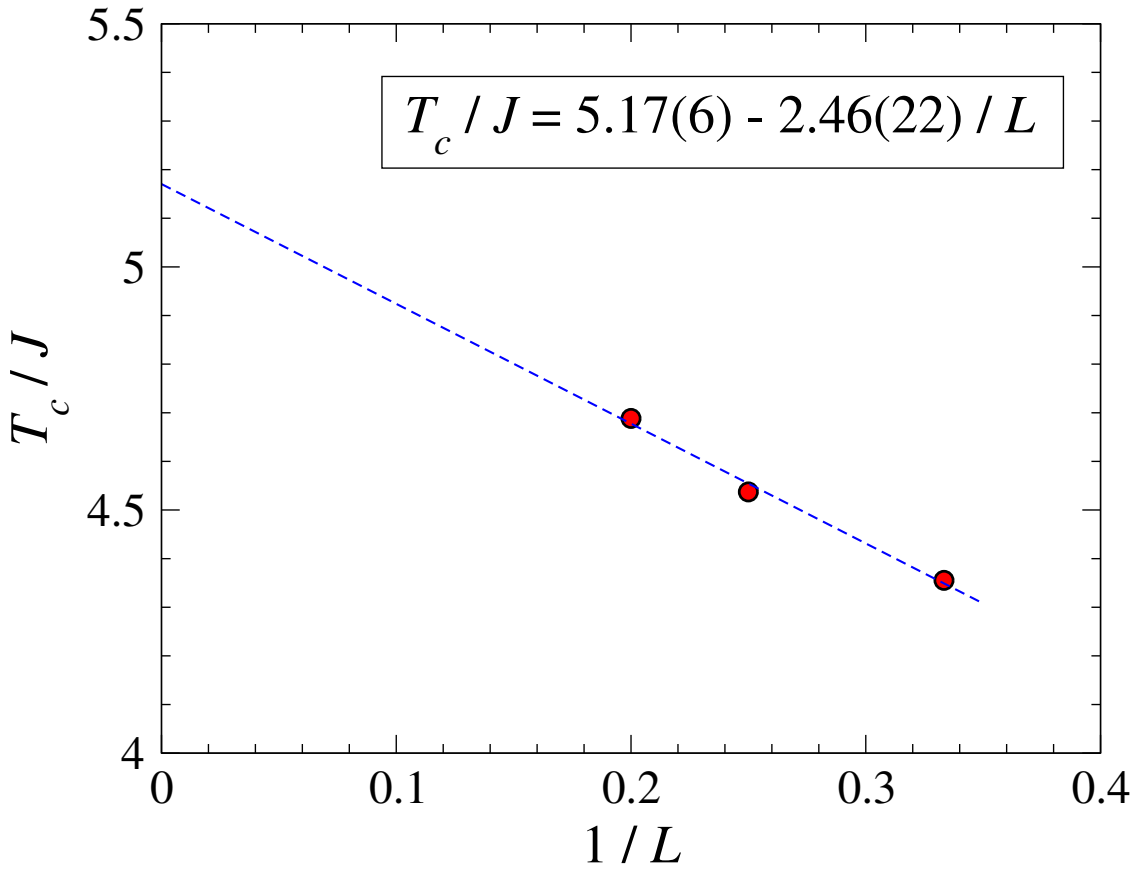

Figure 4.5: Finite-size scaling of the critical fictitious temperature T_c obtained from cluster mean-field calculations for lattice of sizes 13, 25, and 41. A real Ising interaction of strength J involving only nearest neighbors was used. The circles are the numerical data and the dashed line is a linear fit. L denotes the linear size of the surface code.

CHAPTER 5: NUMERICAL EVALUATION OF THE FIDELITY ERROR THRESHOLD FOR THE SURFACE CODE

- Pejman Jouzdani and Eduardo R. Mucciolo, "Numerical evaluation of the fidelity error threshold for the surface code", Phys. Rev. A **90**, 012315 (2014).

5.1 Abstract

We study how the resilience of the surface code is affected by the coupling to a non-Markovian environment at zero temperature. The qubits in the surface code experience an effective dynamics due to the coupling to the environment that induces correlations among them. The range of the effective induced qubit-qubit interaction depends on parameters related to the environment and the duration of the quantum error correction cycle. We show numerically that different interaction ranges set different intrinsic bounds on the fidelity of the code. These bounds are unrelated to the error thresholds based on stochastic error models. We introduce a definition of stabilizers based on logical operators that allows us to efficiently implement a Metropolis algorithm to determine upper bounds to the fidelity error threshold.

5.2 Introduction

Topological quantum codes provide an alternative route to fault-tolerance quantum computation. In topological quantum codes the information is encoded on the topological characteristics of the physical system, resulting in protection against local perturbations [25, 23, 81, 26]. The surface (or planar) code [24, 51] is an important example of this class of quantum codes that requires an

active approach to error correction on lattice of regular qubits. In contrast to the toric code [25], which has an intrinsic Hamiltonian that governs the evolution of the system, the surface code has no intrinsic Hamiltonian and the system's evolution is due to its coupling to an environment and the syndrome extraction and recovery operations at the end of a cycle. It has attracted increasing attention in recent years due to its more practical nature than other topological forms of encodings. Architectures based on superconducting qubits [82] and Majorana fermions [83] have been proposed theoretically. At the experimental level, significant increase in coherence time and fidelity of logical gates in superconducting qubits has been recently reported [84, 85, 86], suggesting that these systems may provide a suitable experimental setting for implementing surface codes. Several studies have been done to determine the error threshold of two-dimensional topological codes [53, 87, 89, 88, 90, 91]. However, in these studies the role played by correlated errors was not fully investigated. However, it is crucial to study the impact of correlated errors on any scalable quantum code before attempting to quantify error thresholds based on quantum error correction (QEC) protocols [92].

When in contact with environmental degrees of freedom, the physical qubits in the surface code will experience an effective dynamics. This effective dynamics may comprise qubit-qubit interactions, which in turn can result in a correlated time evolution. Since a large-scale quantum code has a large Hilbert space, a correlated dynamics may cause a sharp change in the quantum phase of the code system, even in the presence of QEC operations. This change of phase cannot be studied in the context of stochastic noise models, which typically only include bit flip, phase flip, and depolarizing channels.

The effective dynamics induced by the environment on the code system is in general very nontrivial to derive from first principles. However, for a particular case, the bosonic bath, we were able to obtain an exact effective action after a single QEC cycle [66, 93]. This action comprises a qubit-qubit interaction term with a distance-dependent exchange coupling. The range and strength

of qubit-qubit interaction were found to be functions of environmental parameters, the distance between the qubits, and the duration of the QEC cycle. The effective dynamics derived for a bosonic bath could be used as a phenomenological model for other types of environments as it has a rather general functional form.

In this chapter we numerically evaluate the effect of correlated errors induced by a two-qubit effective action and study the impact of different ranges of correlations. We use a Monte Carlo method for evaluating the fidelity of the surface code at the end of a complete QEC cycle. We introduce an alternative approach to define the surface code stabilizers that helps us to implement an efficient Metropolis algorithm. This method can be extended to other topological systems such as the toric code. For the surface code, we confirm the results presented in Ref. [98], namely, the existence of a sharp transition in the fidelity as a function of the coupling between qubits and the environment for large enough codes. The critical value of this coupling provides a threshold for the ability of the surface code to protect quantum information. We also find that an increase in the correlation range does not washes away this critical point but moves it to lower coupling constant values, making it more difficult in practice to achieve protection.

The chapter is organized as follows. In Sec. 5.3 we introduced the basic elements of the surface code. In Sec. 5.4 we describe a model interaction for the environment and the physical qubits that induces an effective evolution for the code system. We then use this evolution in Sec. 5.5 to obtain an expression for the surface code fidelity in terms of expectation values of a spin statistical model. The numerical Monte Carlo method used to compute these expectation values and the results are described in Secs. 5.6 and 5.7. Finally, a summary is provided in Sec. 5.8.

5.3 Surface Code

The surface code [24, 51] is a collection of N qubits located on the links of a two-dimensional lattice, as shown in Fig. 5.1. There are two types of stabilizers, $\hat{A}_s$ and $\hat{B}_p$, which are defined as

$$\hat{A}_s = \prod_{i \in s} \sigma_i^x \tag{5.1}$$

and

$$\hat{B}_p = \prod_{i \in p} \sigma_i^z. \tag{5.2}$$

They have eigenvalues A_s and B_p, respectively, that take the values ± 1. The subscript $s(p)$ refers to a vertex (plaquette) on the lattice, and σ_i^α is the α component of the Pauli matrices that acts on the i-th qubit. The two stabilizers commute, $[\hat{A}_s, \hat{B}_p] = 0$, and thus are simultaneously observable. In addition, there are two logical operators defined as

$$\hat{X}_{l_x} = \prod_{i \in l_x} \sigma_i^x, \tag{5.3}$$

and

$$\hat{Z}_{l_z} = \prod_{i \in l_z} \sigma_i^z, \tag{5.4}$$

where the path l_x (l_z) runs from one boundary to the opposite boundary, as shown in the Fig. 5.1. The two logical operators follow the same commutation relations as the Pauli matrices σ^x and σ^z and both commute with the stabilizers in Eqs. (5.1) and (5.2).

The *code space* is defined as the particular subspace of the total Hilbert space of the system

for which the outcome of any stabilizer is $+1$. The maximum set of observables can be either $\{\{\hat{A}\},\{\hat{B}\},\hat{Z}\}$ or $\{\{\hat{A}\},\{\hat{B}\},\hat{X}\}$. Considering the set $\{\{\hat{A}\},\{\hat{B}\},\hat{Z}\}$, $\hat{X}$ anticommutes with the logical operator in the set, $\hat{Z}$. Therefore, there are only two distinct basis states $|SC\rangle$ and $\hat{X}|SC\rangle$ that satisfy the condition of the code space. $\hat{X}$ can be chosen along different paths l_x. However $\hat{X}|SC\rangle$ is unique and independent of the chosen logical operator. These two orthogonal states are the two states of the logical qubit of the surface code. The code is topologically protected, e.g., to flip the logical qubit state $|SC\rangle$ to $\hat{X}|SC\rangle$ a logical operator comprising at least L physical qubit operations must be applied, where L is the linear size of the system. We will refer to $|SC\rangle$ as the *code state*.

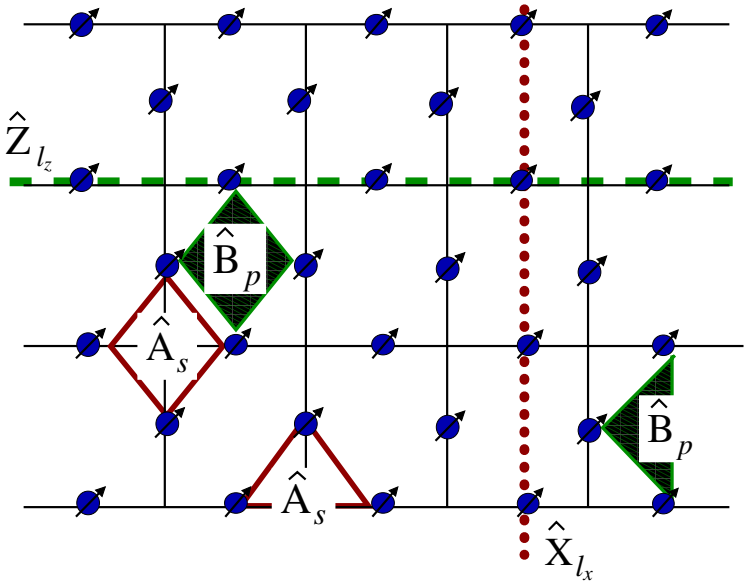

Figure 5.1: The geometry of the surface code system. Physical qubits are shown with arrows. A plaquette (star) operator $\hat{B}_p$ ($\hat{A}_s$) is shown with a shaded (unshaded) enclosed area connecting the corresponding qubits. The dashed green (dotted red) line l_z (l_x) represents the logical operator $\hat{Z}_{l_z}(\hat{X}_{l_x})$ and runs over corresponding qubits.

Any deviation from the code space due to local errors such as qubit flips or phase flips results in excitations known as anyons. The anyons correspond to stabilizers that yield an outcome -1 after measurement. Anyons corresponding to $\hat{A}$ stabilizers are referred as "e" type, while anyons

corresponding to $\hat{B}$ stabilizers are "m" type.

5.4 Interaction with the environment

When the system is in contact with a bath the total Hamiltonian is

$$H = H_B + V_{BC}, \tag{5.5}$$

where H_B is the bath Hamiltonian and V_{BC} is the interaction part. If the closed system is prepared in the product state $|SC\rangle \otimes |B\rangle$, where the $|B\rangle$ is the bath ground state, the closed system evolves in time as

$$|\psi(t)\rangle \;\; = \;\; U_I(t)\,|SC\rangle \otimes |B\rangle, \tag{5.6}$$

where $U_I(t)$ is the time evolution operator of the combined system in the interaction picture. At the end of the QEC cycle the state of the environment may have components beyond its ground state. As a result, the entanglement between the qubits and the environment can spill over to the next QEC cycle. While this effect deserves investigation, here we will adopt a simplifying hypothesis and assume that the environment remains in its ground state at the end of the QEC cycle. This could be achieved by maintaining the environment cold (i.e., by keeping it in contact with a much larger bath or reservoir). Hence, we define

$$U_{\text{eff}}(\Delta) = \langle B|\, U_I(\Delta)\,|B\rangle, \tag{5.7}$$

as the effective evolution operator of the code system at the end of a QEC cycle of duration Δ.

The evolution under $U_{\text{eff}}(\Delta)$ induces an effective dynamics into the code system that includes

dissipation and dephasing. In general, the functional form of $U_{\text{eff}}(\Delta)$ in terms of the qubit operators $\{\sigma_i^\alpha\}$ can be rather difficult to derive from first principles. For the particular case of a gapless bosonic environment with a coupling given by

$$V_{BC} = \lambda \sum_{r_i} f(r_i)\, \sigma_i^x, \tag{5.8}$$

a simple expression can be exactly derived. Here, λ is the strength of coupling to the bosonic field, $f(r_i)$ is the bosonic field operator of the bath, and σ_i^x is the Pauli matrix acting on the i-th qubit. In this case, the induced evolution operator dynamics was found to be [66, 93]

$$U_{\text{eff}}(\Delta) = e^{\beta H_{\text{eff}}} = e^{-\beta \sum_{ij} J_{ij} \sigma_i^x \sigma_j^x}. \tag{5.9}$$

The sum in the exponent is over the physical qubits of the surface code (see Fig. 5.2). The parameter β is a function of λ and other characteristics of the bosonic environment. For the Ohmic case [93],

$$\beta = \frac{1}{2\pi} \left(\frac{\lambda}{\omega_0} \right)^2, \tag{5.10}$$

with ω_0 denoting a characteristic frequency of the bosons and

$$J_{ij} = \frac{1}{2} \times \begin{cases} \text{arcosh}\left(\frac{v\Delta}{|\mathbf{r}_i - \mathbf{r}_j|} \right) + \frac{i\pi}{2}, & \frac{|\mathbf{r}_i - \mathbf{r}_j|}{v\Delta} < 1, \\ i \arcsin\left(\frac{v\Delta}{|\mathbf{r}_i - \mathbf{r}_j|} \right), & \frac{|\mathbf{r}_i - \mathbf{r}_j|}{v\Delta} > 1. \end{cases} \tag{5.11}$$

Here v is the bosonic mode velocity. The complex interaction J_{ij} is directly related to the correlation function of the bath at two spacial points $\mathbf{r}_i$ and $\mathbf{r}_j$ and to Δ. Notice that Eq. (5.11) was derived in Ref. [93] under the assumption that the bath returns to its ground state at the end of the QEC cycle, as shown in Eq. (5.7).

The functional form in the effective action in Eq. (6.21) can also be used as a phenomenological

error model of correlated errors with a complex exchange coupling parameter J_{ij}. We note that other forms of interaction between the surface code constituents and the environment have been used in the literature. In particular, one may start with an interaction such as $V_{BC} \sim \lambda \sum_{r_i} f(r_i)\, A_i$ where a bosonic field couples to the stabilizers. In this case, the resulting effective dynamics may enhance the surface code protection [94, 95].

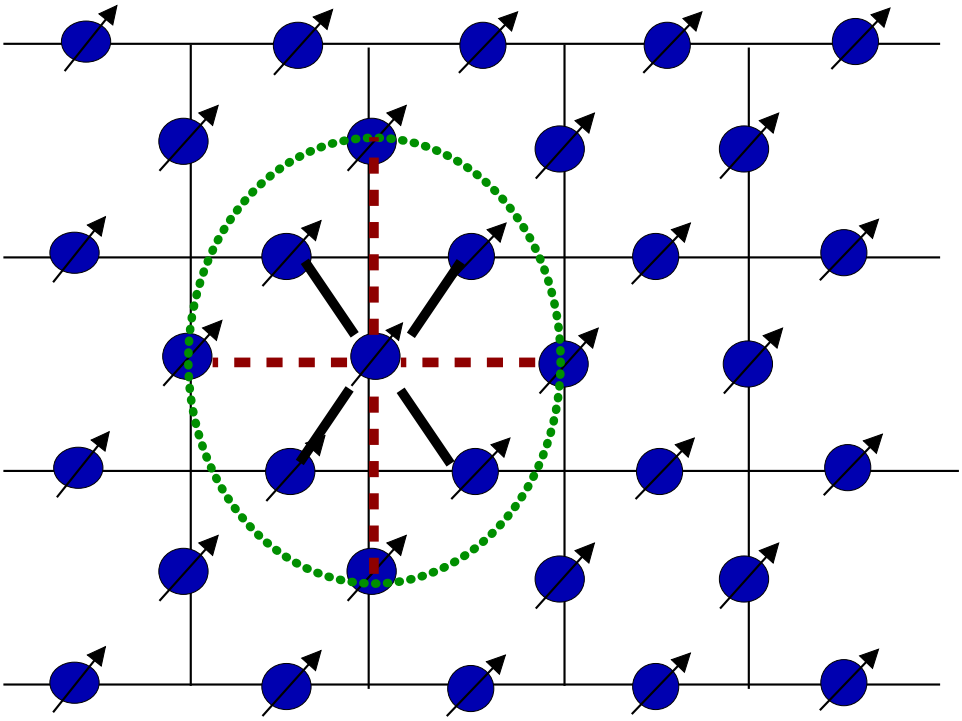

Figure 5.2: The effective interaction induced by the bath, Eq. (6.21), between a qubit and its nearest (solid black lines) and next-to-nearest neighbors (dashed red lines). The range of the interaction (dotted circle) is related to the QEC period Δ.

5.5 QEC with flawless recovery

The system is maintained in its code space by means of QEC cycles. At each QEC cycle the stabilizers are measured (syndrome detection) and a suitable recovery operation is performed with the goal of returning the system to its *code state*, as defined in Sec. 5.3. Due to the interaction with

the environment, prior to the syndrome detection the code system is in a superposition state where all syndromes are possible. After reading the stabilizers, the system is detected (i.e. projected) onto a particular superposition state (syndrome). Eventually, a non-destructive recovery returns the system back to the code state, $|SC\rangle$, or erroneously to $\hat{X}\,|SC\rangle$.

The syndromes in the QEC protocol are based on measurements of the stabilizers. Let us define $\mathcal{P}_{n,f} = |n, f\rangle\langle n, f|$ as the projection onto a subspace of n excitations or anyons. The n excitations may be detected at different vertices or plaquettes on the surface code. The index f refers to the configuration where anyons are detected on the surface code after syndrome detection. Due to the topological nature of the code, any state $|n, f\rangle$ is *a superposition of a large number of states* involving the physical qubits of the system,

$$|n, f\rangle = \sum_{s^*} |s^*\rangle, \tag{5.12}$$

where the sum is over configurations of the physical qubits $|s^*\rangle = |s_1, \ldots, s_N\rangle$ and the asterisk indicates that the sum is taken over the configurations that are consistent with the condition of "n anyons with the configuration f".

After being initially set in the code state $|SC\rangle$, the system interacts with the environment. After a time interval Δ, it evolves to the state $U_{\text{eff}}(\Delta)\,|SC\rangle$. The effective time evolution operator $U_{\text{eff}}(\Delta)$ is in general nontrivial and may not be unitary. At this point we assume that the QEC operation detects the system (with some probability) to be in the state $|n, f\rangle$. Then, a flawless recovery operation $\mathcal{R}$ returns this state to either $|SC\rangle$ or, erroneously, to $\hat{X}|SC\rangle$, namely,

$$\mathcal{R}\,\mathcal{P}_{n,f}\,U_{\text{eff}}(\Delta)\,|SC\rangle = \mathcal{A}\,|SC\rangle + \mathcal{B}\,\hat{X}\,|SC\rangle, \tag{5.13}$$

where $\mathcal{A}$ and $\mathcal{B}$ are the amplitudes of the two orthogonal states $|SC\rangle$ and $\hat{X}|SC\rangle$, respectively.

To be more explicit, let us exactly specify the projector $\mathcal{P}_{n,f} = |n,f\rangle\langle n,f|$ for the case where errors are of "m" type. "m" type errors occur as a result of bit flipping qubits along a set of strings. We define this string operation as

$$\hat{S}^x(\mathcal{L}) = \prod_{j\in\mathcal{L}} \sigma_j^x, \tag{5.14}$$

where $\mathcal{L}$ is a set of strings running on the surface code lattice such that $|n,f\rangle = \hat{S}^x(\mathcal{L})|SC\rangle$. There are many possible sets of $\mathcal{L}$ and corresponding $\hat{S}^x(\mathcal{L})$ that generate the same state $|n,f\rangle$. Two such choices of string operators, $\hat{S}^x(\mathcal{L}_1)$ and $\hat{S}^x(\mathcal{L}_2)$, can differ from each other in two possible ways: Either

$$\begin{aligned} \hat{S}^x(\mathcal{L}_1)|SC\rangle &= \left[\prod_{s\in\mathcal{P}} \hat{A}_s\right] \hat{S}^x(\mathcal{L}_2)\,|SC\rangle \\ &= \hat{S}^x(\mathcal{L}_2)\,|SC\rangle, \end{aligned} \tag{5.15}$$

or

$$\begin{aligned} \hat{S}^x(\mathcal{L}_1)|SC\rangle &= \left[\prod_{s\in\mathcal{P}} \hat{A}_s\,\hat{X}\right] \hat{S}^x(\mathcal{L}_2)\,|SC\rangle \\ &= \hat{X}'\hat{S}^x(\mathcal{L}_2)\,|SC\rangle. \end{aligned} \tag{5.16}$$

Here, $\mathcal{P}$ is a set of vertices on the surface code. In Eqs. (5.15) and (5.16) we used the identity $\left[\prod_{s\in\mathcal{P}} \hat{A}_s\right]\,|SC\rangle = |SC\rangle$. Thus, the two states $S^x(\mathcal{L})\,|SC\rangle$ and $\hat{X}S^x(\mathcal{L})\,|SC\rangle$ alone are enough to define $\mathcal{P}_{n,f}$ as

$$\begin{aligned} \mathcal{P}_{n,f} &= \hat{S}^x(\mathcal{L})\,|SC\rangle\langle SC|\,\hat{S}^x(\mathcal{L}) \\ &\quad + \hat{X}\hat{S}^x(\mathcal{L})\,|SC\rangle\langle SC|\,\hat{S}^x(\mathcal{L})\hat{X}. \end{aligned} \tag{5.17}$$

With this definition we find the state of the code at the end of the first QEC cycle to be

$$\begin{aligned} |SC(\Delta)\rangle &= \mathcal{R}\mathcal{P}_{n,f}\, U_{\text{eff}}(\Delta)\, |SC\rangle \\ &\quad + \mathcal{R}\hat{S}^x(\mathcal{L})\, |SC\rangle\ \langle SC|\hat{S}^x(\mathcal{L})\, U_{\text{eff}}(\Delta)|SC\rangle \\ &\quad + \mathcal{R}\,\hat{X}\,\hat{S}^x(\mathcal{L})\, |SC\rangle\ \langle SC|\hat{S}^x(\mathcal{L})\,\hat{X} U_{\text{eff}}(\Delta)\, |SC\rangle \\ &= \mathcal{A}_{n,p}\, |SC\rangle + \mathcal{B}_{n,p}\hat{X}\, |SC\rangle, \end{aligned} \tag{5.18}$$

where we assume a flawless recovery, $\mathcal{R}\,\hat{S}^x(\mathcal{L}) = \mathbf{1}$, and define the amplitudes

$$\mathcal{A}_{n,f} = \langle SC|\hat{S}^x(\mathcal{L})\, U_{\text{eff}}(\Delta)\, |SC\rangle \tag{5.19}$$

and

$$\begin{aligned} \mathcal{B}_{n,f} &= \langle SC|\hat{S}^x(\mathcal{L})\,\hat{X}\, U_{\text{eff}}(\Delta)\, |SC\rangle \\ &= \langle SC|\hat{S}^x(\bar{\mathcal{L}})\, U_{\text{eff}}(\Delta)\, |SC\rangle. \end{aligned} \tag{5.20}$$

The fidelity is a suitable quantity to measure the success of the QEC operation after error correction,

$$\mathcal{F} = \frac{\langle SC|SC(\Delta)\rangle}{\sqrt{\langle SC(\Delta)|SC(\Delta)\rangle}} \tag{5.21}$$

It is straightforward to show that the fidelity can be written in terms of the amplitudes $\mathcal{A}_{n,f}$ and $\mathcal{B}_{n,f}$, namely,

$$\mathcal{F} = \frac{1}{\sqrt{1 + \left|\frac{\mathcal{B}_{n,f}}{\mathcal{A}_{n,f}}\right|^2}}. \tag{5.22}$$

In order to find a suitable expression for the numerical evaluation of the amplitudes $\mathcal{A}_{n,f}$ and $\mathcal{B}_{n,f}$,

we write $|SC\rangle$ as

$$|SC\rangle = \frac{1}{\sqrt{2^{N_\diamond}}} \prod_s (1 + \hat{A}_s) |F_z\rangle, \tag{5.23}$$

where $|F_z\rangle$ is the ferromagnet state of the qubits in the z-direction: $|F_z\rangle = |\uparrow\rangle_1 \ldots |\uparrow\rangle_N$, with $N_\diamond$ being number of star operators. Noting that

$$|F_z\rangle = \prod_{i=1}^{N} \frac{|+\rangle_i + |-\rangle_i}{\sqrt{2}}, \tag{5.24}$$

where $\sigma_i^x |\pm\rangle_i = \pm 1 |\pm\rangle_i$ and $|\pm\rangle_i$ stands for eigenvectors of Pauli matrix σ_i^x acting on i-th physical qubit, we obtain

$$|SC\rangle = \frac{1}{\sqrt{2^{N_\diamond - 1}}} \sum_{s^*} |s^*\rangle. \tag{5.25}$$

The sum in Eq. (5.25) runs over restricted states s^* (a product state of $|\pm\rangle_i$ of physical qubits) that preserve the conditions $A_s = 1$ (i.e., $\hat{A}_s|s^*\rangle = +|s^*\rangle$) for all vertices s of the lattice. The state $|SC\rangle$ also satisfies the conditions $\hat{Z}|SC\rangle = +|SC\rangle$ and $B_p = 1$ ($\hat{B}_p|SC\rangle = +|SC\rangle$) for all plaquettes of the lattice. Hereafter we will make use of the relations

$$\hat{S}^x(\mathcal{L})|s^*\rangle = S_{s^\star}(\mathcal{L}) |s^*\rangle \tag{5.26}$$

and

$$\hat{S}^x(\mathcal{L})\hat{X}|s^*\rangle = S_{s^\star}(\bar{\mathcal{L}}) |s^*\rangle, \tag{5.27}$$

with $S_{s^\star} = \pm 1$ being the product of the σ_i^x operators along either the path $\mathcal{L}$ or $\bar{\mathcal{L}}$. By inserting Eqs. (5.25), (5.26), and (5.27) into Eqs. (5.19) and (5.20), we arrive at

$$\mathcal{B} = \frac{\mathcal{B}_{n,f}}{\mathcal{A}_{0,0}} = \frac{\sum_{s^*} S_{s^\star}(\bar{\mathcal{L}})\, U_{\text{eff}}(s^\star)}{\sum_{s^*} U_{\text{eff}}(s^\star)}, \tag{5.28}$$

and

$$\mathcal{A} = \frac{\mathcal{A}_{n,f}}{\mathcal{A}_{0,0}} \quad = \quad \frac{\sum_{s^*} S_{s^\star}(\mathcal{L})\, U_{\text{eff}}(s^\star)}{\sum_{s^*} U_{\text{eff}}(s^\star)}. \tag{5.29}$$

Here $U_{\text{eff}}(s^\star)$ is the matrix element $\langle s^\star | U_{\text{eff}}(\Delta) | s^\star \rangle$ that can be considered as a statistical weight in the sums shown above.

Equations (5.28) and (5.29) show that the calculation of $\mathcal{A}_{n,f}$ and $\mathcal{B}_{n,f}$ maps onto a *statistical mechanics* problem where these amplitudes are equal to the expectation values $\langle S(\mathcal{L}) \rangle$ and $\langle S(\bar{\mathcal{L}}) \rangle$, respectively. The averaging $\langle \dots \rangle$ is performed with respect to a complex-time effective action H_{eff} that gives rise to the statistical weight $U_{\text{eff}}(s^*)$ introduced above. In the following, we study the fidelity of the code based on the behavior of the amplitudes $\mathcal{B}$ and $\mathcal{A}$ for an effective action comprising qubit-qubit interactions of the form introduced in Eq. (6.21). We limit our study to real values of β and J_{ij} while probing different ranges of interactions, namely nearest neighbors and next-to-nearest neighbors. We remark that the range of the effective qubit-qubit interaction can be sharply controlled by the duration of the QEC cycle: longer cycles lead to longer ranges while shorter cycles decrease the range, even down to nearest neighbors.

5.6 Numerical Method

We numerically evaluate the amplitudes $\mathcal{A}$ and $\mathcal{B}$, as defined in Eqs. (5.28) and (5.29), using a classical Monte Carlo method and assuming an effective evolution operator as in Eq. (6.21), with an effective action of the form

$$H_{\text{eff}} = -\sum_{(ij)} J(|r_i - r_j|)\, \sigma_i^x \sigma_j^x \tag{5.30}$$

for nearest-neighbor and beyond nearest-neighbor interactions.

Using the standard classical Monte Carlo method [96], we replace the summation over the large set of configurations $\{s^*\}$ in Eqs. (5.28) and (5.29), which is of order $[O(2^{\frac{N}{2}})]$, by a sum over a smaller set of representative sample configurations $\{\tau\}$ for a given value of βJ. All the sampled configurations have the same statistical weight $e^{-\beta E_\tau}$. If there are M representative configurations for a given βJ, we then have

$$\sum_{s^*} \{...\}\, e^{-\beta E_{s^*}} \rightarrow \frac{1}{M} \sum_{\tau} \{...\}, \tag{5.31}$$

where we target the average value of the quantity $\{...\}$. We use a Metropolis algorithm to collect these relevant configurations assuming that βJ is real. However, since we must take into account the constraint $A_s = 1$ for any vertex s, the standard Metropolis algorithm needs to be suitably modified.

In general, a state $|s^*\rangle$ that satisfies the constraint "$A_s = 1$ for all s" in Eq. (5.25) has the form

$$|s^*\rangle = \begin{cases} \prod_{p\in\mathcal{P}} \hat{B}_p\, |F_x\rangle, & \text{(I)} \\ \text{or} & \\ \prod_{p\in\mathcal{P}} \hat{B}_p\, \hat{Z}\, |F_x\rangle. & \text{(II)} \end{cases} \tag{5.32}$$

Here, $\mathcal{P}$ is an arbitrary set of plaquettes. States in the first class, (I), are eigenstates of $\hat{X}$ with eigenvalue $+1$, while in the second class, (II), the states are eigenstates of $\hat{X}$ with eigenvalue -1. Equation (5.32) provides a natural codification of the restricted states $|s^*\rangle$: One can start with a *vacuum state* $|F_x\rangle$, then flip a number of qubits by $\prod_{p\in\mathcal{P}} \hat{B}_p$ that correspond to $\mathcal{P}$, and arrive at a restricted state $|s^*\rangle$. However, this is not the route we pursue. Below we present an equivalent but alternative definition for the stabilizers of the surface code and consequently of the

states in Eq. (5.32). They provide a more efficient implementation of the Metropolis algorithm. The new definition for stabilizers is not limited to the surface code and can be extended to higher-dimensional codes.

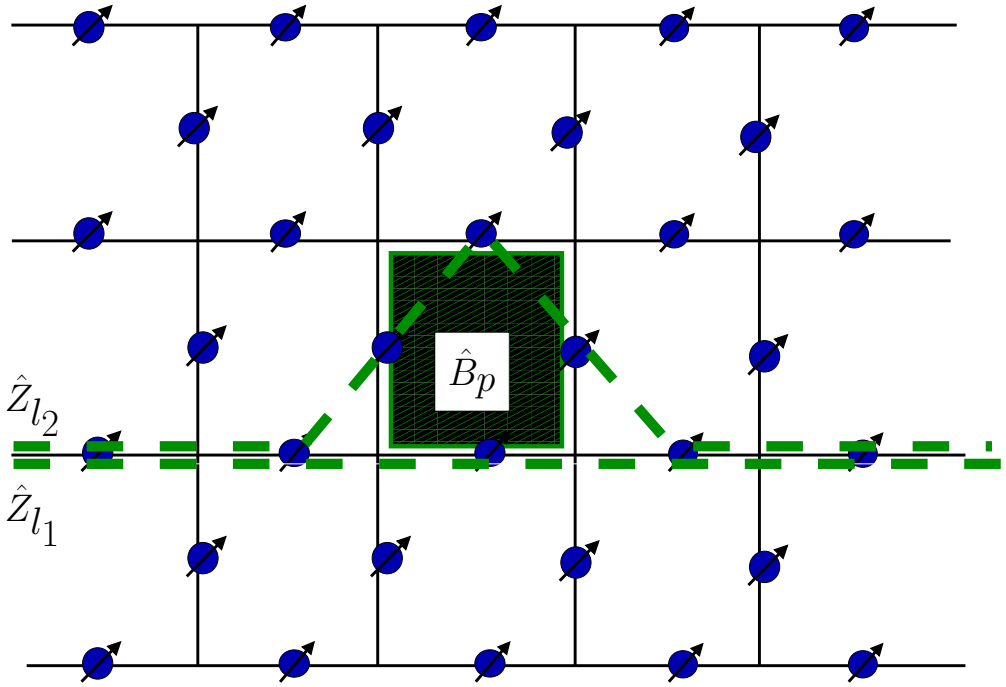

Figure 5.3: Applying two logical $\hat{Z}$ operators along the paths l_1 and l_2 is equivalent to a $\hat{B}_p$ operator shown with the hatched rectangle.

Since $\sigma_i^\alpha \sigma_i^\alpha = 1$ for $\alpha = x, y, z$, one can write the stabilizers of Eqs. (5.1) and (5.2) as

$$\hat{A}_s = \prod_{i \in s} \sigma_i^x = \hat{X}_{l_1} \hat{X}_{l_2} \dots \hat{X}_{l_{2m}} \tag{5.33}$$

and

$$\hat{B}_p = \prod_{i \in p} \sigma_i^z = \hat{Z}_{l_1} \hat{Z}_{l_2} \dots \hat{Z}_{l_{2m}}, \tag{5.34}$$

where a path l_i goes from one boundary to the opposite boundary of the system. The set $\{l_i\}$ is

chosen such that the product of the logical operators $\hat{X}_{l_1}\hat{X}_{l_2}\ldots\hat{X}_{l_{2m}}$ (or $\hat{Z}_{l_1}\hat{Z}_{l_2}\ldots\hat{Z}_{l_{2m}}$) is equal to $\prod_{i\in s}\sigma_i^x$ (or $\prod_{i\in p}\sigma_i^z$) and thus the stabilizer $\hat{A}_s$ (or $\hat{B}_p$). The number of paths, $2m$, is not unique. An even number guarantees that the commutation relation $[\hat{A}_s,\hat{B}_p]=0$ is satisfied. The product of $2m$ logical operators always forms closed loops. For example, in Fig. 5.3 the operation of the stabilizer operator $\hat{B}_p$ on the qubits of plaquette p is generated by applying two logical $\hat{Z}$ operators along the paths l_1 and l_2, as depicted in the figure.

Thus, the states $|s^*\rangle$ defined in Eq. (5.32) can be stated in terms of logical operations as

$$|s^*\rangle = \begin{cases} \hat{Z}_{l_1}\hat{Z}_{l_2}\ldots\hat{Z}_{l_{2m}}\,|F_x\rangle = \mathbf{Z}_l^2\,|F_x\rangle, & \text{(I)} \\ \text{or} & \\ \hat{Z}_{l_1}\hat{Z}_{l_2}\ldots\hat{Z}_{l_{2m}}\hat{Z}|F_x\rangle = \mathbf{Z}_l|F_x\rangle, & \text{(II)} \end{cases} \tag{5.35}$$

where we abbreviate the product $\hat{Z}_{l_1}\hat{Z}_{l_2}\ldots\hat{Z}_{l_{2m}}$ as $\mathbf{Z}_l^2$ and $\hat{Z}_{l_1}\hat{Z}_{l_2}\ldots\hat{Z}_{l_{2m}}\hat{Z}$ as $\mathbf{Z}_l$. By introducing these definitions into Eqs. (5.28) and (5.29) and using the fact that $\mathbf{Z}_l^2\,\hat{X} = \hat{X}\,\mathbf{Z}_l^2$ and $\mathbf{Z}_l\,\hat{X} = -\,\hat{X}\,\mathbf{Z}_l$, we arrive at

$$\begin{aligned} \mathcal{B} \;=\; & \sum_l \{\langle F_x|\,\mathbf{Z}_l^2\,S^x(\mathcal{L})\,U_{\text{eff}}\,\mathbf{Z}_l^2|F_x\rangle \\ & -\langle F_x|\,\mathbf{Z}_l\,S^x(\mathcal{L})\,U_{\text{eff}}\,\mathbf{Z}_l|F_x\rangle\} \end{aligned} \tag{5.36}$$

and

$$\begin{aligned} \mathcal{A} \;=\; & \sum_l \{\langle F_x|\,\mathbf{Z}_l^2\,S^x(\mathcal{L})\,U_{\text{eff}}\,\mathbf{Z}_l^2|F_x\rangle \\ & +\langle F_x|\,\mathbf{Z}_l\,S^x(\mathcal{L})\,U_{\text{eff}}\,\mathbf{Z}_l|F_x\rangle\}, \end{aligned} \tag{5.37}$$

up to a common normalization factor.

To understand the essential difference between $\mathcal{A}$ and $\mathcal{B}$, let us assume a phase of the system in which the states belonging to the two classes of Eq. (5.35) contribute with the same statistical weight U_{eff} (the topological state). In this phase any fluctuation around the equilibrium configuration states, $\{|s^{\star}\rangle\}$ (which is of the order of $\mathcal{L}$ and less than the distance of the code $\frac{L}{2}$), will be canceled out in the sum in the expression for $\mathcal{B}$ via the minus sign of the second term in Eq. (5.36). Hence, the ratio $\left|\frac{\mathcal{B}}{\mathcal{A}}\right| \to 0$ in thermodynamic limit and the fidelity $\mathcal{F} \to 1$, as expected. However, in the phase where the statistical weight of the states in class I differs from states in class II in Eq. (5.35), i.e., in the ordered phase, there is a sizable change in $\left|\frac{\mathcal{B}}{\mathcal{A}}\right|$. In our model the ordered phase corresponds to the state $|F_x\rangle$. In this limit, $\left|\frac{\mathcal{B}}{\mathcal{A}}\right| \to 1$ and a sharp phase transition takes place between these two limits. Thus, for a correct decoding and sufficiently large system, one should expect to see $|\mathcal{B}| < |\mathcal{A}|$ in the disordered phase (topological phase) in a universal way, independently of the error $S_{s^{\star}}(\mathcal{L})$, as long as $\mathcal{L} < \frac{L}{2}$.

Equation (5.35) provides a novel way for the codification of the restricted state $|s^{*}\rangle$: One begins with a *vacuum state* $|F_x\rangle$, then flips a number of qubits along certain path $\{l \equiv l_1 \dots\}$, and arrives at a restricted state $\mathbf{Z}_l^2 |F_x\rangle$ or $\mathbf{Z}_l |F_x\rangle$. The sums in Eqs. (5.36) and (5.37) run over all possible paths $\{l\}$. The statistical weight U_{eff} corresponds to the probability of flipping the qubits along the path l. In this regard, the Metropolis algorithm finds the most relevant paths. The scheme to update the configurations is then similar to the techniques used in world-line-based quantum Monte Carlo [97], since each two $\mathbf{Z}_l$ and $\mathbf{Z}_{l'}$ differ by a certain number of $\hat{B}_p$ operations.

5.7 Numerical Results

Considering a real homogeneous interaction coupling $J_{ij} = J(|r_i - r_j|)$, we use the method described in Sec. 5.6 to numerically evaluate $\mathcal{A}$, $\mathcal{B}$, and $\left|\frac{\mathcal{B}}{\mathcal{A}}\right|$ to determine the fidelity $\mathcal{F}$.

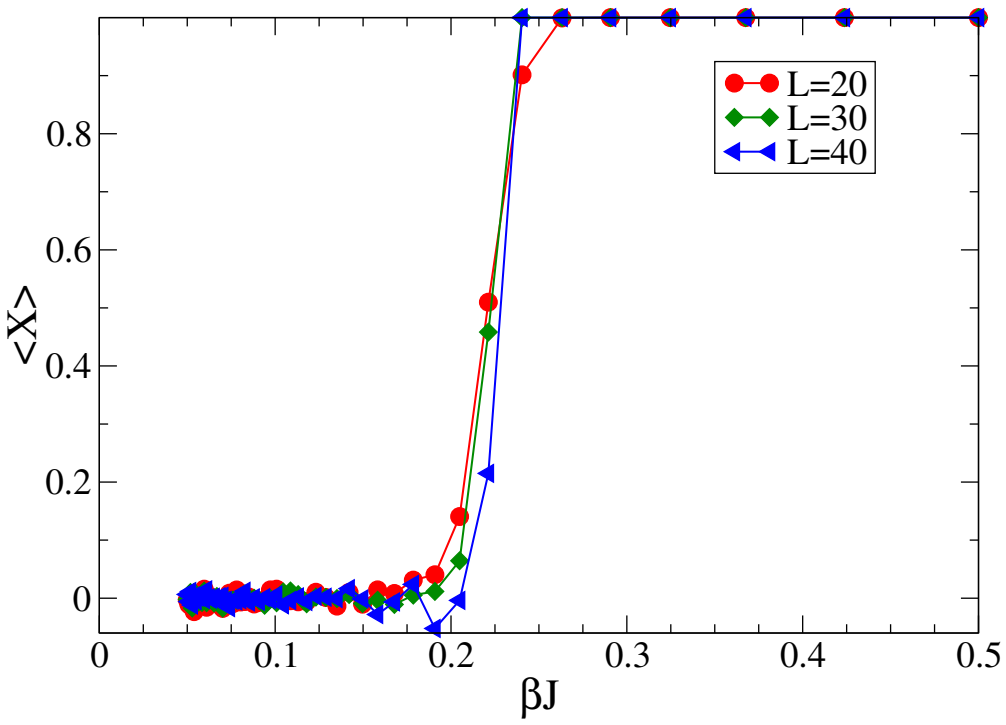

Figure 5.4: The numerical evaluation of $\langle X\rangle = \left|\frac{\mathcal{B}}{\mathcal{A}}\right|$ for non-error syndromes based on the Monte Carlo calculation for different system sizes. $L = 20$ is a surface code system with 761 qubits (circle), $L = 30$ has 1741 qubits (diamond), and $L = 40$ has 3121 qubits. The solid lines are guides to the eye. On the horizontal axis, β is proportional to the coupling to the environment and J is the exchange coupling of the effective interaction between nearest-neighbor qubits. In this simulation 80,000 iterations are used for each β step.

5.7.1 Results for the non-error sector $\mathcal{P}_{0,0}$

For the no-charge sector $\mathcal{P}_{0,0}$ we have $S^x(\mathcal{L}) = \mathbf{1}$. Our numerical results show that $\left|\frac{\mathcal{B}}{\mathcal{A}}\right|$ follows the local order parameter $\langle\sigma_i^x\rangle$, where i is an arbitrary qubit in the bulk of the surface code system. The behavior of $\left|\frac{\mathcal{B}}{\mathcal{A}}\right|$ as a function of βJ for nearest-neighbor interaction and different system sizes is shown in Fig. 5.4.

The surface code geometry can be decomposed into two sublattices. Here we considered square sublattices of sizes $L \times L$ and $(L-1) \times (L-1)$. By increasing the system size the transition from

the topological state, where $\beta J < \beta_c J$, to a trivial state where the degeneracy between $|s^*\rangle$ states is lifted, becomes sharper. This confirms the first-order phase transition nature of the effect (i.e., the existence of an error threshold in the fidelity). A finite-size scaling of the heat capacity is shown in Fig. 5.6. Taking β as a fictitious inverse temperature, we used $\frac{\beta^2(\langle E^2\rangle - \langle E\rangle^2)}{V}$ as the definition of heat capacity. Here V is the total number of qubits. By setting $J = 1$ and fitting the data to the asymptotic functional form $\beta_c(L) = \beta_c(\infty) - yL^x$, we find the critical exponent $x = -1/\nu = -1$, in agreement with the expected Ising model ($\nu = 1$). Scaling the data according to this functional form also gives $\beta_c(\infty) = 0.217$. This value agrees closely with the analytical result obtained in Ref. [98].

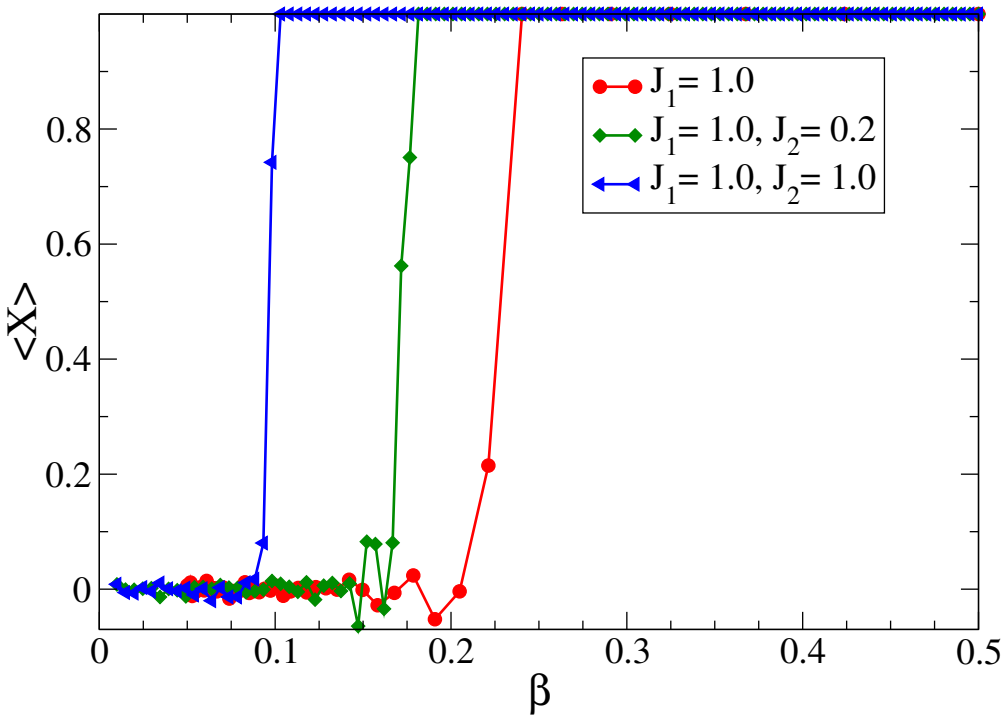

Figure 5.5: The ratio $\left|\frac{\mathcal{B}}{\mathcal{A}}\right|$ for different interaction ranges as a function of β on a lattice with $L = 40$ and 80,000 Monte Carlo steps for each data point. The data points correspond to $J_1 = 1$ (circles), as in Fig. 5.4; $J_1 = 1$, $J_2 = 0.2$, and $J_m = 0$ for $m > 2$ (diamonds); and $J_1 = 1$, $J_2 = 1$, and $J_m = 0$ for $m > 2$ (triangles) in Eq. (5.38). The solid lines are guides to the eye.

In this one-cycle study, the time period of the cycle, Δ, affects directly the range of interaction in

$H_{\rm eff}$ [see, for example, Eq. (5.11)], while the strength is proportional to β. Keeping the environment parameters fixed, the longer the error cycle, the longer the range of the interactions, as qubit correlations are intermediated by the propagation of environmental modes. To extend the analysis to qubit-qubit interactions beyond nearest neighbors, we write

$$H_{\rm eff} \;=\; -\sum_{m}\sum_{m\text{-th n.n }(ij)} J_m\,\sigma_i^x\,\sigma_j^x, \tag{5.38}$$

where J_m is the exchange coupling between m-th nearest neighbors (see Fig. 5.2). In Fig. 5.5 the behavior of $\left|\frac{\mathcal{B}}{\mathcal{A}}\right|$ as a function of β is shown for some fixed values of J_m. By increasing Δ the interaction range in $H_{\rm eff}$ varies and therefore one needs to take into account higher orders of m in Eq. (5.38).

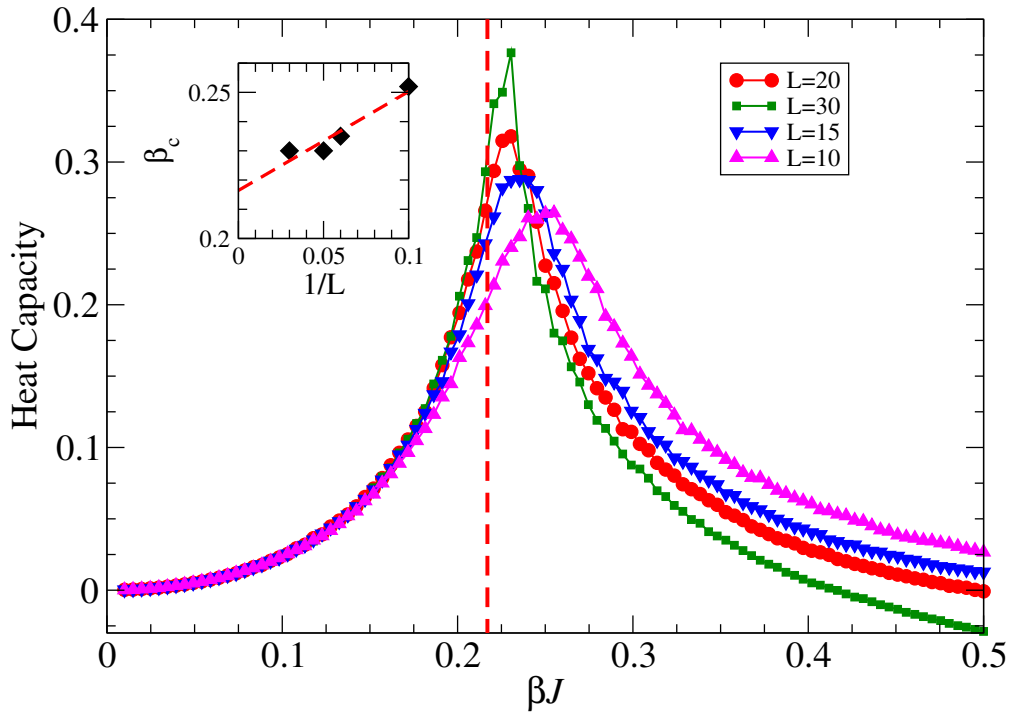

Figure 5.6: Finite-size scaling analysis of the heat capacity per qubit that yields $\beta_c = 0.217$ for $L \to \infty$. The solid lines are guides to the eye.

By including higher orders of m, the threshold value in the coupling to the environment for which the code protection is lost also changes. We see that a longer QEC cycle brings a larger range of correlated errors into account and consequently decreases the threshold value β_c. This indicates that for increasing values of Δ, a smaller coupling to the bath is sufficient to destroy the topological state of the surface code. We should emphasize that the effect is robust against increases of system size and the value of β_c is also well defined in the thermodynamic limit in this case. In general, the dependence of J_m on Δ is determined by the characteristics (correlation functions) of the environment; for bosonic environments this dependence was derived for some representative cases in Ref. [93]. We have numerically calculated the ratio $\left|\frac{\mathcal{B}}{\mathcal{A}}\right|$ for interaction ranges up to the fourth nearest neighbor. The results (not shown) confirm a trend of decreasing thresholds when the interaction range is increased.

5.7.2 Results for one-error sector $\mathcal{P}_{1,f}$ and the two-error sector $\mathcal{P}_{2,f}$

To investigate the intrinsic nature of the transition mentioned above we have also numerically evaluated $\langle S^x_{1,2}\rangle = \left|\frac{\mathcal{B}}{\mathcal{A}}\right|$ for charge sectors $\mathcal{P}_{1,f}$ (where a plaquette B_{p_0} is measured to be -1) and $\mathcal{P}_{2,f}$ (where two plaquettes B_{p_1} and B_{p_2} are measured -1). The locations of the errors $\{B_{p_0}\}$ and $\{B_{p_1}, B_{p_2}\}$ are arbitrarily chosen as shown in Fig. 5.7.

In the presence of detected errors, the numerical calculations require higher number of iterations. Figure 5.8 shows the gradual convergence of the results for the one- and two-error sectors to the results achieved for no-error sector. In these calculations only the nearest-neighbor case ($J_1 = 1$) has been considered. As can be seen in Fig. 5.8, for small values of β, complete convergence is not achieved when the number of iterations is just $O(10^4)$ per data point and a much larger data set is required. However, the data shows a clear tendency of convergence toward the same curve obtained for the no-error sector when the number of iterations is increased. The results for the case

with a larger range of correlated errors [$J_m \neq 0$ for $m > 1$ in Eq. (5.38)] converge toward their counterpart of no-error syndrome as well (not shown). In fact, we observe a faster convergence when the range of correlations is larger. Results for other non-zero error configurations different than the configurations considered here were found to be consistence with the results shown in Fig. 5.8. However, a larger distance between errors requires significantly higher number of computational iterations to achieve convergence.

5.8 Summary

A non-Markovian environment in contact with the surface code induces an effective dynamics (action) on the code system. Environmental degrees of freedom can intermediate interactions between physical qubits making up the system. As a result, when errors occur during the code evolution, they will be correlated. We considered the effect of such correlated errors on the fidelity of the code state after one error correction cycle. We studied the code state resulting from an effective action derived for a gapless bosonic environment but expect the same model to describe phenomenologically other types of environments. The calculation of the expectation values that enter in the fidelity can be cast in the form of expectation values of a statistical mechanics spin model with two separate phases. The disordered and ordered phases of the statistical version correspond to the topological and non-topological states of the surface code system in contact with the environment. We evaluated an upper bound for the threshold of the coupling to the bath beyond which no quantum error correction is possible (i.e., fidelity is fully lost).

We showed numerically that the transition between the two phases can be evaluated by a Monte Carlo method. We used a new definition for the stabilizers of the code based on the logical errors. The logical error in this definition plays a role equivalent to a world-line in the world-line based quantum Monte Carlo. The separation of the two phases of the surface code lies behind the

statistical physics of these world-lines, as presented in Eqs. (5.36) and (5.37). The alternative definition for stabilizers given in this paper can be extended to higher dimensional topological codes where the stabilizers are defined on hypercubes and logical errors correspond to closed hypersurfaces [99]. In higher dimensional codes the stabilizers can be defined in terms of the logical errors similar to Eqs. (5.33) and (5.34). Therefore, a similar approach should be applicable to those codes.

In the numerical evaluation we considered qubit-qubit interactions with different interaction ranges. We considered a QEC cycle with both zero and nonzero error syndromes. For the nearest-neighbor range the results perfectly agrees with the analytical calculations in Ref. [98]. Finite-size scaling shows the value for the threshold β_c to be close to half of an Ising model with nearest-neighbor interaction. For longer range of interactions the threshold β_c decreases. The type of error syndrome does not affect the value β_c. However, higher numerical iterations were required to achieve convergence beyond nonerror syndromes.

Our results are based on the assumption that the interaction between the physical qubits and the environment has the form $V_{BC} = \lambda \sum_{r_i} f(r_i)\, \sigma_i^x$. Different functional forms for this interaction may result in a different effective evolution operator U_{eff} than the one studied here and may set different threshold values for the fidelity. Another question that should be addressed is the behavior of the fidelity over multiple QEC cycles. Both issues are open to future investigations.

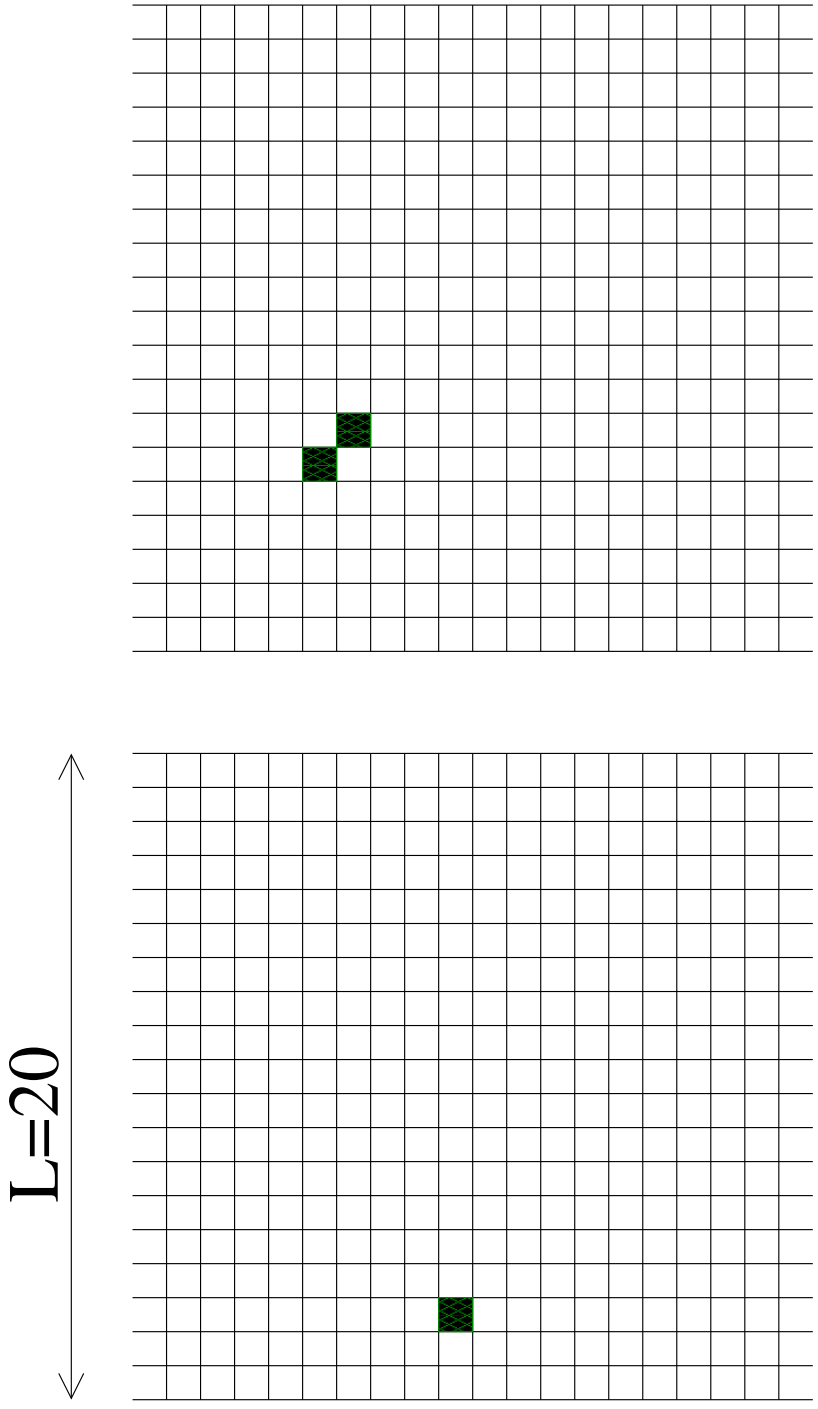

Figure 5.7: The location of the single error $\{B_{p_0}\}$ (bottom) and two errors $\{B_{p_1}, B_{p_2}\}$ (top) assumed in the numerical calculations.

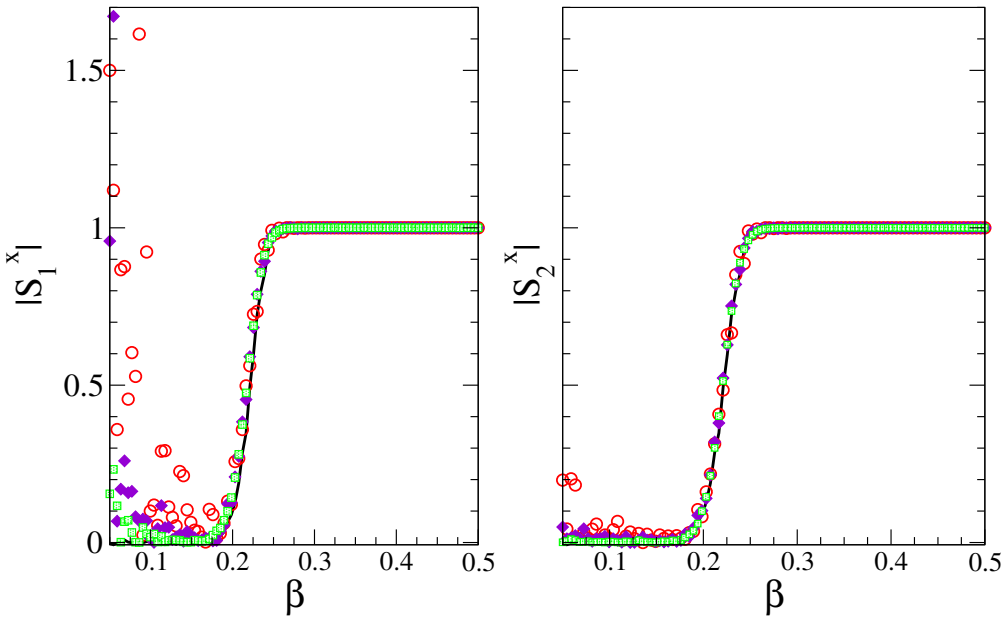

Figure 5.8: The ratio $|\frac{\mathcal{B}}{\mathcal{A}}|$ for a lattice of $L = 20$. The left box shows the convergence of $\langle S_1^x \rangle = |\frac{\mathcal{B}}{\mathcal{A}}|$ for one detected error located as shown in Fig. 5.7. The right box shows the convergence of $\langle S_2^x \rangle = |\frac{\mathcal{B}}{\mathcal{A}}|$ for two detected errors located as shown in Fig. 5.7. In both boxes the number of iterations used for each β data point is: $90,000$ (circle), $180,000$ (square), and $900,000$ (diamonds). The solid line is obtained from the corresponding no-error sector (Fig. 5.5).

CHAPTER 6: FIDELITY THRESHOLD OF THE SURFACE CODE BEYOND SINGLE-QUBIT ERROR MODELS

- Pejman Jouzdani, E. Novais, I. S. Tupitsyn, and Eduardo R. Mucciolo, "Fidelity threshold of the surface code beyond single-qubit error models", Phys. Rev. A **90**, 042315 (2014).

6.1 Abstract

The surface code is a promising alternative for implementing fault-tolerant, large-scale quantum information processing. Its high threshold for single-qubit errors under stochastic noise is one of its most attractive features. We develop an exact formulation for the fidelity of the surface code that allows us to probe much further on this promise of strong protection. This formulation goes beyond the stochastic single-qubit error model approximation and can take into account both correlated errors and inhomogeneities in the coupling between physical qubits and the environment. For the case of a bit-flipping environment, we map the complete evolution after one quantum error correction cycle onto the problem of computing correlation functions of a two-dimensional Ising model with boundary fields. Exact results for the fidelity threshold of the surface code are then obtained for several relevant types of noise. Analytical predictions for a representative case are confirmed by Monte Carlo simulations.

6.2 Introduction

Quantum error correction (QEC) is one of the most important tools to reduce the effects of decoherence in quantum systems that process information. Several different protocols have been de-

veloped since QEC was first introduced [100], but particular attention has been given to stabilizer codes [101]. Among them, the surface code [24, 23] is perhaps the most promising for large-scale implementations [54]. Its main virtues are: (i) qubits are disposed in a planar array, only requiring local measurement operations; and (ii) early estimates based on stochastic error models indicate a very large threshold value, $p_c \approx 11\%$ [23], for the single-qubit error probability p. For $p < p_c$, the probability of successful encoding tends to 1 as the number of physical qubits is increased.

Despite the large theoretical effort that has been devoted to characterizing the threshold of the surface code [23, 102, 52, 103, 104, 105], the true nature of the transition has been hard to assess due to the large Hilbert space that the code demands. Some criticism has also been raised by the use of simplified error models in these studies, since, for more traditional QEC schemes, error models that take into account correlations can substantially alter or even remove error thresholds [37, 60, 106]. In this paper we make significant progress on both issues. We consider more general bit-flip error models with and without disorder and correlations. We derive an exact mapping of a complete QEC quantum evolution with arbitrary syndrome onto a two-dimensional Ising model with complex temperature. Exact results are then obtained for what we call the "one-cycle threshold". Our main conclusion is a positive one: a fidelity threshold exists in most cases, although its value is not universal, depending on the noise model. For a representative case, the analytical prediction for the threshold location based on the mapping is supported by Monte Carlo simulations.

The remaining of the chapter is organized as follows. In Sec. 6.3 we discuss the difference between intrinsic and effective thresholds, which is crucial for the understanding of our results. The next two sections are mainly a review: Sec. 6.4 contains a concise description of the surface code and Sec. 6.5 describes the code's evolution, syndrome extraction, and error correction within one cycle in very general terms. The description of our work begins in Sec. 6.6, where some basic assumptions and definitions are provided and a suitable expression for the fidelity is presented. This is followed by a discussion in Sec. 6.7 of decoding and the thermodynamic limit in the

determination of the threshold. A realistic error model that induces bit-flip errors is introduced in Sec. 6.8 and consists of an effective action involving single-qubit and two-qubit interaction terms. Using this error model and considering the full quantum evolution of the physical qubits, in Sec. 6.9 we map the fidelity calculation after one QEC cycle onto the evaluation of correlation functions of a two-dimensional Ising model. In Sec. 6.10 we discuss several scenarios based on that mapping, including cases with homogeneous and inhomogeneous couplings. In Sec. 6.11 we present the result of Monte Carlo simulations of the fidelity threshold and confirm the analytical prediction based on the mapping for the homogeneous coupling case. Conclusions are provided in Sec. 6.12

6.3 Intrinsic and effective thresholds

Two QEC strategies can be used for any stabilizer code. In the so-called active QEC, stabilizer operators are measured and, based on their syndromes, a recovery operation is chosen and implemented. In passive QEC, the physical qubits are subjected to a Hamiltonian that enforces an energy gap between the code word subspace and the rest of the Hilbert space of the physical qubits. Typically, the Hamiltonian consists of a sum over all stabilizer operators multiplied by a negative constant. Protection in this case requires neither measurements nor recovery operations. While the surface code introduced by Dennis and coworkers [23] is an example of active QEC, the original toric code of Kitaev [25] is its passive counterpart.

Now, consider adding to the toric code a static perturbation that acts directly on the physical qubits and competes with the code's intrinsic Hamiltonian [38]. Several authors have shown that beyond a certain critical value of the perturbation's coupling constant, the toric Hamiltonian is no longer capable of protecting the code word subspace; topological order is completely lost and so is the spectral gap separating the ground state subspace from the excited states [107, 108, 90]. In this

context, it is clear that the critical value of the coupling constant provides an intrinsic threshold: any perturbation larger than the threshold renders the code completely ineffective even when the code distance is increased. It is natural to assume that different types of perturbations will have distinct thresholds.

In this paper we extend the concept of intrinsic thresholds to active QEC. While for passive QEC the intrinsic threshold reveals itself as a clear-cut quantum phase transition, in active QEC the situation is a more subtle because the outcome of the QEC cycle depends on the syndromes, their decoding, and the recovery operation. Thus, it is natural to look for the intrinsic threshold in the most favorable situation, one that is not affected by a particular decoding strategy for codes. This happens in the case of a nonerror syndrome, when no recovery operation is recommended. For any other syndrome, the threshold must be less favorable because there can be a certain amount of uncertainty as to which recovery operation is more effective.

Within this approach, we distinguish two kinds of thresholds:

- An intrinsic one, which depends only on the interaction between the physical qubits and the environment and is independent of any decoding procedure.
- An effective one, which depends on the interaction between the physical qubits and the environment and on the decoding procedure.

This distinction is valid for any stabilizer code. The effective threshold is always equal or smaller than the intrinsic threshold. The effective threshold can always be increased by improving the decoding procedure until it reaches the intrinsic value. Thus, perfect decoding makes the effective threshold equal to the intrinsic one in the limit when the code distance goes to infinity.

In the context of the surface code, the existence of threshold has been demonstrated by associating

it to a phase transition of a classical statistical spin model with quenched disorder [90]. The proof assumes that physical qubits are subjected to independent depolarizing noise sources, uncorrelated in time, with recovery from those errors requiring a syndrome decoding strategy. In this paper we go further and argue that, in general, an *intrinsic* threshold may exist independently of the syndrome decoding procedure adopted, being only determined by the error model. We show that an intrinsic threshold exists for a noise source where spatial correlations among physical qubits are induced by their interaction with a common environment. The threshold in this case is associated to a finite-temperature phase transition of a two-dimensional Ising model, with the coupling constant between physical qubits and the environment playing the role of the inverse temperature of the model.

6.4 The surface code and the stabilizer formalism

In a QEC stabilizer protocol, information is encoded into a much larger Hilbert space than the minimum space physically required. Different sectors of this large Hilbert space are labeled by different values of observables associated to operators known as stabilizers. A judicial choice for the stabilizers can then be used to diagnose the most common type of error for a given quantum evolution. Based on the outcomes (syndromes) of measurements of stabilizer operators, a forceful return to the logical Hilbert space is performed.

The surface code consists of a two-dimensional array of qubits placed on the edges of a square lattice, see Fig. 6.1. These physical qubits can be implemented with Josephson junctions [82], cold atoms [111], trapped ions [112], Rydberg atoms [57], or semiconductor quantum dots [113].

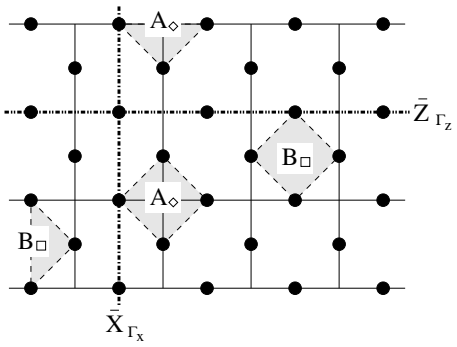

Figure 6.1: Schematic representation of the surface code. The circles are physical qubits. The gray squares represent plaquettes ($B_\square$) and stars ($A_\diamondsuit$). The product of single-qubit operators along the dashed-dotted lines Γ_X (vertical) and Γ_Z (horizontal) define the logical operators $\bar{X}_{\Gamma_X}$ and $\bar{Z}_{\Gamma_Z}$, respectively.

The stabilizers of the code are the plaquette operators

$$B_\square = \prod_{\mathbf{i}\in\square} \sigma_{\mathbf{i}}^z \tag{6.1}$$

and the star operators

$$A_\diamondsuit = \prod_{\mathbf{i}\in\diamondsuit} \sigma_{\mathbf{i}}^x, \tag{6.2}$$

where $\sigma_i^{x,z}$ are the Pauli operators x and z of qubit i. The logical operations are defined as strings of physical qubit operations:

$$\bar{X}_{\Gamma_X} = \prod_{\mathbf{i}\in\Gamma_X} \sigma_{\mathbf{i}}^x \tag{6.3}$$

and

$$\bar{Z}_{\Gamma_Z} = \prod_{\mathbf{i}\in\Gamma_Z} \sigma_{\mathbf{i}}^z, \tag{6.4}$$

where Γ_Z is a path that cuts through the lattice from left to right and Γ_X is a path that goes from

top to bottom [114]. Finally, the codewords can be written as

$$\left|\bar{\uparrow}\right\rangle = G\left|F_z\right\rangle \tag{6.5}$$

and

$$\left|\bar{\downarrow}\right\rangle = \bar{X}_{\Gamma_X} G\left|F_z\right\rangle, \tag{6.6}$$

where

$$G = \frac{1}{\sqrt{2^{N_\diamond}}} \prod_{\diamond} (1 + A_\diamond) \tag{6.7}$$

and

$$\left|F_z\right\rangle = \left|\uparrow\right\rangle_{\mathbf{1}} \otimes \cdots \otimes \left|\uparrow\right\rangle_{\mathbf{N}} \tag{6.8}$$

is the ferromagnet state in the z component of the physical qubits. Here, $N_\diamond$ denotes the number of star operators on the lattice and N is the total number of physical qubits. The product $\bar{X}_{\Gamma_X} G$ is independent of the particular choice of Γ_X and uniquely defines $\left|\bar{\downarrow}\right\rangle$ (thus, hereafter we will drop the path subscript in the logical operators). The logical space is a two-dimensional Hilbert space where all plaquettes and stars, when measured, return the value $+1$; by convention, this set is called the zero charge sector. All other sets define sectors with nonzero charge and are characterized by the number of -1 syndrome values for the plaquette and star operators.

6.5 Quantum evolution, syndrome, and error correction

To make the discussion more concise, and without loss of generality for the case of bit-flip errors, let us assume that the system is initially prepared in the logical state $\left|\bar{\uparrow}\right\rangle$ and is not entangled with the environment $\left|e\right\rangle$,

$$\left|\Psi(0)\right\rangle = \left|\bar{\uparrow}, e\right\rangle. \tag{6.9}$$

The logical qubit and the environment evolve under a unitary evolution operator $U(\Delta)$ for a time Δ,

$$|\Psi(\Delta)\rangle = U(\Delta)\,|\Psi(0)\rangle. \tag{6.10}$$

Since we are assuming only bit-flip errors, stars will remain always with eigenvalue 1 under this evolution. On the other hand, plaquettes may have eigenvalue ± 1. Let us call $\{p\}$ a set of plaquettes that return a nontrivial syndrome, thus indicating an error. When the stabilizers are measured, the system's state vector is projected by the operator

$$\mathcal{P}_{\{p\}} = \frac{1}{2^{N_\square}} \prod_{\square'} (1 + B_{\square'}) \prod_{p} (1 - B_p)\,, \tag{6.11}$$

where $\square'$ is the set of plaquettes with eigenvalue $+1$. The decoding procedure associates to a syndrome a certain recovery operation. In the surface code, this corresponds to choosing a string $\mathcal{S}^x_{\{p\}}$ made of a product of $\sigma^x_{\mathbf{i}}$ operators that connect the plaquettes in $\{p\}$ pairwise or to the boundaries. This recovery operation results in the unnormalized state vector

$$\begin{aligned} |\Psi_{\mathrm{QEC}}\rangle_{\{p\}} &= \mathcal{S}^x_{\{p\}} \mathcal{P}_{\{p\}} |\Psi(\Delta)\rangle \\ &= \mathcal{S}^x_{\{p\}} \mathcal{P}_{\{p\}} U\,(\Delta)\,\left|\bar{\uparrow}, e\right\rangle. \end{aligned} \tag{6.12}$$

A small but important simplification can be made: notice that

$$\begin{aligned} \mathcal{S}^x_{\{p\}} \mathcal{P}_{\{p\}} &= \frac{1}{2^{N_\square}} \mathcal{S}^x_{\{p\}} \prod_{\square'} (1 + B_{\square'}) \prod_{p} (1 - B_p) \\ &= \frac{1}{2^{N_\square}} \prod_{\square} (1 + B_{\square})\, \mathcal{S}^x_{\{p\}}, \end{aligned} \tag{6.13}$$

where in the second line the product over plaquettes is unconstrained. Therefore,

$$|\Psi_{\rm QEC}\rangle_{\{p\}} = \frac{1}{2^{N_\Box}} \prod_\Box (1 + B_\Box)\, \mathcal{S}^x_{\{p\}} U(\Delta) \left|\bar{\uparrow}, e\right\rangle . \tag{6.14}$$

The presence of the projector $\prod_\Box (1+B_\Box)$ on the right-hand side of Eq. (6.14) implies that $|\Psi_{\rm QEC}\rangle$ contains only qubit states with all plaquettes positive, i.e., it can be represented by a superposition of the two logical states $|\bar{\uparrow}\rangle$ and $|\bar{\downarrow}\rangle$. The amplitude of each state depends on the choice of $\mathcal{S}_{\{p\}}$. A good choice will favor $|\bar{\uparrow}\rangle$.

Even though there is a large number of strings $\mathcal{S}^x_{\{p\}}$ compatible with the syndrome $\{p\}$, they can be sorted into two distinct classes related by the logical operator $\bar{X}$. The product $\mathcal{S}^x_{\{p\}} G$, implicit in the evolution of the logical qubit in Eq. (6.14), generates all possible strings within a class. Therefore, the particular choice of $\mathcal{S}^x_{\{p\}}$ to represent a class is irrelevant to the calculation of the fidelity of the code. After choosing a string $\mathcal{S}^x_{\{p\}}$, we can assign $\bar{X}\mathcal{S}^x_{\{p\}}$ to represent the elements of the other class.

Thus, if the recovery operation $\mathcal{S}^x_{\{p\}}$ brings the logical qubit state back to $|\bar{\uparrow}\rangle$, its counterpart $\bar{X}\mathcal{S}^x_{\{p\}}$ takes it to the state $|\bar{\downarrow}\rangle$. We can then write the (unnormalized) state vector at the end of the QEC cycle as

$$|\Psi_{\rm QEC}\rangle_{\{p\}} = |\bar{\uparrow}\rangle\langle\bar{\uparrow}|\mathcal{S}^x_{\{p\}} U(\Delta)|\bar{\uparrow}, e\rangle + |\bar{\downarrow}\rangle\langle\bar{\uparrow}|\bar{X}\mathcal{S}^x_{\{p\}} U(\Delta)|\bar{\uparrow}, e\rangle. \tag{6.15}$$

[Notice the partial contraction in the expectation values appearing on the right-hand side of Eq. (6.15); environmental degrees of freedom remain non contracted.] In the case of a bad recovery operation, the roles of $\mathcal{S}^x_{\{p\}}$ and $\bar{X}\mathcal{S}^x_{\{p\}}$ are swapped. The fact that one cannot be completely sure of the efficacy of the recovery operation is the reason why the effective threshold is always equal or smaller than the intrinsic threshold.

6.6 Environment resetting and the one-cycle fidelity

After one QEC cycle, the fidelity of the system comprising the physical qubits can be generally defined as

$$\mathcal{F}_{\{p\}} \equiv \frac{\left|\langle\Psi(0)|\Psi_{\rm QEC}\rangle_{\{p\}}\right|^2}{||\Psi_{\rm QEC}||^2}, \tag{6.16}$$

where $\{p\}$ is the set of syndromes obtained. This definition implies that if the environment evolves to a state orthogonal to the ground state, the fidelity must goes to zero regardless of the final state of the qubits.

Here we avoid this situation by assuming that the environment is reset to its ground state. It is physically reasonable to assume that the environment's excitations can be suppressed by some "cooling" mechanism (e.g., lowering the temperature, applying a polarizing field, etc). This assumption was previously discussed in Refs. [66, 93]. Assuming this resetting of the environment at the end of the QEC cycle, we can rewrite Eq. (6.15) as

$$|\Psi_{\rm QEC}\rangle_{\{p\}} = \mathcal{A}_{\{p\}}|\bar{\uparrow}, e\rangle + \mathcal{B}_{\{p\}}|\bar{\downarrow}, e\rangle, \tag{6.17}$$

where we have introduced the amplitudes

$$\mathcal{A}_{\{p\}} = \left\langle\bar{\uparrow}, e\right| \mathcal{S}^x_{\{p\}} U\left(\Delta\right) \left|\bar{\uparrow}, e\right\rangle \tag{6.18}$$

and

$$\mathcal{B}_{\{p\}} = \left\langle\bar{\uparrow}, e\right| \bar{X}\mathcal{S}^x_{\{p\}} U\left(\Delta\right) \left|\bar{\uparrow}, e\right\rangle, \tag{6.19}$$

for each syndrome outcome characterized by the set $\{p\}$. As a result, after some simple manipula-

tions [66], we can write

$$\mathcal{F}_{\{p\}} = \frac{\left|\mathcal{A}_{\{p\}}\right|^2}{\left|\mathcal{A}_{\{p\}}\right|^2 + \left|\mathcal{B}_{\{p\}}\right|^2}. \tag{6.20}$$

Maintaining maximum fidelity at the end of the QEC cycle implies $\mathcal{F}_{\{p\}} = 1$. Maximum loss of fidelity results from a complete uncertainty about the logical state, $|\mathcal{A}_{\{p\}}| = |\mathcal{B}_{\{p\}}|$, and, consequently, $\mathcal{F}_{\{p\}} = \frac{1}{2}$ [39].

When the coupling between the physical qubits and the environment is sufficiently weak, one can expand the evolution operator $U(\Delta)$ in terms of strings of operators $\sigma_{\mathbf{i}}^x$ of increasing length. Each string represents a certain number of bit-flip events, with that number defining the length of the string. Looking at Eq. (6.18), one recognizes that the shortest string in the expansion that gives a nonzero contribution to $\mathcal{A}_{\{p\}}$ corresponds exactly to the string of $\sigma_{\mathbf{i}}^x$ operators in $\mathcal{S}_{\{p\}}$. Therefore, the order of the leading contribution to $\mathcal{A}_{\{p\}}$ is equal to the smallest possible length of $\mathcal{S}_{\{p\}}$. Similarly, the leading contribution to $\mathcal{B}_{\{p\}}$ has an order equal to the smallest possible length of $\bar{X}\,\mathcal{S}_{\{p\}}$. Therefore, in the weak-coupling limit, whenever $\mathcal{S}_{\{p\}}$ is shorter than $\bar{X}\,\mathcal{S}_{\{p\}}$ (namely, when it involves fewer bit flips), one expects $|\mathcal{A}_{\{p\}}| > |\mathcal{B}_{\{p\}}|$. In the strong coupling limit, on the other hand, any perturbative expansion fails; in those circumstances, we expect $\mathcal{A}_{\{p\}}$ and $\mathcal{B}_{\{p\}}$ to have similar magnitudes on a finite lattice.

The dependence of $\mathcal{A}_{\{p\}}$ and $\mathcal{B}_{\{p\}}$ on the lengths of $\mathcal{S}_{\{p\}}$ and $\bar{X}\,\mathcal{S}_{\{p\}}$, respectively, give us a hint to the appropriate decoding procedure and thermodynamic limit we need to adopt in order to define a fidelity threshold.

6.7 Decoding and the thermodynamic limit

The expression for the fidelity given in Eq. (6.20) is only valid under the assumption that the decoding of the syndromes is flawless, such that $\left|\mathcal{A}_{\{p\}}\right| > \left|\mathcal{B}_{\{p\}}\right|$. In practice, finding a recovery

operation $\mathcal{S}^x_{\{p\}}$ that fulfills this inequality for any given syndrome set $\{p\}$ is a difficult task. A rich literature exists on decoding algorithms for the surface code; see, for instance, [23, 70, 40, 41] and references therein, where a number of strategies have been proposed. Here, we do not attempt to improve on the existing strategies. We offer instead a prescription where the inequality is always satisfied in the limit of infinite code distance (i.e., infinite lattice sizes). As we argue below, when the inequality holds, the fidelity threshold obtained from from Eq. (6.20) is equal to the intrinsic threshold. However, since it is not possible to guarantee that the decoding is flawless in practice, at times we will have $\left|\mathcal{A}_{\{p\}}\right| < \left|\mathcal{B}_{\{p\}}\right|$. Therefore, an effective fidelity threshold that takes into account the possibility of flawed recovery operations should always be smaller than the intrinsic one.

Our prescription for enforcing $\left|\mathcal{A}_{\{p\}}\right| > \left|\mathcal{B}_{\{p\}}\right|$ begins by recognizing that the amplitudes $\mathcal{A}_{\{p\}}$ and $\mathcal{B}_{\{p\}}$ are functions of the lattice size used to encode the logical qubit. Therefore, it is important to define what we call the *thermodynamic limit*. Let us start with a fixed and finite set $\{p\}$ containing an even number of plaquettes and assume that the limit is taken by constructing a sequence of lattices of increasing size. Consider the smallest lattice that can contain the set $\{p\}$ as the initial element of the sequence. The next element in the sequence is constructed from the previous one by adding rows and columns to all four boundaries of the lattice. As a consequence, *the distance from any plaquette in* $\{p\}$ *to the boundaries increases with increasing lattice sizes*. We now choose a string $\mathcal{S}^x_{\{p\}}$ made of a product of $\sigma^x_{\mathbf{i}}$ operators that connect pairwise the plaquettes in $\{p\}$ without reaching the boundaries. By this choice, the string operator $\bar{X}\mathcal{S}_{\{p\}}$ used in the computation of $\mathcal{B}_{\{p\}}$ always reaches the boundaries while $\mathcal{S}^x_{\{p\}}$ does not. As the lattice grows, the length of $\bar{X}\mathcal{S}_{\{p\}}$ surpasses that of $\mathcal{S}^x_{\{p\}}$. As described in Sec. 6.6, in the weak coupling limit, $\mathcal{B}_{\{p\}}$ is strongly suppressed in comparison to $\mathcal{A}_{\{p\}}$. Thus our choice of $\mathcal{S}^x_{\{p\}}$ ensures that, in the limit of infinite lattice size, the inequality $\left|\mathcal{A}_{\{p\}}\right| > \left|\mathcal{B}_{\{p\}}\right|$ is satisfied.

The prescription needs to be slightly modified when $\{p\}$ contains an odd number of plaquettes.

After connecting all but one plaquette with strings pairwise, we connect the unpaired plaquette (presumably the most remote one) by a string to the closest boundary. We then keep that boundary fixed and construct the sequence of lattices by adding columns to the left and right boundaries but adding rows only to the opposite boundary. Thus, the one string in $\mathcal{S}^x_{\{p\}}$ reaching a boundary will keep its length fixed, while the counterpart of that string in $\bar{X}\mathcal{S}_{\{p\}}$ will reach the opposite boundary with an increasing length. This guarantees that $\left|\mathcal{A}_{\{p\}}\right| > \left|\mathcal{B}_{\{p\}}\right|$ is also satisfied.

With this definition of the thermodynamic limit at hand, we define the one-cycle threshold for the surface code as the largest value of coupling between the physical qubits and the environment such that, in the *thermodynamic limit*, $\mathcal{F}_{\{p\}} \to 1$ *for any* finite set $\{p\}$. In particular, the intrinsic threshold corresponds to the non-error syndrome, namely, when $\{p\}$ is an empty set. A proof that an intrinsic threshold always exists for the error model defined in Sec. 6.8 is given in Appendix B. Our prescription for the thermodynamic limit also allows us to show in Sec. 6.9 that, for an error model with only nearest-neighbor qubit interactions, the fidelity threshold derived from Eq. (6.20) is independent of the syndrome set $\{p\}$ and thus equal to the intrinsic threshold.

In our prescription for the thermodynamic limit we first fix the syndrome set $\{p\}$ and then take the lattice size to infinity. Thus, the density of plaquettes with eigenvalues -1 tends to zero. This procedure is quite adequate for our goal of establishing the intrinsic threshold irrespective of the syndrome $\{p\}$, as we argue in Sec. 6.10.

An alternative definition of the thermodynamic limit, commonly used in numerical investigations using stochastic error models, would keep the density of plaquettes with eigenvalues -1 fixed as the lattice size is increased. Therefore, the set $\{p\}$ would be different and larger for each new lattice size and a recalculation of the amplitudes $\mathcal{A}_{\{p\}}$ and $\mathcal{B}_{\{p\}}$ would be required at each new step. Thus, in addition to being much harder to be analyzed, such a prescription does not guarantee that the inequality $|\mathcal{A}_{\{p\}}| > |\mathcal{B}_{\{p\}}|$ is satisfied in the thermodynamic limit. Therefore, it is not suitable for

determining a fidelity threshold from Eq. (6.20).

6.8 The error model

In realistic implementations, the physical qubits interact with a variety of environmental degrees of freedom [42]. For instance, frequently one cannot neglect the interaction of qubits with bosonic environments [60]. These can come directly from phonons and electromagnetic fluctuations generated by electronic components, or indirectly from interactions with spin or charge impurities. It is also possible that imperfections in qubit design cause spurious coupling between single-qubit states. Finally, it is also possible that qubits couple to a spin (or pseudo-spin) bath. For these cases and others, the effect of a time evolution under the influence of the environment can be recast as an effective action for the physical qubits by integrating out the environmental degrees of freedom. Thus, at the end of a QEC cycle, an effective evolution operator of the form

$$U_{\rm eff} = \langle e|U(\Delta)|e\rangle = e^{-H_{\rm eff}} \tag{6.21}$$

can be derived and employed in the calculation of matrix elements and probability amplitudes involving physical qubits. The exact form of $H_{\rm eff}$ depends on the particular type of interaction and the nature of the physical qubits and the environment. Here, we consider the two-term expression

$$H_{\rm eff}\left(\{\sigma_{\mathbf{i}}^x\}\right) = \sum_{\mathbf{i}} h_{\mathbf{i}}\,\sigma_{\mathbf{i}}^x + \sum_{\mathbf{i}\neq\mathbf{j}} J_{\mathbf{i},\mathbf{j}}\,\sigma_{\mathbf{i}}^x\sigma_{\mathbf{j}}^x. \tag{6.22}$$

The parameters $h_{\mathbf{i}}$ and $J_{\mathbf{ij}}$ incorporate environmental fields and qubit-qubit interactions, respectively, and can be either real or imaginary numbers. Their magnitudes set the strength of the coupling between physical qubits and the environment. This form is exact for qubits coupled linearly to free bosonic baths and local fields [93]. We note that $J_{\mathbf{ij}}$ can also represent direct interactions

between qubits that are not environment mediated.

6.9 Mapping onto an unconstrained Ising model

Let us write expressions for the amplitudes $\mathcal{A}_{\{p\}}$ and $\mathcal{B}_{\{p\}}$ as sums over configurations of the variables $\{\sigma_{\mathbf{i}}^x\}$. We begin by replacing each state $|\uparrow\rangle_{\mathbf{i}}$ in Eq. (6.8) by $\frac{1}{\sqrt{2}}\left(|+\rangle_{\mathbf{i}} + |-\rangle_{\mathbf{i}}\right)$, where $\hat{\sigma}_{\mathbf{i}}^x|\pm\rangle_{\mathbf{i}} = \pm|\pm\rangle_{\mathbf{i}}$. Introducing the notation $\hat{\sigma}_{\mathbf{i}}^x|\sigma_{\mathbf{i}}\rangle = \sigma_{\mathbf{i}}|\sigma_{\mathbf{i}}\rangle$, we have

$$|\bar{\uparrow}\rangle = \sum_{\sigma}{}' \, |\sigma\rangle \tag{6.23}$$

up to a normalization factor. Here σ stands for $(\sigma_{\mathbf{1}}, \ldots, \sigma_{\mathbf{N}})$. The sum in Eq. (6.23) is restricted to the configurations σ that satisfy the constraint $A_{\diamondsuit} = +1$ for all stars (i.e., vertices) in the lattice. We substitute Eq. (6.23) in the definitions of the amplitudes $\mathcal{A}_{\{p\}}$ and $\mathcal{B}_{\{p\}}$ [Eqs. (6.18) and (6.19)] and use Eq. (6.21) to arrive at

$$\mathcal{A}_{\{p\}} = \sum_{\sigma}{}' \, \mathcal{S}_{\{p\}}^x \, e^{-H_{\text{eff}}(\sigma)} \tag{6.24}$$

and

$$\mathcal{B}_{\{p\}} = \sum_{\sigma}{}' \bar{X} \, \mathcal{S}_{\{p\}}^x \, e^{-H_{\text{eff}}(\sigma)}. \tag{6.25}$$

The operator $S_{\{p\}}^x$ now represents a string of variables $\sigma_{\mathbf{i}}$ compatible with the syndrome represented by the set of plaquettes $\{p\}$.

The sums in Eqs. (6.24) and (6.25) are very difficult to evaluate (see Ref. [66]). Below, we provide an exact solution to this problem for a particular but significant case.

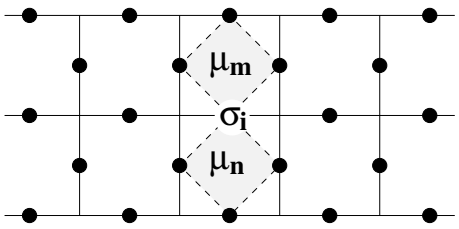

Figure 6.2: Qubit variable $\sigma_{\mathbf{i}}$ and corresponding plaquette variables $\mu_{\mathbf{m}}$ and $\mu_{\mathbf{n}}$.

6.9.1 Nearest-neighbor correlations

Let us consider the case where $J_{\mathbf{ij}}$ describes only nearest-neighbor interactions. To overcome the restriction in the sums in Eqs. (6.24) and (6.25), we introduce plaquette variables $\{\mu_{\mathbf{m}}\}$, with $\mu_{\mathbf{m}} = \pm 1$, such that $\sigma_{\mathbf{i}} = \mu_{\mathbf{m}}\,\mu_{\mathbf{n}}$ (see Fig. 6.2). The subscript $\mathbf{i}$ refers to the physical qubit $\mathbf{i}$ while $\mathbf{m}$ and $\mathbf{n}$ indicate the plaquettes sharing the link $\mathbf{i}$. Even though the variables $\{\mu_{\mathbf{m}}\}$ can be positive or negative, they automatically satisfies the constraint of positive star eigenvalues. This parameterization is well known in the lattice gauge field literature [109]. Thus, starting from the error model defined in Eq. (6.22) and introducing these new variables, it is straightforward to show that, for nearest-neighbor qubits $\mathbf{i}$ and $\mathbf{j}$ in the bulk (i.e., not at the top or bottom edges),

$$h_{\mathbf{i}}\,\sigma_{\mathbf{i}}^{x} \longrightarrow h_{\mathbf{i}}\,\mu_{\mathbf{m}}\mu_{\mathbf{n}} \tag{6.26}$$

and

$$J_{\mathbf{ij}}\,\sigma_{\mathbf{i}}^{x}\,\sigma_{\mathbf{j}}^{x} \longrightarrow J_{\mathbf{ij}}\,\mu_{\mathbf{u}}\,\mu_{\mathbf{v}}, \tag{6.27}$$

where the plaquettes $\mathbf{u}$ and $\mathbf{v}$ are next-to-nearest neighbors containing the links $\mathbf{i}$ and $\mathbf{j}$, respectively [see Fig. 6.3(a)]. Notice that the same product $\mu_{\mathbf{u}}\,\mu_{\mathbf{v}}$ appears again when we consider the contribution from the other pair of nearest-neighbor links $\mathbf{i}'$ and $\mathbf{j}'$ belonging to these plaquettes.

Thus, we can define $\tilde{h}_{\mathbf{mn}} = h_{\mathbf{i}}$ such that

$$\sum_{\mathbf{i}\in\text{bulk}} h_{\mathbf{i}}\,\sigma^x_{\mathbf{i}} = \sum_{\langle\mathbf{m},\mathbf{n}\rangle} \tilde{h}_{\mathbf{mn}}\,\mu_{\mathbf{m}}\,\mu_{\mathbf{n}}, \tag{6.28}$$

as well as $\tilde{J}_{\mathbf{uv}} = J_{\mathbf{ij}} + J_{\mathbf{i'j'}}$ such that

$$\sum_{\langle\mathbf{i},\mathbf{j}\rangle\in\text{bulk}} J_{\mathbf{ij}}\,\sigma^x_{\mathbf{i}}\,\sigma^x_{\mathbf{j}} = \sum_{\mathbf{u},\mathbf{v}} \tilde{J}_{\mathbf{uv}}\,\mu_{\mathbf{u}}\,\mu_{\mathbf{v}}, \tag{6.29}$$

where $\langle\mathbf{m},\mathbf{n}\rangle$ are nearest-neighbor plaquettes and $\mathbf{u},\mathbf{v}$ are next-to-nearest neighbors. The new parameters are functions of $h_{\mathbf{i}}$ and $J_{\mathbf{ij}}$. Notice that for homogeneous fields and couplings in the bulk, $h_{\mathbf{i}} = h$ and $J_{\mathbf{ij}} = J$, we get $\tilde{h}_{\mathbf{mn}} = \tilde{h} = h$ and $\tilde{J}_{\mathbf{uv}} = \tilde{J} = 2J$.

A little more work is needed to understand the constraint of positive stars at the bottom and top boundaries (see Fig. 6.1). A star at these boundaries is formed by the product of three qubits; for instance, $A_1 = \sigma^x_1\,\sigma^x_2\,\sigma^x_3 = 1$. One of these qubits belongs to the bulk and can be written in terms of plaquette variables, $\sigma^x_2 = \mu_1\,\mu_3$. Therefore, we obtain $\mu_1\sigma^x_1\,\mu_3\,\sigma^x_3 = 1$ and, consequently, $\mu_1\,\sigma^x_1 = \mu_3\,\sigma^x_3 = \pm 1$. This can be repeated for all qubits at the boundary. As a result, the product of any pair $\mu_{\mathbf{m}}\,\sigma^x_{\mathbf{i}}$ at the boundaries is a constant ± 1 (here $\mathbf{m}$ denotes the plaquette where the boundary link $\mathbf{i}$ is located.) Thus, for sites at the top t and bottom b boundaries, we can write

$$h_{\mathbf{i}}\,\sigma_{\mathbf{i}} \longrightarrow \alpha_{t(b)}\,h_{\mathbf{i}}\,\mu_{\mathbf{m}} \tag{6.30}$$

and

$$J_{\mathbf{ij}}\,\sigma_{\mathbf{i}}\,\sigma_{\mathbf{j}} \longrightarrow \alpha_{t(b)}\,J_{\mathbf{ij}}\,\mu_{\mathbf{n}}, \tag{6.31}$$

where $\alpha_{t(b)} = \pm 1$ and $\mathbf{n}$ is the nearest-neighbor plaquette to $\mathbf{m}$ that contains the link $\mathbf{j}$. Similarly to the bulk case, pairwise interactions between a qubit at the boundary and another in the bulk

contribute twice to terms containing solely one plaquette variable. As a result,

$$\sum_{\mathbf{i}\in t(b)} h_{\mathbf{i}}\,\sigma_{\mathbf{i}}^{x} + \sum_{\langle \mathbf{i},\mathbf{j}\rangle,\mathbf{i}\in t(b)} J_{\mathbf{ij}}\,\sigma_{\mathbf{i}}^{x}\,\sigma_{\mathbf{j}}^{x} = \alpha_{t(b)} \sum_{\mathbf{m}\in t(b)} \tilde{h}_{\mathbf{m}}\,\mu_{\mathbf{m}}, \tag{6.32}$$

where $\tilde{h}_{\mathbf{m}} = h_{\mathbf{i}} + J_{\mathbf{i'j}} + J_{\mathbf{i''k}}$. Here, $\mathbf{i'}$ and $\mathbf{i''}$ are the next-to-nearest neighboring links to $\mathbf{i}$ along the edge and $\mathbf{j}$ and $\mathbf{k}$ are links belonging to the same plaquette where $\mathbf{i}$ is located [see Fig. 6.3(b)].

Combining Eqs. (6.28), (6.29), and (6.32) we obtain

$$H_{\text{eff}}(\{\mu_{\mathbf{m}}\}) = \sum_{\langle \mathbf{m},\mathbf{n}\rangle} \tilde{h}_{\mathbf{mn}}\,\mu_{\mathbf{m}}\,\mu_{\mathbf{n}} + \sum_{\mathbf{u},\mathbf{v}} \tilde{J}_{\mathbf{u\,v}}\,\mu_{\mathbf{u}}\,\mu_{\mathbf{v}}, \tag{6.33}$$

Thus, we can completely eliminate the qubit variables.

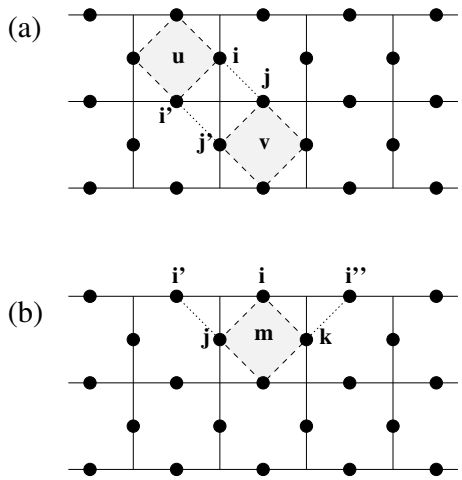

Figure 6.3: (a) Links and plaquettes involved in Eq. (6.27). (b) Links and plaquette involved in Eq. (6.32).

We can now go back to Eqs. (6.24) and (6.25) and switch the restricted sums over qubit variables σ to unrestricted sums over plaquette variables $\{\mu_{\mathbf{m}}\}$. There are two distinct situations to consider, depending on the number of plaquettes in the syndrome.

For syndromes with an even number of plaquettes, the choice of strings in $S^x_{\{p\}}$ will involve no link at the top or bottom boundaries. This is because, in our thermodynamic limit, when the boundaries became infinitely far apart but the plaquettes are confined, this choice provides terms with a finite order in the coupling constants $h_{\mathbf{i}}$ and $J_{\mathbf{ij}}$; other choices will lead to infinite-order terms. Therefore, we can write

$$\mathcal{S}^x_{\{p\}\,\text{even}} \longrightarrow \prod_{\mathbf{m}\in\{p\}} \mu_{\mathbf{m}}. \tag{6.34}$$

and

$$\bar{X}\,\mathcal{S}^x_{\{p\}\ \text{even}} \longrightarrow \alpha_b\,\alpha_t \prod_{\mathbf{m}\in\{p\}} \mu_{\mathbf{m}}, \tag{6.35}$$

since any logic operator $\bar{X}$ will link top to bottom boundaries.

For syndromes with an odd number of plaquettes, at least one string in $S^x_{\{p\}}$ will have to end in one of the boundaries. By applying the operator $\bar{X}$ one generates a string ending on the opposite boundary. Then,

$$\mathcal{S}^x_{\{p\}\ \text{odd}} \longrightarrow \alpha_{t(b)} \prod_{\mathbf{m}\in\{p\}} \mu_{\mathbf{m}}. \tag{6.36}$$

and

$$\bar{X}\,\mathcal{S}^x_{\{p\}\ \text{odd}} \longrightarrow \alpha_{b(t)} \prod_{\mathbf{m}\in\{p\}} \mu_{\mathbf{m}}. \tag{6.37}$$

[If the unpaired plaquette is linked to the top boundary by $\mathcal{S}^x_{\{p\}}$, then one picks the subscript t on the right-hand side of Eq. (6.36). The opposite goes for Eq. (6.37).]

To obtain new expressions for the amplitudes $\mathcal{A}_{\{p\}}$ and $\mathcal{B}_{\{p\}}$ in terms of the variables $\{\mu_{\mathbf{m}}\}$, α_b, and α_t, one inserts Eqs. (6.34) and (6.35) or Eqs. (6.36) and (6.37) into Eqs. (6.24) and (6.25) and sum over all configurations of the variables α_t, α_b, and $\{\mu_{\mathbf{m}}\}$. In order to simplify the result, we

introduce the (unnormalized) correlation function

$$C_{\{p\}}\left(\alpha_b, \alpha_t\right) = \sum_{\{\mu_{\mathbf{m}}\}} \left(\prod_{\mathbf{k}\in\{p\}} \mu_{\mathbf{k}} \right) e^{-\tilde{H}(\{\mu_{\mathbf{m}}\};\alpha_t,\alpha_b)}, \tag{6.38}$$

where

$$\tilde{H}(\{\mu_{\mathbf{m}}\};\alpha_t,\alpha_b) = H_{\text{eff}}(\{\mu_{\mathbf{m}}\}) + H_{\text{bound}}(\{\mu_{\mathbf{m}}\};\alpha_t,\alpha_b), \tag{6.39}$$

and

$$H_{\text{bound}}(\{\mu_{\mathbf{m}}\};\alpha_t,\alpha_b) = \alpha_t \sum_{\mathbf{t}} \tilde{h}_{\mathbf{t}}\, \mu_{\mathbf{t}} + \alpha_b \sum_{\mathbf{b}} \tilde{h}_{\mathbf{b}}\, \mu_{\mathbf{b}}. \tag{6.40}$$

Notice that since H_{eff} contains only two-body interaction terms, the following symmetry relation is satisfied:

$$C_{\{p\}}(-\alpha_t,-\alpha_b) = (-1)^{N_p}\, C_{\{p\}}(\alpha_t,\alpha_b), \tag{6.41}$$

where N_p is the number of plaquettes in $\{p\}$. Using Eqs. (6.34), (6.35), (6.36), and (6.37) in conjunction with Eqs. (6.38) and (6.41) allows us to obtain concise relations for the amplitudes $\mathcal{A}_{\{p\}}$ and $\mathcal{B}_{\{p\}}$. For N_p even, we get

$$\mathcal{A}^{\text{even}}_{\{p\}} = C_{\{p\}}(+,+) + C_{\{p\}}(+,-) \tag{6.42}$$

and

$$\mathcal{B}^{\text{even}}_{\{p\}} = C_{\{p\}}(+,+) - C_{\{p\}}(+,-) \tag{6.43}$$

For N_p odd, there are two situations to consider. When the bottom is closest boundary to the most remote plaquette in $\{p\}$, we get

$$\mathcal{A}^{\text{odd; bottom}}_{\{p\}} = C_{\{p\}}(+,+) - C_{\{p\}}(+,-) \tag{6.44}$$

and

$$\mathcal{B}_{\{p\}}^{\mathrm{odd;\,bottom}} = C_{\{p\}}(+,+) + C_{\{p\}}(+,-) \tag{6.45}$$

while when the closest boundary is the top one,

$$\mathcal{A}_{\{p\}}^{\mathrm{odd;\,top}} = C_{\{p\}}(+,+) + C_{\{p\}}(+,-) \tag{6.46}$$

and

$$\mathcal{B}_{\{p\}}^{\mathrm{odd;\,top}} = C_{\{p\}}(+,+) - C_{\{p\}}(+,-). \tag{6.47}$$

6.10 The threshold as a phase transition

As argued in Sec. 6.7, our prescription of the thermodynamic limit guarantees that $|\mathcal{A}_{\{p\}}| > |\mathcal{B}_{\{p\}}|$ as the lattice size grows and therefore we can use Eq. (6.20) to evaluate the fidelity. Equations (6.42) to (6.47) are exact expressions, valid for any lattice size and for any finite set $\{p\}$, provided that the effective interaction between physical qubits involves only nearest neighbors. Thus, the behavior of $\mathcal{A}_{\{p\}}$ and $\mathcal{B}_{\{p\}}$ is completely determined by $\tilde{H}$ and its associated correlation function $C_{\{p\}}$. Since the boundary-field Ising model defined by $\tilde{H}$ has a finite-temperature critical point, the fidelity threshold can be understood as this phase transition point.

Let us now show that this interpretation is valid. To simplify the argument, suppose that either $\tilde{h} = 0$ and $\tilde{J} \neq 0$ or $\tilde{h} \neq 0$ and $\tilde{J} = 0$, in which case the Ising model defined in Eq. (6.33) can always be transformed into a ferromagnetic model (when $\tilde{J} = 0$) or two decoupled ferromagnetic models (when $\tilde{h} = 0$) by an appropriate change in the signs of the the variables $\mu_{\mathbf{m}}$ belonging to one of the sublattices.

6.10.1 N_p even

Consider the case where N_p is even. For temperatures above the critical value (i.e., for small enough coupling constants), the $\{\mu_{\mathbf{m}}\}$ spin system of Eq. (6.33) is in a disordered (paramagnetic) phase. In the thermodynamic limit, because both boundaries become infinitely distant from the plaquettes in $\{p\}$, $C_{\{p\}}$ will not depend on boundary fields α_b and α_t, namely, $C_{\{p\}}(\alpha_t, \alpha_b) \to \sum_{\{\mu_{\mathbf{m}}\}} \left(\prod_{\mathbf{k}\in\{p\}} \mu_{\mathbf{k}} \right) e^{-H_{\rm eff}(\{\mu_{\mathbf{m}}\})} = C_{\{p\}}(0,0)$. Notice that even though spatial correlations among the spins $\{\mu_{\mathbf{k}}\}$ in the set $\{p\}$ decay exponentially in space, they are finite even in the infinite-lattice limit because their are locked in their positions. Therefore, $|C_{\{p\}}(0,0)| > 0$ and $\mathcal{B}_{\{p\}} \to 0$, independently of $\{p\}$. As a result, $\mathcal{F}_{\{p\}} \to 1$.

Conversely, for low temperatures (i.e., large enough coupling constants), the spin system is in an ordered (ferromagnetic) phase. We can then distinguish two situations: (i) $\alpha_b\, \alpha_t = 1$, when there is an even number of domain walls running parallel to the top and bottom boundaries; (ii) $\alpha_b\, \alpha_t = -1$, when the number of domain walls is odd. In both situations the domain walls are rather costly energetically (the cost scales with $N_{\rm col}$, the number of columns in the lattice). Thus, for low enough temperatures and $N_{\rm col} \gg 1$, we can assume that $C_{\{p\}}(\pm,\pm)$ is governed by spin configurations with no domain wall, whereas $C_{\{p\}}(\pm,\mp)$ is governed by configurations with just one domain wall. In addition, since correlations decay exponentially in space in the ordered phase as well, $\prod_{\mathbf{k}\in\{p\}} \mu_{\mathbf{k}} \approx \prod_{\mathbf{k}\in\{p\}} \mu_{\mathbf{k}}$, where $\cdots = \sum_{\{\mu_{\mathbf{m}}\}} (\cdots)\, e^{-\tilde{H}(\{\mu_{\mathbf{m}}\};\alpha_t,\alpha_b)}$, with each $\mu_{\mathbf{k}} = \pm 1$, depending on which side of the domain wall the site $\mathbf{k}$ is located. Therefore, since we have an even number of plaquettes in $\{p\}$, $C_{\{p\}}(\pm,\pm) > 0$. For $C_{\{p\}}(\pm,\mp)$, on the other hand, because the domain wall can cut across the plaquettes in $\{p\}$ in many different ways with similar energy costs, this amplitude results from a sum of many similar terms with alternating signs. $C_{\{p\}}(\pm,\mp)$ is strongly suppressed with respect to $C_{\{p\}}(\pm,\pm)$ and, as a result, $\mathcal{A}_{\{p\}} \approx \mathcal{B}_{\{p\}}$ and $\mathcal{F}_{\{p\}} \approx \frac{1}{2}$, independently of the location of the plaquettes in the set $\{p\}$, as long as they are in finite number.

6.10.2 N_p odd

Let us now consider cases where N_p is odd and assume that the most remote plaquette in $\{p\}$ is closer to the top boundary (it is straightforward to extend the discussion to the opposite situation).

For temperatures higher than the critical one, the spin system is in a disordered (paramagnetic) phase. In the thermodynamic limit, the bottom boundary will become infinitely distant to the plaquettes in $\{p\}$ and $C_{\{p\}}(\alpha_t, \alpha_b)$ will not depend on the boundary field α_b: $C_{\{p\}}(\alpha_t, \alpha_b) \to C_{\{p\}}(\alpha_t, 0)$. As a result, from Eqs. (6.46) and (6.47) we see that $\mathcal{B}_{\{p\}} \to 0$, independently of $\{p\}$, while $\mathcal{A}_{\{p\}}$ takes a nonzero finite value determined by the residual spatial correlations between the spin variables $\{\mu_{\mathbf{k}}\}_{\mathbf{k}\in\{p\}}$. Therefore, $\mathcal{F}_{\{p\}} \to 1$.

The argument for the low-temperature limit follows closely that developed in Sec. 6.10 when the number of plaquettes is even. In the ordered (ferromagnetic) phase, $C_{\{p\}}(\pm, \pm)$ is governed by spin configurations with no domain walls. Then, $C_{\{p\}}(+, +) > 0$ and $C_{\{p\}}(-, -) > 0$. The correlation functions $C_{\{p\}}(\pm, \mp)$, on the other hand, are dominated by spin configurations with a single domain wall running parallel to the top and bottom boundaries and result from a sum of terms with alternating signs with roughly the same energy costs. As a result, they are suppressed in magnitude in comparison to $C_{\{p\}}(\pm, \pm)$. Thus, using Eqs. (6.46) and (6.47), we concluded that $\mathcal{A}_{\{p\}} \approx \mathcal{B}_{\{p\}}$ and $\mathcal{F}_{\{p\}} \approx \frac{1}{2}$.

6.10.3 *Phase transition*

For both N_p even and odd, the abrupt change in behavior of the correlation function $C_{\{p\}}$ as the critical temperature is crossed is what renders the transition from $\mathcal{F}_{\{p\}} = 1$ to $\mathcal{F}_{\{p\}} = \frac{1}{2}$ sharp and what defines the location of the threshold value for the coupling constants.

We stress that this transition is not the same as that originally discussed in Ref. [23], where the error model was a purely stochastic one with no correlations. By virtue of the stochastic nature of the errors, their problem mapped onto a spin glass on the Nishimori line. Instead, the transition we obtain bares close resemblance to that for the toric code in the presence of a transverse field [107, 108]. For the error model we adopt, if the coupling constants in $\tilde{H}$ are homogeneous, the spin system $\{\mu_{\mathbf{m}}\}$ does not behave as a spin glass.

We now discuss in more detail the critical behavior of the boundary-field Ising model in some special situations and how that behavior affects the surface code threshold.

6.10.4 Homogeneous coupling

Consider $\tilde{J}_{\mathbf{uv}} = 0$ and $\tilde{h}_{\mathbf{mn}} = h < 0$ and real, corresponding to a single-qubit relaxation channel. In this case Eq. (6.33) is reduced to the ferromagnetic square lattice Ising model with a boundary field. In particular, $\mathcal{A}_0$ and $\mathcal{B}_0$ are determined by the partition function of this model [43]. It is known that the free energy has two different terms: a boundary and a bulk contribution. Although the boundary magnetization has a different exponent than the bulk one, the critical temperature for the ferromagnetic transition is defined by the bulk transition temperature [44], $|h_{\text{critical}}| = \ln\left(1+\sqrt{2}\right)/2$. In the high-temperature paramagnetic phase, $|h| < |h_{\text{critical}}|$, the direction of the boundary fields is irrelevant. Hence, in this fully Z_2 symmetric phase, we find that $\mathcal{B}_0 \to 0$ in the thermodynamic limit. Below the critical temperature, $|h| > |h_{\text{critical}}|$, the boundary fields explicitly break the Z_2 symmetry, leading to two distinct values for $\mathcal{B}_0$ when $\alpha_t = \alpha_b$ and $\alpha_t \neq \alpha_b$. In this phase, $\mathcal{B}_0 \neq 0$ in the thermodynamic limit and we find $\mathcal{F}_0 < 1$. The transition is exponentially sharp since the boundary free energy is proportional to the number of sites at the edge. For other syndromes, a very similar discussion can be made.

In the thermodynamic limit, the transition to a regime where the code can correct happens simul-

taneously for all syndromes since the critical point is entirely controlled by $\tilde{H}_{\text{eff}}$.

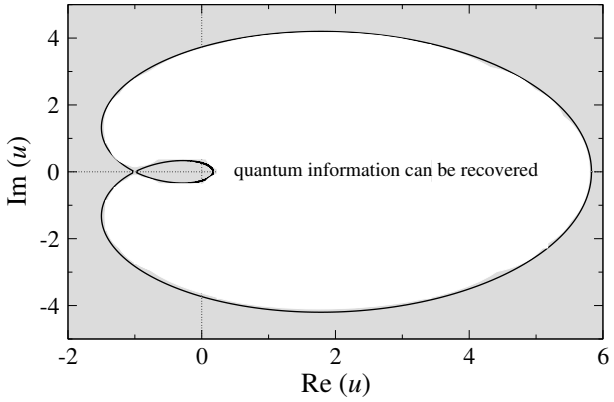

Figure 6.4: Phase diagram of the Ising model with homogeneous complex coupling constant h and its significance to the one-cycle QEC fidelity threshold. Here $u = e^{-4h}$. In the gray regions quantum information cannot be recovered.

This analysis can be extended to complex h [45]. In this more general situation, the transition point between the Z_2 symmetric phase and the broken symmetry phase is defined by the curve $\sinh^2(2h_{\text{critical}}) = e^{-i\theta}$, where $\theta \in [0, 2\pi)$. See Fig. 6.4. For a purely dynamical problem, when h is imaginary (e.g., when a uniform external magnetic field acts on the physical qubits), $h_{\text{critical}} = \pm i\pi/4$. In this case the critical point corresponds to $p_c = 1/2$, which is consistent with the code providing infinite protection in the thermodynamic limit.

Now, consider $\tilde{h}_{\mathbf{mn}} = 0$ and $\tilde{J}_{\mathbf{uv}} = \tilde{J} < 0$. This case applies to qubits coupled linearly to a gapless bosonic bath [66, 93]. The Hamiltonian in Eq. (6.33) can be broken into two independent square-lattice Ising models with nearest-neighbor interactions. Hence, the discussion from the previous paragraph can be immediately applied. Note that $\tilde{J}$ is doubled with respect to its value for the physical qubit interactions, i.e., $\tilde{J} = 2J$.

6.10.5 Random coupling

Let $\tilde{J}_{\mathbf{uv}} = 0$ and $\tilde{h}_{\mathbf{mn}}$ be real and random. The Harris criterion can not be applied since, for the clean Ising model, the specific heat critical exponent vanishes and the model is marginal to disorder [110]. We therefore discuss some specific cases. If $\tilde{h}_{\mathbf{mn}}$ has the same sign for all bonds, we expect bond disorder to be perturbative and simply yield a transition temperature roughly given by the typical value of $\tilde{h}_{\mathbf{mn}}$. This can be put on firm grounds by considering a simple toy model with two possible values for the bond, $\tilde{h}_{\mathbf{mn}} = h_1$ or h_2, with equal probability [46]. In this case the transition temperature is given by $\left(e^{h_1} - 1\right)\left(e^{h_2} - 1\right) = 2$.

An interesting situation arises when there is bond dilution, namely, when some of the $\tilde{h}_{\mathbf{mn}}$ are equal to zero. In the case of a square lattice, the percolation threshold happens when half of the bonds are missing. Thus, if at least half of the qubits do not suffer the action of a local magnetic field $h_{\mathbf{i}}$, the probability of having an infinite cluster (i.e., strings of flipped qubits traversing the lattice) tends to zero in the thermodynamic limit and the Z_2 broken phase does not exist. The implication to QEC is that quantum information can *always* be recovered if at least half of the qubits do not interact with the environment during the QEC cycle. Thus, only a severe random event that affects most of the qubits during the cycle will lead to a failure in the protection. This can be relevant to the design of other planar codes as well (which can be engineered to have high percolation thresholds).

The scenario dramatically changes when we allow bonds with different sign [47]. A Gaussian distribution is likely a realistic assumption for this case [48], but most of the physics can already be discussed using the toy-model bond distribution $P\left(h,q\right) = q\delta\left(\tilde{h}_{\mathbf{mn}} - h\right) + \left(1-q\right)\delta\left(\tilde{h}_{\mathbf{mn}} + h\right)$. There are three renormalization group fixed points for this model in the (h,q) plane [47] (see Fig. 6.5). On top of the well-known Nishimori line, there is an unstable fixed point, (h_N, q_N), that separates the Z_2 broken phase from the unbroken phase. For $q < q_N$ and $h < h_N$ the physics is controlled by the stable fixed point of the model $(h_c, 0)$, hence we fall back to the discussion

of the homogeneous model and get the usual paramagnetic-ferromagnetic transition. Conversely, for $q \geq q_N$ and $h > h_N$ the transition is controlled by the fixed point with (∞, q_N). Little is known about this fixed point, but it is believed that it separates the ferromagnetic phase from a spin glass phase at $h = \infty$. The existence of the Z_2 broken phase is not in question, but the nature of the unbroken phase, where we expect the fidelity to be higher, is not clear and needs further investigation.

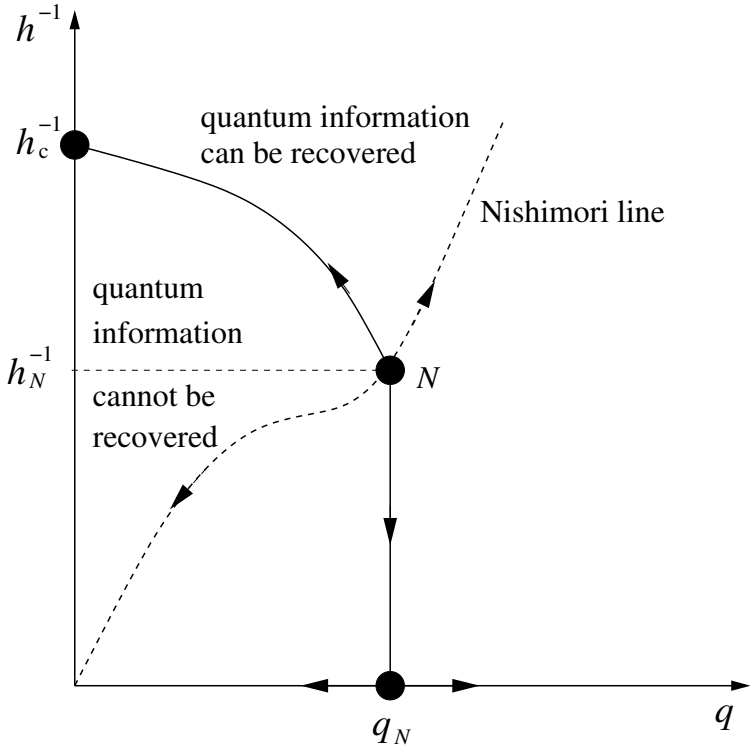

Figure 6.5: Phase diagram of the Ising model with random bond sign and its significance to the one-cycle QEC fidelity threshold.

Finally, let us consider $\tilde{h}_{\mathbf{mn}} = 0$ and $\tilde{J}_{\mathbf{uv}}$ real and random: All the discussion from the previous paragraphs can be immediately transported to this case, the main difference being that there are two independent lattices. Hence, as a function of disorder or coupling strength, one can have two different transition temperatures and thus a more complicated threshold situation may arise.

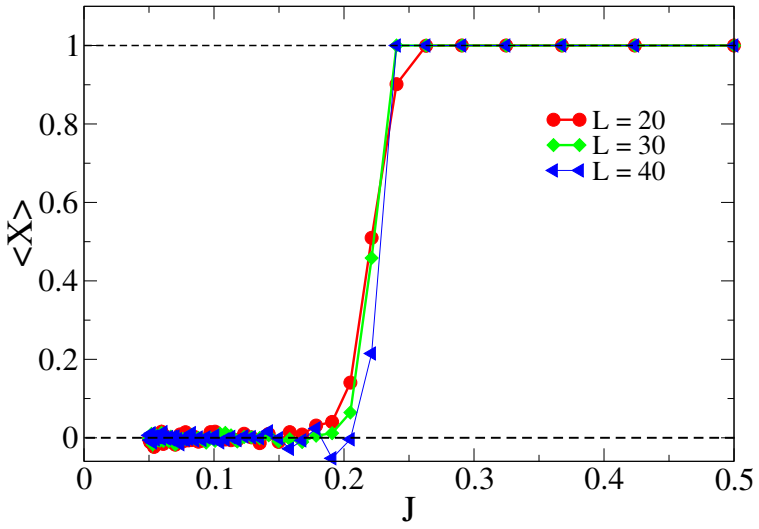

Figure 6.6: Ratio $\langle X \rangle = |\frac{\mathcal{B}}{\mathcal{A}}|$ evaluated through Monte Carlo sampling for three system sizes: $L = 20$ (761 qubits, circles), $L = 30$ (1741 qubits, diamonds), and $L = 40$ (3121 qubits, triangles). The solid lines are guides to the eyes.

6.11 Numerical simulations

Some of the results described above were independently confirmed by Monte Carlo simulations. Here, we present the case of a constant and real $J_{ij} = J$ for nearest neighbors, $h = 0$, and nonerror syndromes. To insert the constraint $A_\diamondsuit = 1$ into the Metropolis algorithm, an alternative representation of the stabilizers was necessary. The stabilizer operator was rewritten as the product of an even number m of logical operators such that their product is equivalent to the stabilizer, namely, $A_\diamondsuit = \bar{Z}_{\Gamma_1} \ldots \bar{Z}_{\Gamma_{2m}}$ (see Ch. 5 for details of this formulation and more extensive numerical results). Working directly with the original spin (i.e., physical qubit) variables, we used this representation to numerically evaluate the amplitudes $\mathcal{A}_0$ and $\mathcal{B}_0$ and the ratio $\langle X \rangle = |\mathcal{B}_0|/|\mathcal{A}_0|$. Data for the case of nearest-neighbor interactions are shown in Fig. 6.6. Notice that the larger the lattice, the sharper the transition becomes. The mapping onto the unconstrained Ising model predicts that the critical coupling J_c should be equal to half of that for a regular two-dimensional Ising system, namely,

$J_c \approx 0.220$. This is in excellent agreement with the numerical value of $J_c = 0.217$ obtained in our Monte Carlo simulations through a finite-size scaling analysis.

6.12 Conclusions

In this chapter, we showed that a stabilizer code, such as the surface code, when coupled to an environment, has an intrinsic fidelity threshold. This threshold can be determined by focusing on the nonerror syndrome sector after the physical qubits have evolved in time under an effective action intermediated by the environment. For other syndrome sectors, the decoding of the syndrome into a recovery operation limits the error correction capabilities of the code. As a result, the effective fidelity threshold should be smaller than the intrinsic threshold. To show that a threshold exists nevertheless for any syndrome, we provide a prescription where the decoding always work in the infinite lattice size limit. When bit-flip errors are considered, this prescription allows us to derive an expression for the fidelity of the surface code in terms of two amplitudes that involve expectation values of a constrained classical spin model.

For the case of an effective action involving at most nearest-neighbor interactions, we map the spin model onto an unconstrained Ising model with boundary fields. This mapping allows us to predict the exact value of the fidelity threshold for several important practical situations. We find that a fidelity threshold is almost always present, for both homogeneous and inhomogeneous noise sources, but the actual critical value of the coupling constant between qubit and environment depends on particular features of the model. Thus, the threshold is not universal. For the case of homogeneous coupling to the environment, the analytical prediction for the threshold location based on the exact mapping is confirmed by an independent Monte-Carlo simulation.

When the effective interaction between physical qubits goes beyond nearest neighbors, the map-

ping no longer works, but the threshold can still be computed by direct numerical simulations of the constrained spin model. In ch. 5 we showed that the threshold decreases with increasing interaction range, as originally predicted in Ref. [66].

APPENDIX A: ONE-DIMENSIONAL SPIN MODEL (DERIVATIONS)

Consider a spin chain of length $N = 4m + 2$ as shown in Fig. 1 in the Letter. The sites are numbered from 1 to N. Sites from 4 to $N - 3$ form the bulk of the chain; sites numbered $1, 2, 3$ and $N - 2, N - 1, N$ are part of the left and right boundaries, respectively. Using this notation, , the unitary transformation R can be written as

$$\begin{aligned} R &= (a + i\,b\,\sigma_1^y\,\sigma_3^y)\,\left(a + i\,b\,\sigma_{N-2}^y\,\sigma_N^y\right)\,\left[\prod_j^{m-1}\left(a + i\,b\,\sigma_{4j}^y\,\sigma_{4j+2}^y\right)\left(a + i\,b\,\sigma_{4j+1}^y\,\sigma_{4j+3}^y\right)\right] \\ &\quad \times \left(a + i\,b\,\sigma_2^y\,\sigma_{N-1}^y\right), \end{aligned} \tag{A.1}$$

where $a = \cos(\alpha/4)$ and $b = \sin(\alpha/4)$. The term within square brackets in Eq. (A.1) is the contribution of the *bulk* while the first two factors are the *boundary* contributions. The last factor in Eq. (A.1) is a *nonlocal* term that connects the two ends of the chain. The initial Ising Hamiltonian can be broken down as

$$\begin{aligned} H_I &= -J\sum_{i=1}^{m-1}\left(\sigma_{4i}^z\,\sigma_{4i+1}^z + \sigma_{4i+1}^z\,\sigma_{4i+2}^z + \sigma_{4i+2}^z\,\sigma_{4i+3}^z\right) - J\sum_{i=0}^{m-1}\sigma_{4i+3}^z\,\sigma_{4i+4}^z \\ &\quad - J\,\left(\sigma_1^z\,\sigma_2^z + \sigma_2^z\,\sigma_3^z + \sigma_{N-2}^z\,\sigma_{N-1}^z + \sigma_{N-1}^z\sigma_N^z\right). \end{aligned} \tag{A.2}$$

Let us first consider the transformation of the terms within the parenthesis in the first line of of Eq. (A.2). For each of the three terms, there exists one and only one term in the *bulk* [corresponding to a term within the square brackets in Eq.(A.1)] that anticommutes with it. Thus,

$$\begin{aligned} R\,\left(\sigma_{4i}^z\,\sigma_{4i+1}^z\right)\,R^\dagger &= \left(a + i\,b\,\sigma_{4j+1}^y\,\sigma_{4j+3}^y\right)\left(c\,\sigma_{4i}^z\,\sigma_{4i+1}^z + s\,\sigma_{4i}^x\,\sigma_{4i+1}^z\sigma_{4i+2}^y\right)\left(a - i\,b\,\sigma_{4j+1}^y\,\sigma_{4j+3}^y\right) \\ &= c^2\,\sigma_{4i}^z\,\sigma_{4i+1}^z + s\,c\,\left(\sigma_{4i}^z\,\sigma_{4i+1}^x\,\sigma_{4i+3}^y + \sigma_{4i}^x\,\sigma_{4i+1}^z\,\sigma_{4i+2}^y\right) \\ &\quad + s^2\,\sigma_{4i}^x\,\sigma_{4i+1}^x\,\sigma_{4i+2}^y\,\sigma_{4i+3}^y, \end{aligned} \tag{A.3}$$

where we have introduced $c = a^2 - b^2 = \cos(\alpha/2)$ and $s = 2ab = \sin(\alpha/2)$. Similarly,

$$\begin{aligned} R\left(\sigma^z_{4i+1}\,\sigma^z_{4i+2}\right)R^\dagger &= \left(a + i\,b\,\sigma^y_{4j+1}\,\sigma^y_{4j+3}\right)\left(c\,\sigma^z_{4i+1}\,\sigma^z_{4i+2} + s\,\sigma^y_{4i}\,\sigma^z_{4i+1}\,\sigma^x_{4i+2}\right) \\ &\quad \times \left(a - i\,b\,\sigma^y_{4j+1}\,\sigma^y_{4j+3}\right) \qquad \text{(A.4)} \\ &= c^2\sigma^z_{4i+1}\sigma^z_{4i+2} + s\,c\,\left(\sigma^x_{4i+1}\,\sigma^z_{4i+2}\,\sigma^y_{4i+3} + \sigma^y_{4i}\,\sigma^z_{4i+1}\,\sigma^y_{4i+2}\right) \\ &\quad + s^2\,\sigma^y_{4i}\,\sigma^x_{4i+1}\,\sigma^x_{4i+2}\sigma^y_{4i+3}, \qquad \text{(A.5)} \end{aligned}$$

and

$$\begin{aligned} R(\sigma^z_{4i+2}\,\sigma^z_{4i+3})R^\dagger &= \left(a + i\,b\,\sigma^y_{4j+1}\,\sigma^y_{4j+3}\right)\left(c\,\sigma^z_{4i+2}\,\sigma^z_{4i+3} + s\,\sigma^y_{4i}\,\sigma^x_{4i+2}\,\sigma^z_{4i+3}\right) \\ &\quad \times \left(a - i\,b\,\sigma^y_{4j+1}\,\sigma^y_{4j+3}\right) \qquad \text{(A.6)} \\ &= c^2\sigma^z_{4i+2}\,\sigma^z_{4i+3} + s\,c\,\left(\sigma^y_{4i+1}\,\sigma^z_{4i+2}\,\sigma^x_{4i+3} + \sigma^y_{4i}\,\sigma^x_{4i+2}\,\sigma^z_{4i+3}\right) \\ &\quad + s^2\,\sigma^y_{4i}\,\sigma^y_{4i+1}\,\sigma^x_{4i+2}\,\sigma^x_{4i+3}. \qquad \text{(A.7)} \end{aligned}$$

The second term in the first line in Eq. (A.2) contains terms such as $\sigma^z_3\,\sigma^z_4$, $\sigma^z_7\,\sigma^z_8$, up to $\sigma^z_{N-3}\,\sigma^z_{N-2}$. They transform as

$$\begin{aligned} R\,\left(\sigma^z_{4i+3}\,\sigma^z_{4i+4}\right)\,R^\dagger &= \left(a + i\,b\,\sigma^y_{4i+1}\,\sigma^y_{4i+3}\right)\left(c\,\sigma^z_{4i+3}\,\sigma^z_{4i+4} + s\,\sigma^y_{4i+3}\,\sigma^x_{4i+4}\,\sigma^z_{4i+6}\right) \\ &\quad \times \left(a - i\,b\,\sigma^y_{4i+1}\,\sigma^y_{4i+3}\right) \qquad \text{(A.8)} \\ &= c^2\,\sigma^z_{4i+3}\,\sigma^z_{4i+4} + s\,c\,\left(\sigma^y_{4i+1}\,\sigma^x_{4i+3}\,\sigma^z_{4i+4} + \sigma^z_{4i+3}\sigma^x_{4i+4}\,\sigma^y_{4i+6}\right) \\ &\quad + s^2\,\sigma^y_{4i+1}\,\sigma^x_{4i+3}\,\sigma^x_{4i+4}\,\sigma^y_{4i+6}. \qquad \text{(A.9)} \end{aligned}$$

Finally, for the terms $\sigma^z_1\sigma^z_2$, $\sigma^z_2\sigma^z_3$, $\sigma^z_{N-2}\sigma^z_{N-1}$, and $\sigma^z_{N-1}\sigma^z_N$ in Eq. (A.2), the transformation leads

to the nonlocal terms. We obtain

$$
\begin{aligned}
R\left(\sigma_1^z\,\sigma_2^z\right)R^\dagger &= c^2\,\sigma_1^z\,\sigma_2^z + cs\left(\sigma_1^z\,\sigma_2^x\,\sigma_{N-1}^y + \sigma_1^x\,\sigma_2^z\,\sigma_3^y\right) + s^2\,\sigma_1^x\,\sigma_2^x\,\sigma_3^y\,\sigma_{N-1}^y \quad \text{(A.10)}\\
R\left(\sigma_{N-1}^z\,\sigma_N^z\right)R^\dagger &= c^2\,\sigma_{N-1}^z\,\sigma_N^z + cs\left(\sigma_2^y\,\sigma_{N-1}^x\,\sigma_N^z + \sigma_{N-2}^y\,\sigma_{N-1}^z\,\sigma_N^x\right)\\
&\quad + s^2\,\sigma_2^y\,\sigma_{N-2}^y\,\sigma_{N-1}^x\sigma_N^x \quad \text{(A.11)}\\
R\left(\sigma_2^z\,\sigma_3^z\right)R^\dagger &= c^2\,\sigma_2^z\,\sigma_3^z + cs\left(\sigma_2^x\,\sigma_3^z\,\sigma_{N-1}^y + \sigma_1^y\,\sigma_2^z\,\sigma_3^x\right) + s^2\,\sigma_1^y\,\sigma_2^x\,\sigma_3^x\sigma_{N-1}^y \quad \text{(A.12)}\\
R\left(\sigma_{N-2}^z\,\sigma_{N-1}^z\right)R^\dagger &= c^2\,\sigma_{N-2}^z\,\sigma_{N-1}^z + cs\left(\sigma_2^y\,\sigma_{N-2}^z\,\sigma_{N-1}^x + \sigma_{N-2}^x\,\sigma_{N-1}^z\,\sigma_N^y\right)\\
&\quad + s^2\,\sigma_2^y\,\sigma_{N-2}^x\,\sigma_{N-1}^x\,\sigma_N^y. \quad \text{(A.13)}
\end{aligned}
$$

Putting all together, we obtain Eq. (4) in the Letter, where

$$
\begin{aligned}
H_T &= -J\sum_{i=1}^{m-1}\left(\sigma_{4i}^y\,\sigma_{4i+1}^x\,\sigma_{4i+2}^x\sigma_{4i+3}^y + \sigma_{4i}^y\,\sigma_{4i+1}^x\,\sigma_{4i+2}^x\sigma_{4i+3}^y + \sigma_{4i}^y\,\sigma_{4i+1}^y\,\sigma_{4i+2}^x\,\sigma_{4i+3}^x\right)\\
&\quad - J\sum_{i=0}^{m-1}\sigma_{4i+1}^y\,\sigma_{4i+3}^x\,\sigma_{4i+4}^x\,\sigma_{4i+6}^y\\
&\quad - J\left(\sigma_1^x\,\sigma_2^x\,\sigma_3^y\,\sigma_{N-1}^y + \sigma_2^y\,\sigma_{N-2}^y\,\sigma_{N-1}^x\sigma_N^x + \sigma_1^y\,\sigma_2^x\,\sigma_3^x\sigma_{N-1}^y + \sigma_2^y\,\sigma_{N-2}^x\,\sigma_{N-1}^x\,\sigma_N^y\right)
\end{aligned}
\quad \text{(A.14)}
$$

and

$$
\begin{aligned}
H_1 &= -J\sum_{i=1}^{m-1}\left(\sigma_{4i}^z\,\sigma_{4i+1}^x\,\sigma_{4i+3}^y + \sigma_{4i}^x\,\sigma_{4i+1}^z\,\sigma_{4i+2}^y + \sigma_{4i+1}^x\,\sigma_{4i+2}^z\,\sigma_{4i+3}^y + \sigma_{4i}^y\,\sigma_{4i+1}^z\,\sigma_{4i+2}^y\right.\\
&\quad \left. + \sigma_{4i+1}^y\,\sigma_{4i+2}^z\,\sigma_{4i+3}^x + \sigma_{4i}^y\,\sigma_{4i+2}^x\,\sigma_{4i+3}^z\right) - J\sum_{i=0}^{m-1}\left(\sigma_{4i+1}^y\,\sigma_{4i+3}^x\,\sigma_{4i+4}^z + \sigma_{4i+3}^z\sigma_{4i+4}^x\,\sigma_{4i+6}^y\right)\\
&\quad - J\left(\sigma_1^z\,\sigma_2^x\,\sigma_{N-1}^y + \sigma_1^x\,\sigma_2^z\,\sigma_3^y + \sigma_2^y\,\sigma_{N-1}^x\,\sigma_N^z + \sigma_{N-2}^y\,\sigma_{N-1}^z\,\sigma_N^x + \sigma_2^x\,\sigma_3^z\,\sigma_{N-1}^y\right.\\
&\quad \left. + \sigma_1^y\,\sigma_2^z\,\sigma_3^x + \sigma_2^y\,\sigma_{N-2}^z\,\sigma_{N-1}^x + \sigma_{N-2}^x\,\sigma_{N-1}^z\,\sigma_N^y\right).
\end{aligned}
\quad \text{(A.15)}
$$

Notice that H_T can be broken into four-spin plaquette operators, as stated in Eq. (5) of the paper. The operators are explicitly identified in Eqs. (2.10-2.17).

APPENDIX B: EVOLUTION OPERATOR

Consider Eq. (4.14), where the bosonic field in the interaction picture reads

$$f(\mathbf{r},t) = \frac{(v/\omega_0)^{D/2+s}}{L^{D/2}} \sum_{\mathbf{k}\neq 0} |\mathbf{k}|^s \left(e^{i\mathbf{k}\cdot\mathbf{r}-i|\mathbf{k}|vt} a_{\mathbf{k}}^\dagger + e^{-i\mathbf{k}\cdot`\mathbf{r}+i|\mathbf{k}|vt} a_{\mathbf{k}} \right). \tag{B.1}$$

We can write $U(\Delta) = \exp[\Omega(\Delta)]$, where $\Omega(\Delta)$ follows the Magnun expansion

$$\Omega(\Delta) = \Omega_1(\Delta) + \Omega_2(\Delta) + \Omega_3(\Delta) + \ldots \tag{B.2}$$

with

$$\Omega_1(\Delta) = -\frac{i\lambda}{2} \int_0^\Delta dt \sum_i f(\mathbf{r}_i,t)\, \sigma_i^x, \tag{B.3}$$

$$\Omega_2(\Delta) = -\frac{1}{2!}\left(\frac{\lambda}{2}\right)^2 \int_0^\Delta dt_1 \int_0^{t_1} dt_2 \times \sum_{i,j} [f(\mathbf{r}_i,t_1), f(\mathbf{r}_j,t_2)]\, \sigma_i^x \sigma_j^x, \tag{B.4}$$

$$\begin{aligned}\Omega_3(\Delta) = & -\frac{i}{3!}\left(\frac{\lambda}{2}\right)^3 \int_0^\Delta dt_1 \int_0^{t_1} dt_2 \int_0^{t_2} dt_3 \\ & \times \sum_{i,j,k} \big([f(\mathbf{r}_i,t_1), [f(\mathbf{r}_j,t_2), f(\mathbf{r}_k,t_3)]] \\ & + [f(\mathbf{r}_k,t_3), [f(\mathbf{r}_j,t_2), f(\mathbf{r}_i,t_1)]] \big) \\ & \times \sigma_i^x \sigma_j^x \sigma_k^x,\end{aligned} \tag{B.5}$$

etc. Since $[f(\mathbf{r}_i,t_1), f(\mathbf{r}_j,t_2)]$ is a c-number, only the first two terms in the expansion survive and

we can write

$$U(\Delta) = \exp\left[-i\frac{\lambda}{2}\sum_i F_{\mathbf{r}_i}(\Delta)\sigma_i^x\right] \times \exp\left[-\frac{\lambda^2}{8}\sum_{i,j}\mathcal{G}^{(I)}_{\mathbf{r}_i\mathbf{r}_j}(\Delta)\sigma_i^x\sigma_j^x\right]. \tag{B.6}$$

where $\mathcal{G}^{(I)}_{\mathbf{r}_i\mathbf{r}_j}(\Delta)$ and $F_{\mathbf{r}_i}(\Delta)$ are defined in Eqs. (4.18) and (4.20), respectively.

It is convenient to rewrite the first exponential in Eq. (B.6) as a normal ordered term. For this purpose, we note that $F_{\mathbf{r}_i}(\Delta)$ has the form

$$F_{\mathbf{r}_i}(\Delta) = \sum_{k\neq 0}(g^*_{\mathbf{r}_i,\mathbf{k}}\, a_{\mathbf{k}} + g_{\mathbf{r}_i,\mathbf{k}}\, a^\dagger_{\mathbf{k}}), \tag{B.7}$$

where

$$g_{\mathbf{r},\mathbf{k}} = -i\frac{(v/\omega_0)^{D/2+s}}{vL^{D/2}}|\mathbf{k}|^{s-1}e^{i\mathbf{k}\cdot\mathbf{r}}(e^{i|\mathbf{k}|v\Delta}-1). \tag{B.8}$$

Thus, we can write

$$\exp\left[-\frac{i\lambda}{2}\sum_i F_{\mathbf{r}_i}(\Delta)\sigma_i^x\right] = \prod_{\mathbf{k}\neq 0}\exp(a^\dagger_{\mathbf{k}}v_{\mathbf{k}} - a_{\mathbf{k}}v^\dagger_{\mathbf{k}}), \tag{B.9}$$

where

$$v_{\mathbf{k}} = -\frac{i\lambda}{2}\sum_i g_{\mathbf{r}_i,\mathbf{k}}\,\sigma_i^x. \tag{B.10}$$

Now we can use the Zassenhaus formula applied to bosonic operators,

$$e^{(a^\dagger_{\mathbf{k}}v_{\mathbf{k}} - a_{\mathbf{k}}v^*_{\mathbf{k}})} = e^{\frac{1}{2}[a^\dagger_{\mathbf{k}}v_{\mathbf{k}}, a_{\mathbf{k}}v^\dagger_{\mathbf{k}}]}\, e^{a^\dagger_{\mathbf{k}}v_{\mathbf{k}}}\, e^{-a_{\mathbf{k}}v^\dagger_{\mathbf{k}}}, \tag{B.11}$$

which results in

$$\begin{aligned}
\exp\left[-i\lambda\sum_i F_{\mathbf{r}_i}(\Delta)\,\sigma_i^x\right] &= \prod_{\mathbf{k}\neq 0} e^{-\frac{1}{2}v_{\mathbf{k}}v_{\mathbf{k}}^\dagger}\, e^{a_{\mathbf{k}}^\dagger v_{\mathbf{k}}}\, e^{-a_{\mathbf{k}}v_{\mathbf{k}}^\dagger} \\
&= \prod_{\mathbf{k}\neq 0} e^{-\frac{1}{2}v_{\mathbf{k}}v_{\mathbf{k}}^\dagger} : e^{a_{\mathbf{k}}^\dagger v_{\mathbf{k}} - a_{\mathbf{k}}v_{\mathbf{k}}^\dagger} : \\
&= e^{-\frac{1}{2}\sum_{\mathbf{k}\neq 0} v_{\mathbf{k}}v_{\mathbf{k}}^\dagger} \\
&\quad \times : \exp\left[-i\frac{\lambda}{2}\sum_i F_{\mathbf{r}_i}(\Delta)\,\sigma_i^x\right] :, \qquad \text{(B.12)}
\end{aligned}$$

where $: (\ldots) :$ denotes normal ordering. We can rewrite the argument of the first exponential in Eq. (B.12) since

$$\begin{aligned}
\sum_{\mathbf{k}\neq 0} v_{\mathbf{k}}v_{\mathbf{k}}^\dagger &= -\frac{\lambda^2}{4}\sum_{i,j}\left(\sum_{\mathbf{k}\neq 0} g_{\mathbf{r}_i,\mathbf{k}}g^*_{\mathbf{r}_j,\mathbf{k}}\right)\sigma_i^x\sigma_j^x \\
&= -\frac{\lambda^2}{4}\sum_{i,j}\mathcal{G}^{(R)}_{\mathbf{r}_i\mathbf{r}_j}(\Delta)\,\sigma_i^x\sigma_j^x, \qquad \text{(B.13)}
\end{aligned}$$

where $\mathcal{G}^{(R)}_{\mathbf{r}_i\mathbf{r}_j}(\Delta)$ is defined in Eq. (4.19). Combining Eqs. (B.6), (B.12), and (B.13), we arrive at Eq. (4.15).

APPENDIX C: THE CORRELATOR $\mathcal{G}^{(R)}_{\mathbf{rs}}(\Delta)$

The correlator in Eq. (4.19) can be evaluated in the following way. Inserting Eq. (4.20) into Eq. (4.19) and using Eq. (B.1), we find

$$\mathcal{G}^{(R)}_{\mathbf{rs}}(\Delta) = \frac{(v/\omega_0)^{D+2s}}{v^2 L^D} \sum_{\mathbf{k}\neq 0} |\mathbf{k}|^{2s-2} e^{i\mathbf{k}\cdot(\mathbf{r}-\mathbf{s})} \left| e^{i|\mathbf{k}|v\Delta} - 1 \right|^2 . \tag{C.1}$$

This is integral is convergent provided that $0 < D + 2s < 4$. Assuming $D = 2$, we can write

$$\begin{aligned} \mathcal{G}^{(R)}_{\mathbf{rs}}(\Delta) &= \frac{2(v/\omega_0)^{2+2s}}{v^2} \int \frac{d^2k}{(2\pi)^2} |\mathbf{k}|^{2s-2} e^{i\mathbf{k}\cdot(\mathbf{r}-\mathbf{s})} \\ &\quad \times \left[1 - \cos\left(|\mathbf{k}|v\Delta\right)\right] \\ &= \frac{(v/\omega_0)^{2+2s}}{\pi\, v^2} \int_0^{\Lambda} dk\, k^{2s-1} J_0\left(k|\mathbf{r}-\mathbf{s}|\right) \\ &\quad \times \left[1 - \cos\left(kv\Delta\right)\right], \end{aligned} \tag{C.2}$$

where $J_n(x)$ is the nth Bessel function of the first kind. To proceed further, we consider three representative values of s where the integration over momentum is convergent independent of the cutoff and we can set $\Lambda \to \infty$.

- Subohmic case:

  For $s = -1/2$ we can write

$$\mathcal{G}^{(R)}_{\mathbf{rs}}(\Delta) = \frac{1}{\pi\, v\, \omega_0} \int_0^{\infty} \frac{dk}{k^2} J_0\left(k|\mathbf{r}-\mathbf{s}|\right) \left[1 - \cos\left(kv\Delta\right)\right]. \tag{C.3}$$

  Then, Eq. (4.21) can be obtained by using the integral [76]

$$\begin{aligned} &\int_0^{\infty} \frac{dx}{x^2} J_0(\beta x) \left[1 - \cos(\alpha x)\right] \\ &= -\beta + \begin{cases} \sqrt{\beta^2 - \alpha^2} + \alpha \arcsin\left(\frac{\alpha}{\beta}\right), & \alpha < \beta, \\ \frac{\alpha\,\pi}{2}, & \alpha > \beta. \end{cases} \end{aligned} \tag{C.4}$$

- Ohmic case:

  For $s = 0$ we can write

$$\mathcal{G}^{(R)}_{\mathbf{rs}}(\Delta) = \frac{1}{\pi\,\omega_0^2}\int_0^\infty \frac{dk}{k}\,J_0\left(k|\mathbf{r}-\mathbf{s}|\right)\left[1-\cos\left(kv\Delta\right)\right]. \tag{C.5}$$

  Then, Eq. (4.23) can be obtained by using the integral [77]

$$\int_0^\infty \frac{dx}{x} J_0(\beta x)\left[1-\cos(\alpha x)\right] = \text{arcosh}\left(\frac{\alpha}{\beta}\right)\,\theta(\alpha-\beta). \tag{C.6}$$

- Superohmic case:

  For $s = 1/2$ we can write

$$\mathcal{G}^{(R)}_{\mathbf{rs}}(\Delta) = \frac{v}{\pi\,\omega_0^3}\int_0^\infty dk\,J_0\left(k|\mathbf{r}-\mathbf{s}|\right)\left[1-\cos\left(kv\Delta\right)\right]. \tag{C.7}$$

  Then, Eq. (4.25) can be obtained by using the integral [78]

$$\int_0^\infty dx\,J_0(\beta x)\,\left[1-\cos(\alpha x)\right] = \frac{1}{\beta} - \frac{\theta(\beta-\alpha)}{\sqrt{\beta^2-\alpha^2}}. \tag{C.8}$$

APPENDIX D: THE CORRELATOR $\mathcal{G}^{(I)}_{\mathbf{rs}}(\Delta)$

The correlator in Eq. (4.18) can be evaluated in the following way. Starting with Eq. (4.13), we have

$$[f(\mathbf{r},t_1),f(\mathbf{s},t_2)] = -2i\frac{(v/\omega_0)^{D+2s}}{L^D}\sum_{\mathbf{k}\neq 0}|\mathbf{k}|^{2s}\sin[\mathbf{k}\cdot(\mathbf{r}-\mathbf{s})+|\mathbf{k}|v(t_1-t_2)], \tag{D.1}$$

which allows us to write

$$\frac{1}{2}\left\{[f(\mathbf{r},t_1),f(\mathbf{s},t_2)]+[f(\mathbf{s},t_1),f(\mathbf{r},t_2)]\right\} = -2i\frac{(v/\omega_0)^{D+2s}}{L^D}\sum_{\mathbf{k}\neq 0}|\mathbf{k}|^{2s}\cos[\mathbf{k}\cdot(\mathbf{r}-\mathbf{s})]\sin[|\mathbf{k}|v(t_1-t_2)]. \tag{D.2}$$

Considering $D=2$, we have

$$\frac{1}{2}\left\{[f(\mathbf{r},t_1),f(\mathbf{s},t_2)]+[f(\mathbf{s},t_1),f(\mathbf{r},t_2)]\right\} = -\frac{i}{\pi}\left(\frac{v}{\omega_0}\right)^{2+2s}\int_0^\Lambda dk\,k^{2s+1}J_0(k|\mathbf{r}-\mathbf{s}|)\sin[kv(t_1-t_2)]. \tag{D.3}$$

In Eq. (D.3), we introduced an ultraviolet momentum cutoff Λ. To proceed further, we need to specify s. Below, we consider three representative values.

- Subohmic case:

  For $s=-1/2$, the integral in Eq. (D.3) converges. Using the integral [79]

  $$\int_0^\infty dx\,J_0(\beta x)\,\sin(\alpha x) = \text{sign}(\alpha)\,\frac{\theta(|\alpha|-|\beta|)}{\sqrt{\alpha^2-\beta^2}}, \tag{D.4}$$

  we have

  $$\frac{1}{2}\left\{[f(\mathbf{r},t_1),f(\mathbf{s},t_2)]+[f(\mathbf{s},t_1),f(\mathbf{r},t_2)]\right\} = -\frac{i}{\pi}\left(\frac{v}{\omega_0}\right)\text{sign}(t_1-t_2)\,\frac{\theta(v|t_1-t_2|-|\mathbf{r}-\mathbf{s}|)}{\sqrt{v^2|t_1-t_2|^2-|\mathbf{r}-\mathbf{s}|^2}}. \tag{D.5}$$

  Carrying out the time-ordered integration over t_1 and t_2, we obtain Eq. (4.22).

- Ohmic case:

  For $s = 0$, we notice that

$$\frac{1}{2}\left\{[f(\mathbf{r},t_1),f(\mathbf{s},t_2)]+[f(\mathbf{s},t_1),f(\mathbf{r},t_2)]\right\} = -\frac{i}{\pi}\left(\frac{v}{\omega_0}\right)^2\frac{d}{dt_2}\frac{d}{dt_1} \left[\int_0^\Lambda \frac{dk}{k}\,J_0(k|\mathbf{r}-\mathbf{s}|)\sin[kv(t_1-t_2)]\right]. \tag{D.6}$$

  Using the integral [80]

$$\int_0^\infty \frac{dx}{x}\,J_0(\beta x)\,\sin(\alpha x) = \text{sign}(\alpha)\left[\frac{\pi}{2}\,\theta(|\alpha|-|\beta|)+\arcsin\left(\frac{|\alpha|}{|\beta|}\right)\,\theta(|\beta|-|\alpha|)\right] \tag{D.7}$$

  we obtain

$$\frac{1}{2}\left\{[f(\mathbf{r},t_1),f(\mathbf{s},t_2)]+[f(\mathbf{s},t_1),f(\mathbf{r},t_2)]\right\} = -\frac{i}{\pi}\left(\frac{v}{\omega_0}\right)^2\frac{d}{dt_2}\frac{d}{dt_1}\left[\frac{\pi}{2}\,\theta(|t_1-t_2|-|\mathbf{r}-\mathbf{s}|) + \arcsin\left(\frac{|t_1-t_2|}{|\mathbf{r}-\mathbf{s}|}\right)\,\theta(|\mathbf{r}-\mathbf{s}|-|t_1-t_2|)\right]. \tag{D.8}$$

  Carrying out the time-ordered integration in t_1 and t_2, we obtain Eq. (4.24).

- Superohmic case:

  Similarly to the ohmic case, for $s = 1/2$ we write

$$\frac{1}{2}\left\{[f(\mathbf{r},t_1),f(\mathbf{s},t_2)]+[f(\mathbf{s},t_1),f(\mathbf{r},t_2)]\right\} = -\frac{i}{\pi}\left(\frac{v}{\omega_0}\right)^3\frac{d}{dt_2}\frac{d}{dt_1} \left[\int_0^\Lambda dk\,J_0(k|\mathbf{r}-\mathbf{s}|)\sin[kv(t_1-t_2)]\right]. \tag{D.9}$$

Using the integral in Eq. (D.4), we obtain

$$\frac{1}{2}\left\{[f(\mathbf{r},t_1),f(\mathbf{s},t_2)]+[f(\mathbf{s},t_1),f(\mathbf{r},t_2)]\right\} \;=\; -\frac{i}{\pi}\left(\frac{v}{\omega_0}\right)^3\frac{d}{dt_2}\frac{d}{dt_1}\left[\frac{\theta(|t_1-t_2|-|\mathbf{r}-\mathbf{s}|)}{\sqrt{v^2|t_1-t_2|^2-|\mathbf{r}-\mathbf{s}|^2}}\right]. \tag{D.10}$$

Carrying out the integration the time-ordered integrations on t_1 and t_2, we arrive at Eq. (4.26).

APPENDIX E: SINGLE-QUBIT FLIPPING PROBABILITY

We can obtain a compact expression for the single-qubit-bath evolution operator in Eq. (4.58) by following essentially the same steps show in Appendix B. The only formal difference is that summations over all qubits in the lattice have to be replaced by a term corresponding to a single qubit j. Thus, considering Eq. (4.15), the result is

$$U_j(\Delta) = \chi_j \; : \exp\left[-\frac{i\lambda}{2} F_{\mathbf{r}_j}(\Delta)\, \sigma_j^x\right] :, \tag{E.1}$$

where

$$\chi_j = \exp\left[-\frac{\lambda^2}{8} \mathcal{G}^{(R)}_{\mathbf{r}_j \mathbf{r}_j}(\Delta)\right]. \tag{E.2}$$

since $\mathcal{G}^{(I)}_{\mathbf{r}_j \mathbf{r}_j}(\Delta) = 0$.

Consider now the change of basis

$$|\uparrow_j\rangle = \frac{1}{\sqrt{2}} \left(|\uparrow_j\rangle_x + |\downarrow_j\rangle_x\right), \tag{E.3}$$

$$|\downarrow_j\rangle = \frac{1}{\sqrt{2}} \left(|\uparrow_j\rangle_x - |\downarrow_j\rangle_x\right), \tag{E.4}$$

which allows one to write

$$\begin{aligned} \langle\uparrow_j |U_j(\Delta)| \downarrow_j\rangle &= \frac{1}{2}\left\{\exp\left[-\frac{i\lambda}{2} F_{\mathbf{r}_j}(\Delta)\right]\right. \\ &\quad \left. - \exp\left[\frac{i\lambda}{2} F_{\mathbf{r}_j}(\Delta)\right]\right\} \end{aligned} \tag{E.5}$$

since $: e^{-\frac{i\lambda}{2} F_{\mathbf{r}_j}(\Delta)} := \chi_j^{-1}\, e^{-\frac{i\lambda}{2} F_{\mathbf{r}_j}(\Delta)}$ [see Eqs. (B.12) and (B.13)]. We can then write

$$\begin{aligned} \langle\uparrow_j |U_j^\dagger(\Delta)| \downarrow_j\rangle\langle\downarrow_j |U_j(\Delta)| \uparrow_j\rangle &= \frac{1}{4}\left\{2 - \exp\left[i\lambda\, F_{\mathbf{r}_j}(\Delta)\right] - \exp\left[-i\lambda\, F_{\mathbf{r}_j}(\Delta)\right]\right\} \\ &= \frac{1}{4}\left\{2 - \chi_j^2 : \exp\left[i\lambda\, F_{\mathbf{r}_j}(\Delta)\right] : - \chi_j^2 : \exp\left[-i\lambda\, F_{\mathbf{r}_j}(\Delta)\right] :\right\}, \end{aligned} \tag{E.6}$$

which yields Eq. (4.59) when the expectation value over the bath vacuum is taken. Now we can insert Eq. (E.1) into Eq. (4.57) to obtain Eq. (4.59).

APPENDIX F: EXISTANCE OF AN INTRINSIC THRESHOLD

Let us consider the case of nonerror syndrome and assume that the environment is reset to its ground state at the end of the QEC cycle. The final state of the physical qubits is given by the state vector

$$|\psi_{\rm QEC}\rangle_0 = \mathcal{P}_0\, U_{\rm eff}|\bar{\uparrow}\rangle, \tag{F.1}$$

where

$$|\bar{\uparrow}\rangle = \frac{1}{\sqrt{2^{N_\diamond}}}\prod_{\Diamond}(1+A_\Diamond)|F_z\rangle, \tag{F.2}$$

$|F_z\rangle$ is the ferromagnetic z state, and the projector of positive stars and plaquettes is

$$\mathcal{P}_0 = \frac{1}{2^{N_\diamond}2^{N_\square}}\prod_{\Diamond}(1+A_\Diamond)\prod_{\square}(1+B_\square). \tag{F.3}$$

Since "no errors" were identified, there is no need to apply a recovery operation: $\mathcal{S}_0^x = 1$ (i.e., the identity operator).

Introducing the amplitudes

$$\begin{aligned}\mathcal{A}_0 &= \langle\bar{\uparrow}|\psi_{\rm QEC}\rangle_0 \\ &= \frac{1}{2^{N_\diamond}2^{N_\square}}\langle\bar{\uparrow}|\prod_{\Diamond}(1+A_\Diamond)\prod_{\square}(1+B_\square)U_{\rm eff}|\bar{\uparrow}\rangle\end{aligned} \tag{F.4}$$

and

$$\begin{aligned}\mathcal{B}_0 &= \langle\bar{\downarrow}|\psi_{\rm QEC}\rangle_0 \\ &= \frac{1}{2^{N_\diamond}2^{N_\square}}\langle\bar{\uparrow}|\bar{X}\prod_{\Diamond}(1+A_\Diamond)\prod_{\square}(1+B_\square)U_{\rm eff}|\bar{\uparrow}\rangle,\end{aligned} \tag{F.5}$$

we can express the fidelity without any ambiguity as

$$\mathcal{F}_0 = \frac{|\mathcal{A}_0|^2}{|\mathcal{A}_0|^2+|\mathcal{B}_0|^2}. \tag{F.6}$$

In order to evaluate the amplitudes, it is convenient to move to the x basis $\{|s\rangle\}$. Since

$$|F_z\rangle = \prod_{i=1}^{N} \left(\frac{|\uparrow\rangle_{x,i} + |\downarrow\rangle_{x,i}}{\sqrt{2}} \right) = \frac{1}{\sqrt{2^N}} \sum_s |s\rangle, \tag{F.7}$$

we arrive at

$$\mathcal{A}_0 = \frac{1}{2^{N_\square} 2^N} \sum_s \langle s| \prod_\Diamond (1 + A_\Diamond) \prod_\square (1 + B_\square) U_{\text{eff}} |s\rangle \tag{F.8}$$

and

$$\mathcal{B}_0 = \frac{1}{2^{N_\square} 2^N} \sum_s \langle s|\bar{X} \prod_\Diamond (1 + A_\Diamond) \prod_\square (1 + B_\square) U_{\text{eff}} |s\rangle, \tag{F.9}$$

where we used that $\frac{1}{2^{N_\Diamond}} \left[\prod_\Diamond (1 + A_\Diamond)\right]^2 = \prod_\Diamond (1 + A_\Diamond)$. Substituting $U_{\text{eff}} = e^{-H_{\text{eff}}}$ and recalling that, for bit-flip errors, H_{eff} is diagonal in the x basis, we can write

$$\mathcal{A}_0 = \frac{1}{2^{N_\square} 2^N} \sum_s e^{-E_s} \langle s| \prod_\Diamond (1 + A_\Diamond) \prod_\square (1 + B_\square) |s\rangle \tag{F.10}$$

and

$$\mathcal{B}_0 = \frac{1}{2^{N_\square} 2^N} \sum_s e^{-E_s} \langle s|\bar{X} \prod_\Diamond (1 + A_\Diamond) \prod_\square (1 + B_\square) |s\rangle, \tag{F.11}$$

where $H_{\text{eff}}|s\rangle = E_s|s\rangle$.

At this point the sums over states s contain all possible x spin configurations of the physical qubits. However, the projectors in Eqs. (F.10) and (F.11) will restrict these configurations. In order to proceed, we can explicitly write that any state s that satisfies the projectors can be written in one of the two forms:

$$|s_1\rangle = \prod_j B_j |F_x\rangle \tag{F.12}$$

$$|s_2\rangle = \bar{Z}_\gamma \prod_j B_j |F_x\rangle, \tag{F.13}$$

where $|F_x\rangle$ is the ferromagnetic state in the x direction, $\bar{Z}_\gamma$ is a logical z following a path γ, and $\prod_j B_j$ is a product over a set of plaquettes. In order for the basis $\{|s_1\rangle, |s_2\rangle\}$ to be complete, all possible products of plaquettes have to be used when generating the states $|s_1\rangle$. Notice that only one path γ should be used for generating the states $|s_2\rangle$; summing over more than one path will render the basis overcomplete. In principle the choice of γ should not be important in the evaluation of the fidelity (choosing γ amounts to choosing a gauge; for each state $|s_1\rangle$ there is a state $|s_2\rangle$ and different γ's just define different correspondences between those states).

Thus, the restricted sums can be explicitly written as

$$\begin{aligned} \mathcal{A}_0 &= \frac{1}{2^N}\left(\sum_{s_1} e^{-E_{s_1}}\langle s_1|s_1\rangle + \sum_{s_2} e^{-E_{s_2}}\langle s_2|s_2\rangle\right) \\ &= \frac{1}{2^N}\left(\sum_{s_1} e^{-E_{s_1}} + \sum_{s_2} e^{-E_{s_2}}\right) \end{aligned} \tag{F.14}$$

and

$$\begin{aligned} \mathcal{B}_0 &= \frac{1}{2^N}\left(\sum_{s_1} e^{-E_{s_1}}\langle s_1|\bar{X}|s_1\rangle + \sum_{s_2} e^{-E_{s_2}}\langle s_2|\bar{X}|s_2\rangle\right) \\ &= \frac{1}{2^N}\left(\sum_{s_1} e^{-E_{s_1}} - \sum_{s_2} e^{-E_{s_2}}\right). \end{aligned} \tag{F.15}$$

Notice that $|\mathcal{A}_0| \geq |\mathcal{B}_0|$ always.

Now consider the infinite-lattice limit. When the spin model of Eq. (6.22) has a well-defined phase transition at a finite temperature, in the "high-temperature" (disordered) phase, which here corresponds to small coupling constant values, states of type $|s_1\rangle$ and $|s_2\rangle$ have the same "partition function", namely, $\sum_{s_1} e^{-E_{s_1}} = \sum_{s_2} e^{-E_{s_2}}$. As a result, $\mathcal{B}_0 = 0$ and $\mathcal{F}_0 = 1$ for coupling constant values below the critical point. In the "low-temperature" (ordered) phase, states $|s_2\rangle$ are energetically more costly than states $|s_1\rangle$ [66], resulting in $\left(\sum_{s_1} e^{-E_{s_2}}\right) / \left(\sum_{s_2} e^{-E_{s_1}}\right) \to 0$ in the

thermodynamic limit. Therefore, for coupling constant values above the critical point, $\mathcal{B}_0 = \mathcal{A}_0$ and $\mathcal{F}_0 = 1/2$.

LIST OF REFERENCES

[1] I. Bengtsson and K. Zyczkowski, *Geometry of Quantum States: An Introduction to Quantum Entanglement* (Cambridge University Press, 1st edition, 2008)

[2] V. Pless, *Introduction to the Theory of Error-Correcting Codes* (Wiley-Interscience, 3rd edition, 1998)

[3] J. Preskill, "Lecture notes on quantum computation", online http://www.theory.caltech.edu/people/preskill/ph229/

[4] A. Altland and B. Simons, *Condensed matter field theory* (Cambridge University Press, 1st edition, 2006).

[5] M. Nakahara, *Geometry, Topology and Physics* (Taylor and Francis Group, 2nd edition, 2003)

[6] J. B. Kogut, Rev. Mod. Phys. **51**, 659 (1979).

[7] X.-G. Wen, *Topological orders and edge excitations in fractional quantum Hall states*. Advances in Physics, Vol. 44, Iss. 5, (1995).

[8] R. B. Laughlin, Phys. Rev. Lett. **50**, 1395 (1983).

[9] D. J. Thouless, M. Kohmoto, M. P. Nightingale, and M. den Nijs, Phys. Rev. Lett. **49**, 405 (1982).

[10] M. Z. Hasan and C. L. Kane, Rev. Mod. Phys. **82**, 3045 (2010).

[11] B. I. Halperin, Phys. Rev. B **25**, 2185 (1982).

[12] F. D. M. Haldane, Phys. Rev. Lett. **61**, 2015 (1988).

[13] W. P. Su, J. R. Schrieffer, and A. J. Heeger, Phys. Rev. Lett. **42**, 1698 (1979).

[14] X.-L. Qi and S.-C. Zhang, Rev. Mod. Phys. **83**, 1057 (2011).

[15] A. H. Castro Neto, F. Guinea, N. M. R. Peres, K. S. Novoselov, and A. K. Geim, Rev. Mod. Phys. **81**, 109 (2009).

[16] A. Stern and N. H. Lindner, Science **339**, 1179 (2013).

[17] A. Y. Kitaev, Phys. Usp. **44**, 131 (2001).

[18] A. Kitaev and C. Laumann, arXiv:0904.2771.

[19] P. Bonderson, S. D. Sarma, M. Freedman, and C. Nayak, arXiv:1003.2856 [quant-ph].

[20] J. Alicea, Y. Oreg, G. Refael, F. Oppen, and M. P. A. Fisher, Nat. Phys. **7** , 412417 (2011).

[21] S. D. Sarma, M. Freedman, and C. Nayak, Phys. Today **59**, 32 (2006).

[22] A. Kitaev, Ann. Phys. **321**, 2 (2006).

[23] E. Dennis, A. Kitaev, A. Landahl, and J. Preskill, J. Math. Phys. **43**, 4452 (2002).

[24] S. B. Bravyi and A. Y. Kitaev, arXiv:quant-ph/9811052.

[25] A. Yu. Kitaev, Ann. Phys. **303**, 2 (2003).

[26] C. Nayak, S. H. Simon, A. Stern, M. Freedman, and S. D. Sarma, Rev. Mod. Phys. **80**, 1083 (2008).

[27] J. Alicea, Phys. Rev. B **81**, 125318, (2010).

[28] L. Fu and C. L. Kane, Phys. Rev. Lett. **102**, 216403 (2009).

[29] E. Ginossar and E. Grosfeld, Nat. Comm. **5**, 4772 (2014).

[30] A. Bühler, N. Lang, C. V. Kraus, G. Möller, S. D. Huber and H. P. Büchler, Nat. Comm. **5**, 4504 (2014).

[31] C. V. Kraus *et al.*, New J. Phys. **14** 113036, (2013).

[32] L. S. Levitov, T. P. Orlando, J. B. Majer, and J. E. Mooij, arXiv:cond-mat/0108266.

[33] R. Barends *et al.*, Nature (London) **508**, 500 (2014).

[34] J. M. Chow *et al.* Nat. Comm. **5**, 4015 (2014).

[35] G. Jotzu *et al.*, Nat. **515**, 237-240, (2014).

[36] A. Weisse, G. Wellein, A. Alvermann, and H. Fehske, Rev. Mod. Phys. **78**, 275 (2006).

[37] R. Klesse and S. Frank, Phys. Rev. Lett. **95**, 230503 (2005).

[38] Several authors have shown that the passive two-dimensional toric code is thermally unstable [e.g., C. Castelnovo and C. Chamon, Phys. Rev. B **76**, 184442 (2007)]. The instability is a general feature of two-dimensional topological systems with local interactions (O. Landon-Cardinal and D. Poulin, arXiv:1209.5750). This is because the strings of errors generated thermally can freely diffuse and wind around the torus, causing a logical error. The same problem does not arise in active QEC, which is the main focus of this paper, since it is possible to act on the state of the system and correct it before errors propagate far enough. In addition, we consider only zero temperature.

[39] Notice that the time evolution determined by Eq. (6.15) will always lead to a superposition between logical up and logical down states with nonzero amplitudes $A_{\{p\}}$ and $B_{\{p\}}$, respectively. The syndrome alone cannot distinguish between a logical $\bar{X}$ and the identity. Therefore, both amplitudes are always present, even after the syndrome and recovery. In the worst-case scenario, the bath would cause the magnitudes $|A_{\{p\}}|$ and $|B_{\{p\}}|$ to be equal, in which case the lowest possible fidelity is 1/2, signaling a complete loss of information about the logical state. There is no situation where all amplitudes $A_{\{p\}}$ go to zero, unless the error operators have

identical coupling constants and act uniformly on all qubits of the code simultaneously. But in this case the system is just doing a global logical state precession.

[40] S. Bravyi, M. Suchara, and A. Vargo, arXiv:1405:4883.

[41] A. J. Ferris and D. Poulin, Phys. Rev. Lett. **113**, 030501 (2014).

[42] P. C. E. Stamp and I. S. Tupitsyn, Chem. Phys. **296**, 281 (2004); A. Morello, P. C. E. Stamp, and I. S. Tupitsyn, Phys. Rev. Lett. **97**, 207206 (2006).

[43] B. M. McCoy and T. T. Wu, Phys. Rev. **162**, 436 (1967); D. B. Abraham, Phys. Rev. Lett. **44** 1165 (1980); H. Au-Yang and M. E. Fisher, Phys. Rev. B **21** 3956 (1980); A. Maciolek and J. Stecki, *ibid*. **54** 1128 (1996).

[44] L. Onsager, Phys. Rev. **65**, 117 (1944).

[45] V. Matveev and R. Shrock, J. Phys. A: Math. Gen. **28** 1557 (1995).

[46] J. Cardy and J. L. Jacobsen, Phys. Rev. Lett. **79**, 4063 (1997).

[47] A. Honecker, J. L. Jacobsen, M. Picco, and P. Pujol, in Proceedings of the NATO Advanced Research Workshop on Statistical Field Theories, edited by A. Cappelli and G. Mussardo (Kluwer Academic, Dordrecht, 2002); arXiv/cond-mat/0112069.

[48] W. L. McMillan, Phys. Rev. B **29**, 4026 (1984).

[49] P. Jouzdani and E. R. Mucciolo, Phys. Rev. A **90**, 012315 (2014).

[50] M. Nielsen and I. L. Chuang, *Quantum computation and quantum information* (Cambridge University Press, 1st ed., 2010).

[51] M. H. Freedman and D. A. Meyer, Found. Comput. Math. **1**, 325 (2001).

[52] D. S. Wang, A. G. Fowler, and L. C. L. Hollenberg, Phys. Rev. A **83**, 020302(R) (2011).

[53] R. Raussendorf and J. Harrington Phys. Rev. Lett. **98**, 190504 (2007).

[54] A. G. Fowler, M. Mariantoni, J. M. Martinis, and A. N. Cleland, Phys. Rev. A **86**, 032324 (2012).

[55] I. Bloch, J. Dalibard, and S. Nascimbene, Nature Phys. **8**, 267 (2012).

[56] R. Blatt and D. Wineland, Nature (London) **453**, 1008 (2008).

[57] M. Saffman, T. G. Walker, and K. Mølmer, Rev. Mod. Phys. **82**, 2313 (2010).

[58] M. A. Eriksson *et al.*, Quant. Info. Proc. **3**, 133 (2004); H. Bluhm *et al.*, Nature Phys. **7**, 109 (2011)

[59] J. Clarke and F. K. Wilhelm, Nature (Londo) **453**, 1031 (2008); D. P. DiVincenzo, Phys. Scr. T **137**, 014020 (2009).

[60] E. Novais, E. R. Mucciolo, and H. U. Baranger, Phys. Rev. Lett. **98**, 040501 (2007).

[61] E. Novais, E. R. Mucciolo, and H. U. Baranger, Phys. Rev. A **78**, 012314 (2008).

[62] E. Novais, E. R. Mucciolo, and H. U. Baranger, Phys. Rev. A **82**, 020303(R) (2010).

[63] D. Aharonov, A. Kitaev, and J. Preskill, Phys. Rev. Lett **96**, 050504 (2006).

[64] H. K. Ng, and J. Preskill, Phys. Rev. A **79**, 032318 (2009).

[65] J. Preskill, Quant. Inf. Comput. **13**, 181 (2013).

[66] E. Novais and E. R. Mucciolo, Phys. Rev. Lett. **110**, 010502 (2013).

[67] D. Aharonov, Phys. Rev. A **62**, 062311 (2000).

[68] U. Weiss, *Quantum Dissipative Systems* (World Scientific, Singapore, 2001).

[69] Notice that Eq. (5) in Ref. [66] has a typo.

[70] G. Duclos-Cianci and D. Poulin, Phys. Rev. Lett. **104**, 050504 (2010).

[71] A. G. Fowler, A. C. Whiteside, and L. C. L. Hollenberg, Phys. Rev. Lett. **108**, 180501 (2012).

[72] When the syndromes point to an error, one can try to recover the state by flipping back qubits. However, there is no guarantee that the appropriate string of qubits is being flipped. As a result, the recovery operation may induce a logical error.

[73] N. Madras and G. Slade, *The Self-Avoiding Walk* (Birkhäuser Boston, 1996).

[74] M. Suzuki and M. Katori, J. Phys. Soc. Jpn. **55**, 1 (1986).

[75] M. Suzuki, M. Katori, and X. Hu, J. Phys. Soc. Jpn. **56**, 2092 (1987).

[76] This expression is obtained using integration by parts and Eqs. 6.56.1.14, 6.693.2, and 6.693.1 from Ref. [77].

[77] I. S. Gradshteyn and I. M. Ryzhik, *Table of Integrals, Series, and Products* (Academic Press, San Diego, 1980), Eq. 6.696.

[78] Ref. [77], Eqs. 6.511.5 and 6.671.8.

[79] Ref. [77], Eq. 6.761.7.

[80] Ref. [77], Eq. 6.693.7.

[81] M. H. Freedman, A. Kitaev, M. J. Larsen, and Z. Wang, Am. Math. Soc. **40**, 31 (2003).

[82] J. Clarke and F. K. Wilhelm, Nature (London) **453**,15 1031 (2008); D. P. DiVincenzo, Phys. Scr. **T137**, 014020 (2009).

[83] B. M. Terhal, F. Hassler, and D. P. DiVincenzo, Phys. Rev. Lett. **108**, 260504 (2012).

[84] H. Paik *et al.*, Phys. Rev. Lett. **107**, 240501 (2011).

[85] J. M. Martinis, K.B. Cooper, R. McDermott, M. Steffen, M. Ansmann, K. D. Osborn, K. Cicak, S. Oh, D. P. Pappas, R. W. Simmonds, and C. C. Yu, Phys. Rev. Lett. **95**, 210503 (2005).

[86] R. Barends *et al.*, Nat. **508**, 500-503, (2014).

[87] A. G. Fowler, A. M. Stephens, and P. Groszkowski, Phys. Rev. A **80**, 052312 (2009).

[88] A. Hutter and D. Loss, Phys. Rev. A **89**, 042334 (2014).

[89] J. R. Wootton and D. Loss, Phys. Rev. Lett. **109**, 160503 (2012).

[90] B. M. Terhal, arXiv:1302.3428.

[91] H. Bombin, R. S. Andrist, M. Ohzeki, H. G. Katzgraber, and M. A. Martin-Delgado, Phys. Rev. X **2**, 021004 (2012).

[92] J. Preskill, technical report No. CALT 68-2881 (2012); arXiv:1207.6131.

[93] P. Jouzdani, E. Novais, and E. R. Mucciolo, Phys. Rev. A **88**, 012336 (2013).

[94] F. L. Pedrocchi, A. Hutter, J. R. Wootton, and D. Loss, Phys. Rev. A **88**, 062313 (2013).

[95] A. Hamma, C. Castelnovo, and C. Chamon, Phys. Rev. B **79**, 245122 (2009).

[96] M. Kardar, *Statistical Physics of Fields* (Cambridge University Press, 2007).

[97] F. F. Assaad and H. G. Evertz, Heraeus Summer School, Greifswald 18-29 Sept. 2006. Lecture Notes.

[98] P. Jouzdani, E. Novais, I. S. Tupitsyn, and E. R. Mucciolo, Phys. Rev. A **90**, 042315 (2014) .

[99] C. Castelnovo and C. Chamon, Phys. Rev. B **78**, 155120 (2008); S. Bravyi and B. Terhal, New J. Phys. **11**, 043029 (2009).

[100] P. W. Shor, Phys. Rev. A **52**, R2493 (1995).

[101] D. Gottesman, Ph.D. thesis, Caltech, 1997.

[102] R. Raussendorf, J. Harrington, and K. Goyal, Ann. Phys. **321**, 2242 (2006); New J. Phys. **9**, 199 (2007);

[103] J. Ghosh, A. G. Fowler, and M. R. Geller, Phys. Rev. A **86**, 062318 (2012).

[104] A. G. Fowler, Phys. Rev. Lett. **109**, 180502 (2012); A. G. Fowler, arXiv:1310.0863; A. G. Fowler and J. M. Martinis, Phys. Rev. A **89**, 032316 (2014).

[105] A. M. Stephens, Phys. Rev. A **89**, 022321 (2014).

[106] J. Preskill, Quant. Inf. Comput. **13**, 181 (2013); H. K. Ng and J. Preskill, Phys. Rev. A **79**, 032318 (2009).

[107] S. Trebst, P. Werner, M. Troyer, K. Shtengel, and C. Nayak, Phys. Rev. Lett. **98**, 070602 (2007).

[108] I. S. Tupitsyn, A. Kitaev, N. V. Prokof'ev, and P. C. E. Stamp, Phys. Rev. B **82**, 085114 (2010).

[109] A. M. Polyakov, *Gauge Fields and Strings* (Hardwood Academic, London, 1987).

[110] J. L. Jacobsen and J. Cardy, Nucl. Phys. **B515**, 701 (1998).

[111] I. Bloch, J. Dalibard, and W. Zwerger, Rev. Mod. Phys. **80**, 885 (2008).

[112] D. Nigg *et al.*, Science **345**, 302 (2014).

[113] M. A. Eriksson *et al*., Quantum Inf. Proc. **3**, 133 (2004); H. Bluhm *et al*., Nat. Phys. **7**, 109 (2011).

[114] The allowed Γ_Z paths can be obtained from that shown in Fig. 6.1 by pulling it up or down at the sites on horizontal edges. Similarly, allowed Γ_X paths are generated from that shown in Fig. 6.1 by pulling it to left or to the right at the sites on horizontal edges.